UNIVERSITY OF SOUTHAMPTON

FACULTY OF NATURAL AND ENVIRONMENTAL SCIENCES

School of Chemistry

New methods for Nitrogen-14 solid state NMR

by

Ibraheem Mohammed Haies

Thesis for the degree of Doctor of Philosophy

July 2015

UNIVERSITY OF SOUTHAMPTON

ABSTRACT

FACULTY OF NATURAL AND ENVIRONMENTAL SCIENCES

School of Chemistry

Thesis for the degree of Doctor of Philosophy

NEW METHODS FOR NITROGEN-14 SOLID STATE NMR

Ibraheem Mohammed Haies

Nitrogen is one of the most abundant elements. It plays a significant role in different scientific disciplines, like materials science, chemistry, biochemistry and pharmaceutical chemistry. Most NMR studies of nitrogen have been performed on samples enriched with ^{15}N. To avoid enrichment and overcome the problem of using NMR where isotopic enrichment is not feasible, NMR of ^{14}N that has 99.6% natural abundance is a viable alternative. However, the ^{14}N spin quantum number 1 and high quadrupolar interactions lead to a few challenges for NMR investigation. Recently, two approaches appeared which overcome the complications associated to the first order quadrupolar line broadening, namely indirect detection using vicinal nuclei and overtone transition. Paper 1 describes a novel version of HMQC experiments, which requires the application of a moderate RF field to the ^{14}N nucleus to correlate the ^{14}N with a ^{13}C ‘spy’ nucleus, which provides good sensitivity on natural abundance and labelled materials. In addition, overtone ^{14}N NMR spectroscopy is a promising route for the direct detection of ^{14}N signals with good spectral resolution. Overtone NMR is the main topic of my research. To overcome the poor efficiency of the overtone transition, polarization transfer techniques have been implemented. Papers 2 and 4 present respectively polarization transfer methods from ^{1}H to the ^{14}N overtone using symmetry-based R-sequences and cross polarization methods. Signal enhancements of 6.7 and 2 have been obtained when cross polarization methods and symmetry-based R-sequences are used respectively. Paper 3 shows results obtained with the DOR (double rotation) technique to reduce ^{14}N overtone linewidth, with ^{14}N overtone spectra with linewidth reduced by nearly one order of magnitude. Analysis of the results has been facilitated through the use of a new simulation strategy for ^{14}N overtone NMR spectroscopy of spinning samples, using *Spinach* library.

Table of Contents

List of Tables

List of Figures

DECLARATION OF AUTHORSHIP

I, Mr. Ibraheem M. Haies

declare that this thesis and the work presented in it are my own and has been generated by me as the result of my own original research.

New methods for Nitrogen-14 solid state NMR

I confirm that:

1. This work was done wholly or mainly while in candidature for a research degree at this University;
2. Where any part of this thesis has previously been submitted for a degree or any other qualification at this University or any other institution, this has been clearly stated;
3. Where I have consulted the published work of others, this is always clearly attributed;
4. Where I have quoted from the work of others, the source is always given. With the exception of such quotations, this thesis is entirely my own work;
5. I have acknowledged all main sources of help;
6. Where the thesis is based on work done by myself jointly with others, I have made clear exactly what was done by others and what I have contributed myself;
7. Parts of this work have been published in the next page, with the List of papers:

Signed: ....

Date: ....

List of Papers

I. An efficient NMR method for the characterisation of ^{14}N sites through indirect ^{13}C detection.

Jarvis, J. A.; **Haies, I. M.**; Williamson, P. T. F.; Carravetta, M.

Phys. Chem. Chem. Phys. 2013, 15, 7613.

II. ^{14}N Overtone NMR under MAS: signal enhancement using symmetry-based sequences and novel simulation strategies.

Haies, I. M.; Jarvis, J. A.; Bentley, H.; Heinmaa, I.; Kuprov, I.; Williamson, P.; Carravetta, M.

Phys. Chem. Chem. Phys. 2015, 17, 6577.

III. ^{14}N overtone transition in double rotation solid-state NMR.

Haies, I. M.; Jarvis, J. A.; Brown, L. J.; Kuprov, I.; Williamson, P.; Carravetta, M.

Accepted in *Phys. Chem. Chem. Phys.* 2015.

IV. ^{14}N overtone NMR under MAS: signal enhancement using cross polarization methods,

Haies, I. M.; Jarvis, J. A.; Kuprov, I.; Williamson, P.; Carravetta, M.

Will be submitted soon in *J. Magn. Reson.* 2015.

Acknowledgements

First, I would like to present my graduate to my family who, even though they were far away from me during my PhD studies, they were in my heart and my mind all the time and this was supporting me, in addition to their support. I really would like to thank them for everything they have done for me. Thanks all.

I wish to express my deep gratitude to my supervisor Marina Carravetta for every way she supported me. She really was an amazing supervisor, not just scientifically. I am very grateful that she was my supervisor during my PhD study. This was the best thing ever in my PhD study. Many thanks Marina for your patience, scientific advices and everything you helped me with.

Acknowledgment to The Higher Committee for Education Development in Iraq for financial support to complete my PhD studies. I would also like to present my thankfulness for all teachers who have taught me over my studies in Iraq and in the UK. Many thanks for all knowledge, behaviours, and advices I have obtained from you.

I am indebted to Phil Williamson for his ideas, patience to advice and guide me over my study. It was really helpful and fruitful collaborating with you. Thanks Phil. Here also I would like to thanks all my colleagues, friends and people know me for their friendship and support, Richard Bounds, James Jarvis and Stuart Findlow for always helping out when they were needed, Ole Johannessen for sharing his technical knowledge and helping in machines' technical issues, Ilya Kuprov for development of Spinach and experienced support and all the magres section members for their help.

The UK 850 MHz solid-state NMR Facility instruments used in this research were funded by EPSRC and BBSRC, as well as the University of Warwick, including via part funding through Birmingham Science City Advanced Materials Projects 1 and 2 supported by Advantage West Midlands (AWM) and the European Regional Development Fund (ERDF). Acknowledgment to all members there, especially Dinu Iuga who was very helpful in the instrument set-up and sharing his knowledge.

Thanks to Ivo Heinmaa and Raivo Stern in the National Institute of Chemical Physics and Biophysics in Tallinn, Estonia for helping to do some experiments in their lab.

بِسْمِ اللَّهِ الرَّحْمَنِ الرَّحِيمِ

فَأَمَّا الزَّبَدُ فَيَذْهَبُ جُفَاءً

وَأَمَّا مَا يَنفَعُ النَّاسَ فَيَمْكُثُ فِي الأَرْضِ

كَذَلِكَ يَضْرِبُ اللَّهُ الأَمْثَالَ

صدق اللَّهُ العظيم

In the name of Allah, the Gracious, the Merciful

As for the foam, it vanishes, [being] cast off; but as for that which benefits the people, it remains on the earth Thus does Allah present examples.

Truth of the great God

Chapter 1: Basics and Principles of Magnetic Resonance

1.1 Introduction

In 1945, the birth of NMR technology stemmed from two notable experiments: first, a weak radio-frequency signal from proton in a solid material (paraffin) was detected by Purcell, Torrey and Pound[1]. Bloch, Hansen and Packard did the second experiment. They detected a proton signal in liquid paraffin[2]. These works were independent of each other and both Purcell and Bloch received the Nobel Prize in Physics in 1952.

NMR was discovered and developed by physicists, but it is used in other fields like chemistry and medicine. NMR techniques are used to investigate molecular structure and dynamics in chemistry. For instance, the chemical shift reflects the local nuclear environment, so it plays a significant role in determining the molecular structure[3].

As new pulse programs are developed, more detailed information can be resolved from the studies. For example, the discovery of two dimensional experiment to get heteronuclear correlation was a major breakthrough in ^{13}C NMR in the 1980s and for ^{1}H in 1990s. In 1991 Ernst received the Nobel Prize for his work in multidimensional spectroscopy[4].

1.2 Basics of Magnetic Resonance

1.2.1 Nuclear Spin

Atoms have four main physical features: mass, electric charge, magnetism and spin. For NMR spectroscopy the major properties are spin and magnetism. Spin is a form of angular momentum, but it is an intrinsic property of the particle and, unlike orbital angular momentum, it does not originate from the rotation of the particle in space. Since the proton and neutron are both comprised of three particles (quarks) and each of these particles has spin ½, proton and neutron also have spin ½ (except in high energy). Therefore, the nucleus, which consists of protons and neutrons, also has an overall spin, which depends on the numbers of protons and neutrons. For example, ^{1}H has spin ½ because it consists of one proton, while ^{2}H has spin 1 and it consists of one proton and one neutron. Nuclei with the same atomic numbers (number of protons) but different mass numbers (number of protons and neutrons) are called isotopes. The isotopes which have spin quantum number *I* = 0, like ^{12}C and ^{16}O, are NMR silent. Table 1.1 shows some of the most important NMR isotopes and their properties.

Table 1.1 Selection of popular nuclear isotopes and their properties.

Isotope	Ground-state nuclear spin	Natural abundance, %	Gyromagnetic ratio (γ), 10^6 rad s^{-1} T^{-1}	Resonance frequency at 9.4T, MHz
^{1}H	½	~100	267.522	-400.000
^{2}H	1	0.015	41.066	-61.43
^{13}C	½	1.1	67.283	-100.659
^{14}N	1	99.6	19.338	-28.9
^{15}N	½	0.37	-27.126	40.58
^{17}O	5/2	0.04	-36.281	54.27
^{12}C	0	98.9		
^{16}O	0	~100		

When a nucleus with spin *I* is placed in a magnetic field, it splits in (2*I*+1) sublevels which have different energy and the splitting between these levels is called the nuclear Zeeman splitting. In absence of the field these levels are degenerate (Fig. 1.1).

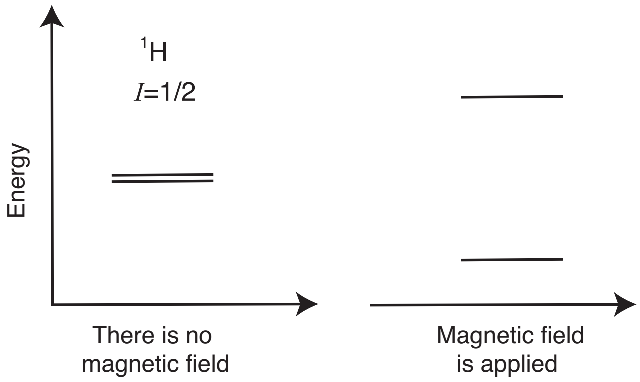

Fig. 1.1 Nuclear ground state of the proton with and without static magnetic field.

A material, which is placed in a magnetic field, will interact with this field and the spin Hamiltonian can be expressed as:

$$H = H_{ele} + H_{mag} \tag{1.1}$$

where H_{ele} describes the effect of the electric field (which is 0 for spin *I* =1/2 nuclei), and H_{mag} describes the effect of the magnetic field, which can be expressed as:

$$H_{mag} = -u.B \quad (1.2)$$

where u is the magnetic moment operator, and B is the static magnetic field.

The magnetic interaction comes from: magnetic moments of electron and nuclei, and electric current. The concept of the magnetism, which comes from electron and nuclei, is difficult to understand.

There is a relationship between magnetic moment and spin angular momentum, which is:

$$u = \gamma \mathbf{I} \quad (1.3)$$

where γ is the gyromagnetic ratio and it is specific for the each nuclear species. The gyromagnetic ratio may have either sign. The lowest energy configuration for the spin angular momentum is parallel to the magnetic moment for nuclei with a positive γ, and opposite to the magnetic moment for nuclei with a negative γ.

Classically, the magnetic moment of the nuclear spin placed in a magnetic field will turn around the static magnetic field and the angle between the field and the nuclear spin will be kept unchanged. This movement around the static magnetic field is called precession. The frequency of the nuclear spin precession is the so-called Larmor frequency, which can be expressed as:

$$\omega_0 = -\gamma B_0 \quad (1.4)$$

where γ is the gyromagnetic ratio and it is specific for the each nuclear species[3].

1.2.2 Effect of a Pulse

The net magnetization of nuclei in a static magnetic field is along the field, it is static and it is almost undetectable. On the other hand, NMR detects the magnetization in the *xy*-plane because it generates a time modulated signal, which is easy to detect, as discussed in the next section. Therefore an electromagnetic wave is applied to transfer the magnetization to the *xy*-plane. A much weaker, time dependent radio frequency (RF) field is used for this purpose, but the RF field has to be on resonance to do that. The interaction of the spin with the RF pulse can be expressed as:

$$H_{RF} = \omega_1[\cos\left(\omega_{RF}\mathrm{t} + \phi(\mathrm{t})\right) I_{\mathrm{x}} + \sin\ (\omega_{RF}\mathrm{t} + \phi(\mathrm{t}))I_{\mathrm{y}}] \quad (1.5)$$

where $\omega_1 = -\gamma B_1$, B_1 is the magnetic field associated with the pulse applied and ϕ is the phase.

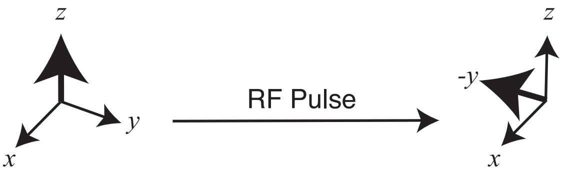

Fig. 1.2 Transfer the magnetization from *z*-axis plane by applying a π/2 pulse along *–y*.

The direction of the overall magnetization after the applied pulse is dependent on the duration and the amplitude of the pulse. Fig. 1.2 shows the effect of a $(\pi/2)_x$ pulse to transfer the magnetization from the *z*-axis onto the *xy*-plane.

1.2.3 NMR Signal

After an RF pulse, the magnetization will precess at the Larmor frequency ω_0 around the magnetic field and it can be expressed in the *xy*-plane at any time as:

$$M_y = -M_{eq}\cos(\omega_0\, t)\exp\{-\frac{t}{T_2}\} \tag{1.6}$$

$$M_x = M_{eq}\sin(\omega_0\, t)\exp\{-\frac{t}{T_2}\} \tag{1.7}$$

In NMR spectroscopy what is actually detected is the precession of the magnetization vector in the *xy*-plane. This magnetization induces an oscillating current in the coil around the sample, and the current decays as the magnetization decays. This decay will lead to the Free Induction Decay (FID), which is detected in the NMR spectrometer, and this is the NMR signal in the time domain.

1.2.4 Fourier Transformation

In modern NMR spectroscopy what is actually detected is the FID. The visual interpretation of the signal components contained in the FID is not straightforward in general. Hence, the usual approach is to convert the signal from the time domain to frequency domain, which is often of easier interpretation. This is achieved with a mathematical technique called Fourier transform (FT). The Fourier transform can be written as:

$$S(f) = \int_0^{+\infty} S_{FID}(t)\cos(2\pi f t)\,dt \tag{1.8}$$

where $S(f)$ is the intensity of the signal at frequency f, $S_{FID}(t)$ is the amplitude of the FID at time t, and $\cos(2\pi f t)$ is the trial cosine function[6]. Fig. 1.3 illustrates the FT method.

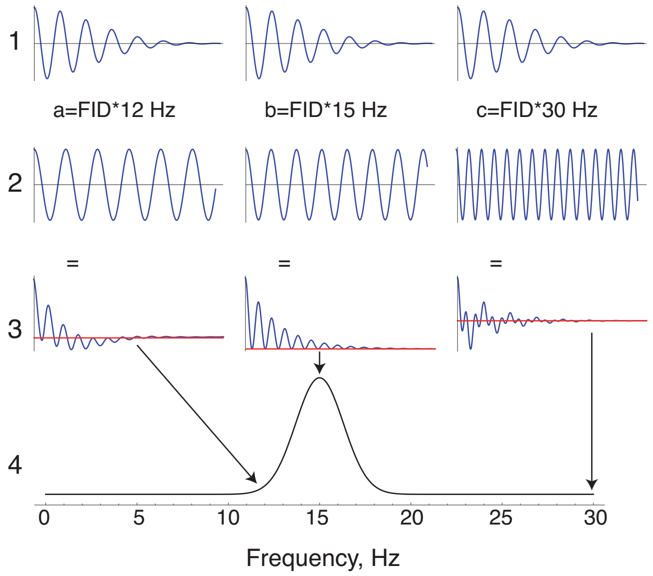

Fig. 1.3 Visual description of how the FT works. The FIDs shown in row 1 are multiplied by trial cosine functions of known frequency, with some of them shown in row 2 (12 Hz in a, 15 Hz in b and 30 Hz in c). Row 3 shows the product functions, from the multiplication of row 1 by row 2. The area under the product functions is illustrated in row 4 and is the spectrum.

1.3 Nuclear Spin Interactions

The nuclear spin interacts with external magnetic fields. These fields include: the static magnetic field, the RF field and the gradient field. In addition to the external interactions there are internal nuclear spin interactions.

The full Hamiltonian describing a homonuclear spin system can be expressed as:

$$H = H_Z^I + H_{RF} + H_Q^I + H_{CS}^I + H_D^{II} + H_J^{II} \tag{1.9}$$

where H_Z is the Zeeman Hamiltonian and it can be given as:

$$H_Z = -\gamma \mathbf{I} \cdot B_0 \tag{1.10}$$

$\hat{H}_{Q}^{I}$ is the Hamiltonian for the quadrupolar interaction, $\hat{H}_{D}^{II}$ is the Hamiltonian for the dipole-dipole interaction, H_{CS}^{I} is the Hamiltonian for the chemical shift interaction[8] and H_{J}^{II} is the Hamiltonian for the indirect dipolar coupling interaction.

The Hamiltonian for an arbitrary nuclear spin interaction can be expressed in general as:

$$H = -\gamma \mathbf{I} \cdot B_{loc} = -\gamma \mathbf{I} \cdot A_{loc} \cdot B_{loc}^{sou} \tag{1.11}$$

where A_{loc} is the Cartesian tensor (δ for the chemical shift, V for the quadrupolar interaction and D for the dipole-dipole interaction, J for indirect dipolar coupling) describing the nature of the nuclear spin interaction and its orientation. B_{loc}^{sou} is a vector representing the source of the B_{loc} magnetic field at the nucleus, e.g. B_0 for the chemical shift interactions or another nuclear spin for the dipolar coupling interaction[8]. A_{loc} can be expressed as:

$$A_{loc} = \begin{bmatrix} A_{xx} & A_{xy} & A_{xz} \\ A_{yx} & A_{yy} & A_{yz} \\ A_{zx} & A_{zy} & A_{zz} \end{bmatrix} \tag{1.12}$$

The isotropic part of this interaction is related to the trace of this tensor, expressed as:

$$A_{loc}^{iso} = \frac{1}{3}(A_{xx} + A_{yy} + A_{zz}) \tag{1.13}$$

The nuclear spin interactions can be classified through their ranks (signatures of theses interactions) with respect to; field rank B, space rank *l*, spin rank λ and Table 2.1 summarizes some of the nuclear spin interactions according to these ranks.

Table 1.2 Ranks of some NMR nuclear spin interactions. Antisymmetric interactions are neglected. Only isotropic interactions remain in liquids.

Interactions	Space rank (*l*)	Spin ranks (λ)	Field rank (B)
Zeeman	0	1	1
RF- Field	0	1	1
Isotropic chemical shift	0	1	1
Chemical shift anisotropy	2	1	1
Isotropic *J*-coupling	0	0	0
Dipole-dipole coupling	2	2	0
Electric quadrupolar coupling	2	2	0

1.3.1 Chemical Shift Interaction

The chemical shift is induced by the electrons around the nucleus. The electron clouds in the molecules are affected by the external magnetic field and give rise to a secondary magnetic field, which is called the induced field $B_{induced}^{j}$ and it can be expressed as:

$$B_{induced}^{j} = \delta^{j} \cdot B_0 \tag{1.14}$$

where δ^{j} is the chemical shift tensor. Using the notation introduced in Eq.(1.12), this tensor can be written as:

$$\delta = \begin{bmatrix} \delta_{xx} & \delta_{xy} & \delta_{xz} \\ \delta_{yx} & \delta_{yy} & \delta_{yz} \\ \delta_{zx} & \delta_{zy} & \delta_{zz} \end{bmatrix} \tag{1.15}$$

The overall local field will be the sum of the static magnetic field and the induced field.

$$B_{loc}^{j} = B_0 + B_{induced}^{j} \tag{1.16}$$

Although the induced field is very small compared with the external field, it is enough to change the spin procession frequency of the nuclei in a measurable way. Chemical shift plays a major role for sample characterization via NMR and it provides a tool to relate directly the NMR signal to the local chemical environment. Both the isotropic and the anisotropic chemical shift can provide important information about the nuclear environment.

The chemical shielding Hamiltonian is given by:

$$H_{CS} = \gamma \mathbf{I} \cdot \delta \cdot B_0 \tag{1.17}$$

1.3.2 Quadrupolar Coupling Interactions

About 74% of the NMR active nuclei have spin larger than ½, and are classified as quadrupolar nuclei. Spin ½ nuclei have a spherical charge distribution but quadrupolar nuclei have an electric quadrupole moment, which originates from the fact that the charge distribution is not spherical. The electric quadrupole moment interacts with the electric field gradient, which is produced from the electrons participating in bonds around the nucleus of interest. Table 1.3 shows some important quadrupolar nuclei with some properties. The quadrupolar interaction will be described more in details in chapter three.

Table 1.3 A selection of common quadrupolar nuclei in NMR, and their electric quadrupole moment.

Isotope	Ground-state nuclear spin	Natural abundance, %	Electric quadrupole moment, 10^{-28} m^2
^{2}H	1	0.012	0.2860
^{11}B	3/2	80.1	4.059
^{14}N	1	99.6	2.044
^{17}O	5/2	0.038	-2.558
^{87}Rb	3/2	27.8	0.132
^{79}Br	3/2	50.69	31.3
^{81}Br	3/2	49.31	26.15
^{23}Na	3/2	100	10.4
^{27}Al	5/2	100	14.66

1.3.3 Dipolar Coupling interaction

Typical NMR samples contain several NMR active nuclei, each of these generates a small magnetic moment. The direct interactions between one nuclear spin with other nuclear spins is called through-space dipole-dipole coupling or direct dipole-dipole coupling and is expressed as:

$$H_D = -2\mathbf{I} \cdot D \cdot \mathbf{S} \tag{1.18}$$

where *D* is the dipolar-coupling tensor, which describes the interaction between spin *I* and spin *S*. Since the dipolar-coupling tensor is traceless, it just contains an anisotropic component. The dipolar-coupling tensor depends on the dipolar-coupling constant.

The dipole-dipole spin Hamiltonian can be written in terms of the dipolar-coupling constant as:

$$H_{D_{IS}} = b_{IS}[3(\mathbf{I}_I . e_{IS})(\mathbf{I}_S . e_{IS}) - \mathbf{I}_I . \mathbf{I}_S] \tag{1.19}$$

where e_{IS} is a unit vector parallel to the line between the *I* and *S* spins and b_{IS} is the dipole-dipole coupling constant, given by:

$$b_{IS} = -\hbar \left[\frac{\mu_\circ}{4\pi}\right] \frac{1}{r^3} \gamma_I \gamma_S \tag{1.20}$$

where r is the distance between spin I and spin S and μ_0 is the vacuum permeability. Therefore, the dipolar coupling depends on the distance between the two nuclear spins, as well as on the orientation of the internuclear vector and the static magnetic field.

Dipolar couplings can be classified as follows:

1- Homonuclear dipolar coupling, when *I* and *S* are the same nuclear species.

The dipole-dipole spin Hamiltonian for homonuclear dipolar coupling can be given as:

$$H_{D_{IS}}(\phi_{IS}) = d_{IS}[3I_{Iz}I_{Sz} - \mathbf{I}_I . \mathbf{I}_S] \tag{1.21}$$

where d_{IS} in this case is the secular dipole-dipole coupling, given by:

$$d_{IS} = b_{IS}\frac{1}{2}(3cos^2\phi_{IS} - 1) \tag{1.22}$$

where ϕ_{IS} is the angle between the static magnetic field and e_{IS}.

2- Heteronuclear dipolar coupling, when *I* and *S* are different nuclear species.

The dipole-dipole spin Hamiltonian for heteronuclear dipolar coupling can be given as:

$$H_{D_{IS}}(\phi_{IS}) = d_{IS}2I_{Iz}I_{Sz} \tag{1.23}$$

1.3.4 *J*- coupling

Participation of the electrons to the interactions between spins leads to the indirect spin-spin coupling, or *J*-coupling, or indirect dipole-dipole coupling. Since the electrons participate in the interaction, the *J*-coupling is an important link between NMR and chemistry. The *J*-coupling gives important information about the chemical bonds in a molecule.

The Hamiltonian that describes the *J*-coupling is:

$$H_J = 2\pi\mathbf{I}_I \mathrm{J}\, \mathbf{I}_S \tag{1.24}$$

where J is the *J*-coupling tensor.

For an isotropic liquid, the *J*-coupling has in general a non-zero isotropic component.

The Hamiltonian for the isotropic part of the *J*-coupling can be expressed as:

$$H_{J_{IS}} = 2\pi J_{IS}(I_{Ix}I_{Sx} + I_{Iy}I_{Sy} + I_{Iz}I_{Sz}) \tag{1.25}$$

where J_{IS} is the scalar coupling and can be given as:

$$J_{IS} = \frac{1}{3}(J_{xx}^{IS} + J_{yy}^{IS} + J_{zz}^{IS}) \tag{1.26}$$

The isotropic *J*-coupling is independent on molecular orientation and it is typically small. In solid state NMR usually the peaks are broader than this interaction and the isotropic *J*-coupling is often not directly resolved.

Since the anisotropic *J*-coupling behaves like the dipolar coupling, there is no way to measure it independently, but it can be estimated from first principle calculations. In solid state NMR the *J*-coupling is typically much smaller than other anisotropic interactions, therefore is often ignored. It is nevertheless possible to measure and study the *J*-coupling in solids with suitable methods[9-13].

Chapter 2: Solid State NMR

2.1 Introduction

Solid state NMR has significantly developed over the last decades to become a prominent research technique used in chemistry, biochemistry and materials science. The first NMR spectrum was acquired in 1945 by Purcell *et al.* at Harvard university when they recorded the proton spectrum of paraffin wax in solid state[1]. It is fair to mention that there were two unsuccessful efforts to record NMR spectra of solid materials by Gorter in 1936[14] and Gorter and Broer in 1942[15]. For the first thirty years, most NMR studies were in the liquid state because of the high resolution of liquid state NMR and the lack of resolution and challenging signal to noise of solid state NMR. A step change in the adoption of solid state NMR as a research and analytical tool followed the invention of the magic-angle spinning (MAS), discussed in the next section.

The most important factor affecting the resolution of solid state NMR is the orientation dependence of the NMR interactions. As discussed in Chapter 1, the Hamiltonian for nuclear spin interactions contains both isotropic and anisotropic components (see Table 1.2). The NMR spectrum of a powder material depends on the orientation of the nuclei with respect to the magnetic field in each individual crystallite. This is illustrated in Fig. 2.1.

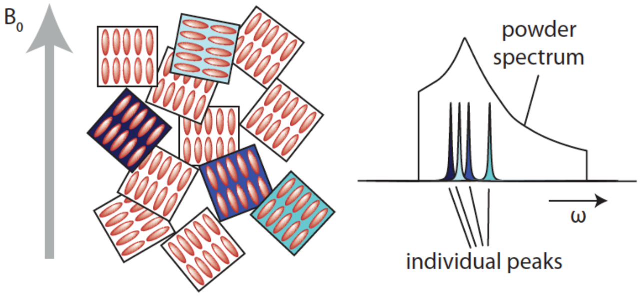

Fig. 2.1 Effect of the molecular orientation on the NMR spectrum of a powder. Each crystallite with a different orientation gives a spectrum, which depends on its orientation with respect to the magnetic field. (Reprinted from Ref[3]).

The high molecular mobility in the liquid state averages out the anisotropic nuclear spin interactions. Solid materials have motional restriction, therefore the anisotropic part of spin interactions strongly depend on the molecular orientation. Thus, the linewidth in solid state NMR is much broader than in liquid state NMR and it consists of the superposition of the spectra arising from all crystallites in the powder. For example, the linewidth of the proton spectrum in solid water is broader by a factor of six orders of magnitude than the linewidth of the proton spectrum in liquid water[16], as shown in Fig. 2.2.

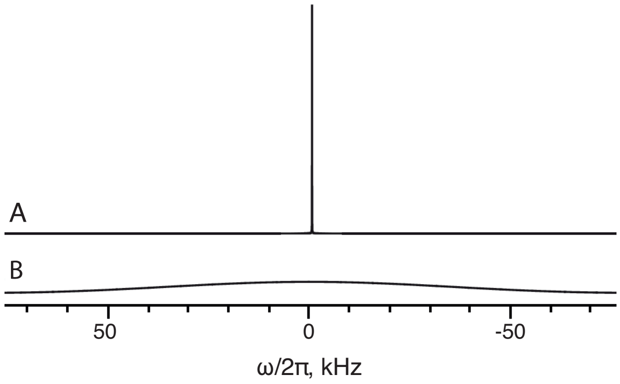

Fig. 2.2 Schematic representations of ^1H NMR spectra for water (A) a liquid sample at room temperature and (B) a solid sample at low temperature.

2.2 High Resolution Solid State NMR

Solid state NMR suffers from a lack of high resolution. Therefore, several techniques have been developed to improve the resolution of solid state NMR.

2.2.1 Magic Angle Spinning (MAS)

One of the most significant issues facing solid state NMR is the line broadening that comes from the orientation dependence. Removing the anisotropic broadening from the spectrum by spinning the solid sample was first noted independently by Andrew[17,18] and by Lowe[19] at the end of the 1950s. Rapidly rotating the sample at a specific angle of $\theta_R = 54.74^o$ (called the magic-angle) between the static magnetic field and the rotation axis averages out the second rank tensor interactions to first order, therefore all sources of the broadening coming from these interactions are removed[20,21]. A schematic view of the MAS set-up is provided in Fig. 2.3. Although MAS was discovered in the early stages of NMR, it was not used commonly at first because it was thought that to remove the anisotropic spin interactions, the spinning frequency had to be larger than the magnitude of the interactions themselves. At the end of the 1970s, it was found that MAS narrows down anisotropic lineshapes and splits them up into narrow ‘spinning sidebands’, which are narrow peaks at integer multiples of the spinning frequency from the isotropic peak position. This occurred even when the spinning frequency was much smaller than the anisotropic interaction (as for the case of the Chemical Shift Anisotropy, CSA in the first reports of this behaviour)[22,23].

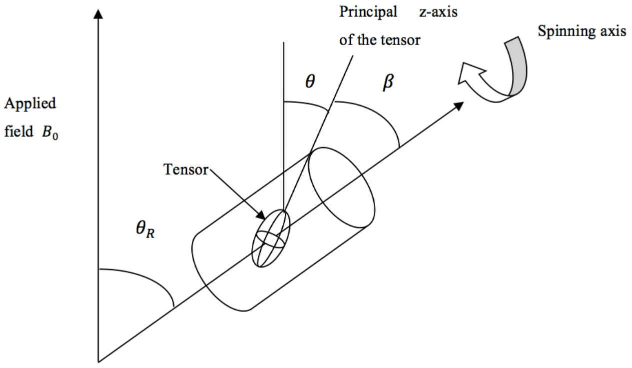

Fig. 2.3 The magic-angle spinning scheme: the sample is rotated about an axis at an angle θ_R equal to 54.74^o with respect to the static magnetic field. θ is the angle between the *z*-axis of the Principal Axis Frame (PAF) tensor of an interaction and the static magnetic field and β is the angle between the *z*-axis of the PAF tensor and the rotation axis.

MAS now is used routinely for many applications. Anisotropic interactions with rank 2 are averaged out to good extent using MAS without affecting the isotropic chemical shift and *J*-coupling interactions. The orientation dependence term $3cos^2\theta - 1$ can be expressed under spinning of the sample at the θ_R as:

$$\langle 3cos^2\theta - 1\rangle_{\tau_r} = \frac{1}{2}(3cos^2\theta_R - 1)(3cos^2\beta - 1) \tag{2.1}$$

where θ is the angle between the static magnetic field and the *z*-axis of the Principal Axis Frame (PAF) of the tensor for one of the internal spin interactions. β is the angle between the *z*-axis of the PAF of an interaction tensor and the rotating axis. The term $3cos^2\theta - 1$ vanishes when θ_R is equal to 54.74^o (MAS).

The MAS technique enhances significantly the sensitivity of solid state NMR. Fig. 2.4 below shows the improvement in sensitivity with MAS for the ^{1}H spectra of a powder of adamantane. At low spinning frequency, a large number of spinning sidebands appear in the spectrum. The spinning sidebands start to disappear with an increase in the spinning frequency. The spinning rate has to be fast enough to remove the spinning sidebands completely, typically around a factor of 3 or 4 larger than the size of the anisotropic interaction. In addition to fast spin rates, there are other two ways to remove the spinning sidebands. First, record the FID synchronously with the rotor period[24]. Second, use the Total Suppression of Spinning sidebands pulse sequence[25].

The peak linewidth at moderate spinning frequency is broader than the linewidth at high spinning frequency (Fig. 2.4). This is because the Hamiltonian of the homonuclear dipolar coupling does not commute with each other. Therefore, overage out all the anisotropic interactions of the homonuclear dipolar coupling is no longer possible at moderate spinning frequency and to achieve satisfactory line narrowing, the spinning frequency must be larger than the dipolar coupling strength.

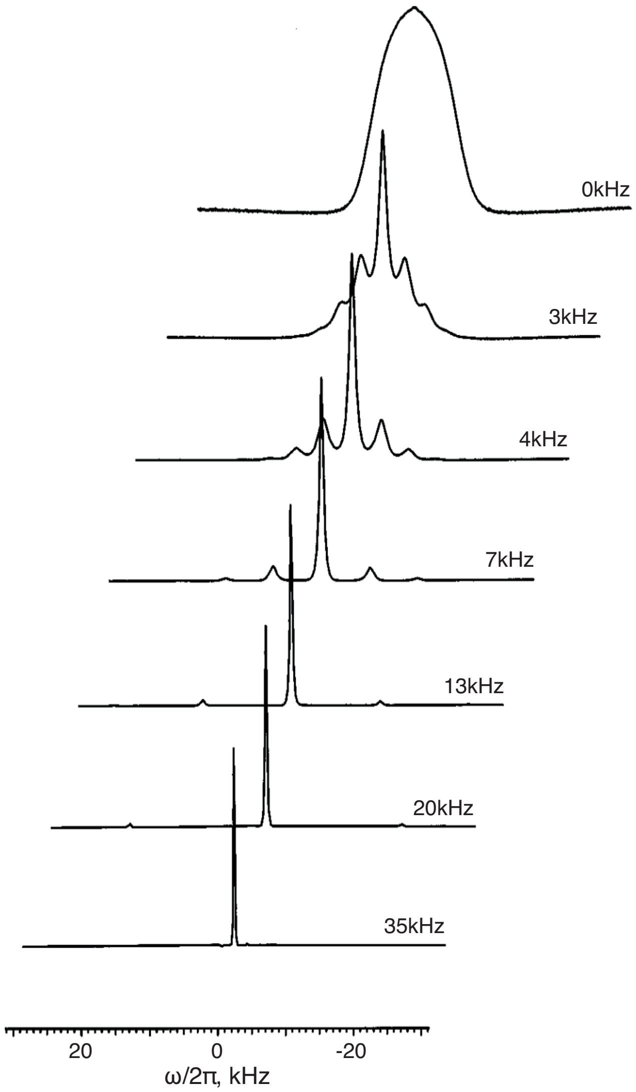

Fig. 2.4 ^{1}H NMR spectra of adamantane acquired under static conditions and at different spinning frequencies in the range from 0 to 35 kHz. This serves as an example for a sample with homogenous line broadening. (Reprinted from Ref[26]).

2.2.2 Decoupling

Although MAS makes a significant improvement to solid state NMR resolution by partly removing the line broadening coming from anisotropic interactions (Fig. 2.5C static and B under MAS), the lines are still broad, which complicate the investigation of materials. This is because MAS, even with the highest spinning frequencies available now, cannot fully average out all the anisotropic interactions, in particular ^{1}H-^{1}H dipolar interactions. Therefore, the use of decoupling techniques is often necessary to improve resolution.

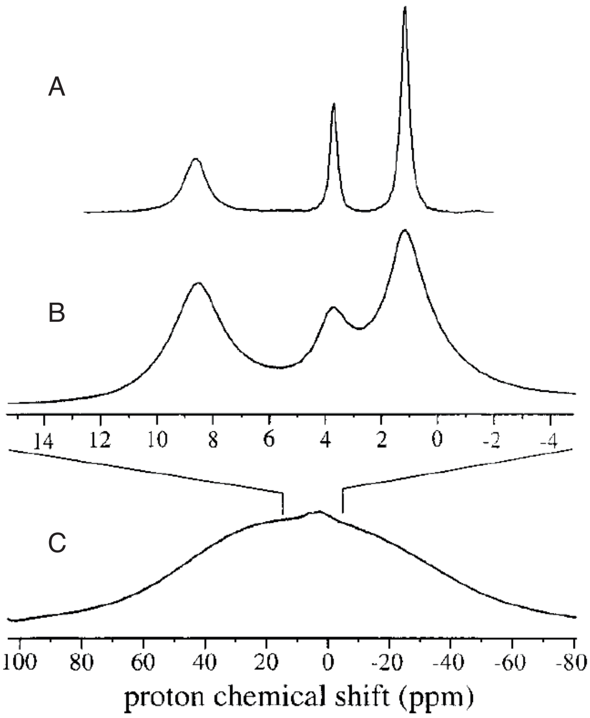

Fig. 2.5 ^{1}H NMR spectra of powdered L-alanine acquired with (A) Combined Rotation and Multiple Pulse Sequence under 12.5 kHz spinning frequency using FSLG decoupling, (B) one pulse at 30 kHz spinning frequency, and (C) one pulse under static conditions. (Reprinted from Ref[27])

2.2.2.1 Heteronuclear Decoupling

The simplest technique to achieve heteronuclear decoupling is high-power decoupling without any modulation of the RF field. This is called continuous wave decoupling (CW), and is achieved by applying a high-power pulse on the nuclear spin to decouple. The nutation frequency of the pulse should ideally be at least three times larger than the magnitude of the dipolar coupling between nuclei[8]. For example the dipole-dipole coupling between proton-nitrogen pair is about 20 kHz, therefore more than 60 kHz RF nutation frequency should lead to good heteronuclear decoupling. In addition to the high-power decoupling there are other methods which can achieve the decoupling, like Two Pulse Phase Modulation (TPPM)[28], composite-pulse decoupling and SPINAL-64[29].

2.2.2.2 Homonuclear Decoupling

There are many pulse sequences, which can be used to achieve homonuclear decoupling. The first one is the Lee-Goldburg homonuclear dipolar decoupling (LG), which can be achieved by making the effective magnetic field at magic angle with respect to the static magnetic field. This can be done by adjusting the resonance offset of the RF field to be off resonance according to the equation $\Delta\omega = \pm\sqrt{1/2}\,\omega_1$. Under these circumstances the homonuclear dipolar interactions are averaged out and the heteronuclear dipolar interactions and the chemical shift of the decoupled nuclei are scaled by factor $1/\sqrt{3}$ because the Hamiltonian for the homonuclear dipolar coupling is scaled by $(3cos^2\,\theta - 1)$ and for heteronuclear dipolar coupling the scaling factor is $cos\theta$[30]. The WAHUHA pulse sequence[31], which is one of the simplest pulse sequences in this family can also be used to achieve homonuclear decoupling.

The Frequency-Switched Lee-Goldburg (FSLG)[32], and Phase-Modulated Lee-Goldburg (PMLG)[33] can also be used. The FSLG decoupling is implemented by dividing the decoupling duration into periods of duration $\tau = 2\pi\sqrt{2/3}\,/\omega_1$, and the RF offset alternates between plus and minus the Lee-Goldburg frequency in these intervals, while the phase of the RF also changes by π every time. Some rotor synchronised sequences can also be used to remove the homonuclear coupling[34]. In addition, high resolution solid state NMR of ^1H, for a sample containing a network of strongly interacting protons, can be achieved by combining MAS with homonuclear decupling technique. This method is called Combined Rotation and Multiple Pulse Sequences (CRAMPS)[27,35-38]. Fig. 2.5A illustrates a ^1H spectrum using the CRAMPS method.

2.3 Sensitivity Enhancement Techniques

2.3.1 Cross Polarization (CP)

Solid state NMR studies of nuclei with low gyromagnetic (γ), like ^{13}C were not common even with MAS till 1973 when Pines *et al.* did the first experiment to enhance the signal for such nuclei[39]. This method is now widely used in solid state NMR and is called Cross Polarization (CP) which is a technique used to increase the NMR sensitivity of the low gyromagnetic ratio nuclei by transfer magnetization from high gyromagnetic ratio such as ^1H to low gyromagnetic ratio nuclei such as ^{13}C. In addition to the enhancement of the low gyromagnetic ratio nuclei by the different populations between spin up and spin down state, the pulse recycle delay depends on the relaxation time of the higher gyromagnetic ratio which is usually ^{1}H and it is usually lower than the relaxation time of the low gyromagnetic ratio nucleus that leads to a decreases in time between successive FID's, thus high resolution spectra can be obtained in less time[40].

The CP pulse sequence is shown in Fig. 2.6 below. First, a 90° pulse on the *I*-spin is applied to transfer the magnetization to $-y$. Then a so-called contact pulse is applied to both nuclei (*I*-spin and *S*-spin), which achieves a spin-lock. To transfer the magnetization from I to S the RF pulse on the two nuclear species must match the Hartmann-Hahn's condition[41] which is:

$$\gamma_I B_1(I) = \gamma_S B_1(S) \tag{2.2}$$

Under MAS, this condition is modulated by the spinning frequency[23]:

$$\gamma_I B_1(I) = \gamma_S B_1(S) \pm n\,\omega_r \tag{2.3}$$

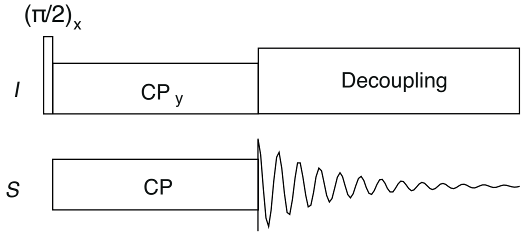

Fig. 2.6 Cross polarization pulse sequence. 90° pulse applied on *I*, which has high gyromagnetic ratio, moves the magnetization along *–y*. The contact pulses are applied simultaneously on both nuclei to transfer the magnetization to the *S*-nucleus.

Different kinds of cross polarization methods have been applied to enhance the signal of the low-γ nuclei. For example, conventional CP with constant amplitudes has been used. Better signal enhancement is achieved by changing the proton amplitude linearly during the contact pulse[42]. In addition, cross polarization efficiency can be increased also by applying an adiabatic pulse on one of the nuclei[43,44].

2.3.2 Heteronuclear Polarization Transfer by Symmetry-Based Recoupling Sequences

Rotating the sample at the magic angle averages out most of the heteronuclear dipole–dipole interactions. Therefore, recoupling methods are required to achieve heteronuclear polarization transfer, by re-introducing the heteronuclear dipole–dipole interactions. These sequences were first used at end of the 1980s when it was found that the heteronuclear dipolar interaction under MAS may be brought back by applying a continuous RF field to one spin species[45,46]. Recoupling sequences that have been used to transfer magnetization include REDOR[47], TEDOR[48], LG-CP-MAS[49], REPT[50].

PRESTO (Phase-shifted Recoupling Effects a Smooth Transfer of Order) is a symmetry-based sequence used to transfer polarization [51,52]. Symmetry-based sequences are rotor-synchronized RF pulses developed by Levitt and co-workers to restore certain desired interactions whilst removing the other interactions[34,53-58].

The rotational properties of the nuclear spin interactions can be described by their ranks with respect to rotation of the static magnetic field, rotation of the molecule (space), and rotation of the nuclear spin. Every rank has components, for example space rank l has $2l+1$ components with the m index running in integer steps from $-l$ to $+l$. Table 2.1 summarize the nuclear spin interactions according to spin and space rotational ranks and their components.

Table 2.1 Spin and space ranks and their components, which describe the rotational properties of the nuclear, spin interactions in the case of exact magic-angle spinning

Interactions	Space rank (l)	Space component (m)	Spin ranks (λ)	Spin component (μ)
Isotropic chemical shift	0	0	1	{−1, 0, 1}
Chemical shift anisotropy	2	{−2, −1, 1, 2}	1	{−1, 0, 1}
Isotropic *J*-coupling	0	0	0	0
Dipole-dipole coupling	2	{−2, −1, 1, 2}	2	{−2, −1, 1, 2}

An average Hamiltonian containing the desired combinations of quantum numbers $\{l, m, \lambda, \mu\}$ can be generated or suppressed by using the symmetry-based sequences $\mathrm{R}N_n^{\nu}$ and $\mathrm{C}N_n^{\nu}$. To achieve that, the $\mathrm{R}N_n^{\nu}$ sequence has to be rotor-synchronized in such a way that N R pulses are applied exactly in n rotor periods, where each R pulse is an effective π pulse. The phase of each R pulse is alternated between $+\varphi_R$ and $-\varphi_R$ where $\varphi_R = (\pi\nu)/N$. The resulting average Hamiltonian will be:

$$H_{lm\lambda\mu} = 0 \quad if \quad mn - \mu v \neq Z_\lambda \frac{N}{2} \tag{2.4}$$

where Z_λ is an integer with the same parity as λ. Therefore, by choosing the sequence, a desired term can be recoupled or decoupled. For instant, $\mathrm{R}18_1^7$, $\mathrm{R}12_5^4$, $\mathrm{R}20_1^8$, $\mathrm{R}18_2^5$ symmetries can be used to recouple terms corresponding to $\{l, m, \lambda, \mu\} = \{2, \pm 2, 1, \pm 1\}$ which are the CSA and heteronuclear dipole-dipole interactions. PRESTO sequences using some of the $\mathrm{R}N_n^\nu$ symmetries have been used to enhance signal of spin ½ and half integer spin nuclei [51,52].

2.4 Numerical Simulation of Solid State NMR

Solid state NMR has undergone a tremendous evolution in the last few decades. It has been performed in one dimension and multiple dimensions with simple pulse or complicated pulse sequences to achieve more information about structure. Therefore, numerical simulations are needed to extract structural parameters from the data, for the design of new pulse sequences, and for understanding the theoretical concepts. In 1992 the first reasonably general NMR simulation software was implemented which is called ANTIOPE[59] . Two years later Smith *et al* reported new simulation approach called GAMMA using C^{++} software[60]. In 2000 Bak *et al.* reported a more general solid state simulation software with a simple user interface based on the Tcl language (SIMPSON)[61], which has been widely adopted in the NMR community. More recently SPINEVOLUTION software has been released[62]. In 2011 Hogben *et al.* developed a new approach of simulation, the *Spinach* library, written using the Matlab software[63]. All these programs have pros and cons, based on speed, generality, ease of use etc. Some of them are open-source and freely available for users and some of them not. Some of these softwares have been used in this thesis, like *Spinach* (paper 2, 3, 4) and SPINEVOLUTION (paper 1). In addition SIMPSON has been used to test some experiments like PRESTO-II on ^{15}N but data are not shown here.

Chapter 3: Quadrupolar Nuclei

3.1 Introduction

The nuclear interactions to consider in solid state NMR are quadrupolar, dipole–dipole coupling, chemical shift, and indirect coupling (*J*-coupling). Although, these interactions are in general anisotropic, MAS and decoupling methods average out some of their orientation dependence, especially for those interactions with low magnitude compared to the spinning frequencies. Unfortunately, the high magnitude of the quadrupolar interactions (a few kHz to a few MHz leading up to 2000–3000 MHz in the case of ^{127}I)[64] makes these techniques unable to average out these interactions effectively. Nuclei with spin > ½ have a quadrupole moment and according to their spin quantum number, these nuclei can be divided to two classes.

1- Quadrupolar nuclei with integer spin number, like ^{2}H and ^{14}N with spin number 1 and ^{10}B with spin number 3.
2- Quadrupolar nuclei with half-integer spin number, like ^{23}Na, ^{87}Rb and ^{11}B with spin number 3/2 and ^{17}O and ^{27}Al with spin number 5/2.

The nuclear quadrupole moment interacts with the electric field gradient and this interaction shifts the Zeeman energy levels significantly. EFG is a tensor and it is affected by the local electronic environment and symmetry of the chemical bonds about the nucleus. Therefore, information about the molecular structure and the chemistry of a molecule can be investigated by characteristics of the EFG. The EFG tensor is a second rank tensor and it can be given as:

$$V = \begin{bmatrix} V_{xx}^{PAF} & 0 & 0 \\ 0 & V_{yy}^{PAF} & 0 \\ 0 & 0 & V_{zz}^{PAF} \end{bmatrix} \qquad (3.1)$$

where V_{nn}^{PAF} are the principal values of the tensor and PAF is the principal axes frame of the nucleus. The summation of V_{xx}^{PAF}, V_{yy}^{PAF} and V_{zz}^{PAF} is zero (traceless tensor with no isotropic term) and $|V_{zz}^{PAF}| \geq |V_{yy}^{PAF}| \geq |V_{zz}^{PAF}|$. Therefore, only two independent parameters are needed.

1- Quadrupolar coupling constant (C_Q), expressed as:

$$C_Q = \frac{eQV_{zz}^{PAF}}{h} \tag{3.2}$$

2- Quadrupolar asymmetry parameter (η_Q) expressed as:

$$\eta_Q = \frac{V_{xx}^{PAF} - V_{yy}^{PAF}}{V_{zz}^{PAF}} \tag{3.3}$$

The quadrupolar interaction depends on the orientation of the EFG tensor with respect to the magnetic filed and the principal values of the tensor. The quadrupolar interaction vanishes when $V_{xx}^{PAF} = V_{yy}^{PAF} = V_{zz}^{PAF}$, like in the ^{14}N NMR spectrum of the NH_4Cl powdered, as in this case the tensor is spherical.

The shift of the Zeeman energy levels caused by the quadrupolar interactions depends on the size of this interaction and the spin quantum number. In general, these lead to a significant line broadening of the NMR signal in a powder sample. In addition, the presence of more than two energy levels complicates the spin dynamic. Fig. 3.1 shows the effect of the First Order Quadrupolar Interaction (FOQI) and Second Order Quadrupolar Interaction (SOQI) on spin-1 (A) and spin-3/2 quadrupolar nuclei (B).

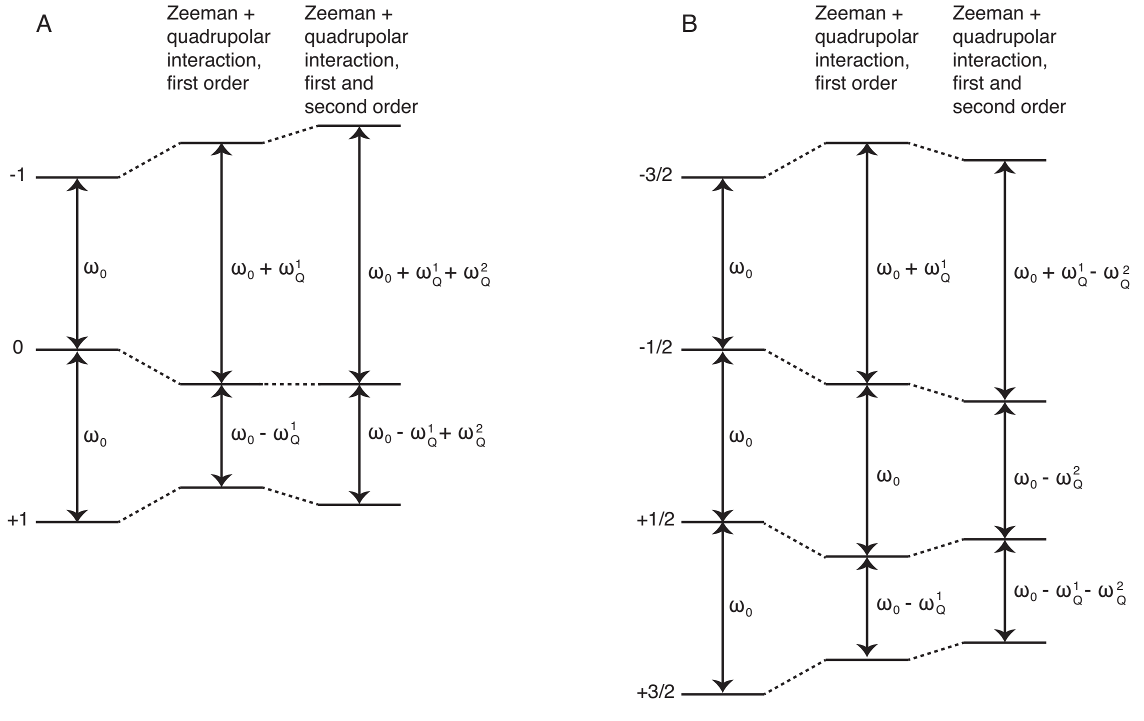

Fig. 3.1 Energy levels of quadrupolar nuclei in the presence of Zeeman field, FOQI and SOQI, (A) spin-1 nuclei (B) spin-3/2 nuclei.

In the case of integer spins, the fundamental transitions ($\Delta m = \pm 1$) are all affected by the FOQI and SOQI. However, the overtone transition ($\Delta m > \pm 1$) is affected by the SOQI but not the first order for a spin 1 nucleus. On the other hand, in the case of half-integer spin quadrupolar nuclei, the $m \leftrightarrow -m$ transitions are not affected by FOQI but they are affected by SOQI. The transition at the centre ($1/2 \leftrightarrow -1/2$) is called central transition. This single-quantum transition is a great advantage of half-integer spin quadrupole nuclei over integer quadrupolar nuclei, as it is not broadened by FOQI. However, the satellite transitions ($\Delta m = \pm 1$ but not $m \leftrightarrow -m$) are affected by both the FOQI and SOQI.

3.2 The Quadrupolar Hamiltonian

The quadrupolar Hamiltonian in the laboratory frame can be expressed with the notation of irreducible tensor operators as[65]:

$$H_Q = \omega_Q \sum_{q=-2}^{2} (-1)^q \, T^Q_{2,q} V^{\,Q}_{2,-q} \tag{3.4}$$

where ω_Q is the quadrupolar frequency, expressed as:

$$\omega_Q = \frac{2\pi C_Q}{2I(2I-1)} \tag{3.5}$$

T^Q are the irreducible spherical tensor operators for the nuclear spin, given by:

$$\begin{gathered} T^{\,Q}_{2,0} = \sqrt{\frac{1}{6}}\left[3I_z^2 - \left(I_x^2 + I_y^2 + I_z^2\right)\right] \\ T^{\,Q}_{2,\pm1} = \pm\frac{1}{2}\left[I_\pm I_z + I_z I_\pm\right] \\ T^{\,Q}_{2,\pm2} = \frac{1}{2} I_\pm^2 \end{gathered} \tag{3.6}$$

and V^Q is the EFG spherical tensor in the laboratory frame which describes the orientation dependence of this interaction. The EFG spherical tensor in the laboratory frame can be determined by rotating the EFG tensor from its principal axes frame into the laboratory frame using the Wigner matrix elements $D^{\,m}_{q',q}(\alpha,\beta,\gamma)$, where (α,β,γ) are the Euler angles[66]:

$$V^{\,Q}_{2,q} = \sum_{q'=-2}^{2} D^{\,(2)}_{q',q}\,(\alpha,\beta,\gamma)\,\rho^{\,Q}_{2,q'} \tag{3.7}$$

where ρ^Q are the coefficients of the EFG spherical tensors and they are:

$$\rho^{Q}_{2,0} = \sqrt{\frac{3}{2}}$$

$$\rho^{Q}_{2,\pm 1} = 0 \tag{3.8}$$

$$\rho^{Q}_{2,\pm 2} = \frac{1}{2}\eta_Q$$

The Wigner matrix $D\ (\alpha, \beta, \gamma)$ can be used also to transfer the principal axis frame to the rotor axis frame when MAS is applied:

$$V^{Q}_{2,q} = \sum_{q''=-2}^{2} D^{(2)}_{q'',q}\ (\omega_r t, \theta_{MAS}, 0) \sum_{q'=-2}^{2} D^{(2)}_{q',q''}\ (\alpha, \beta, \gamma)\ \rho_{2,q'} \tag{3.9}$$

The full Hamiltonian for the quadrupole spin-*I* is the summation of the Zeeman interaction and the quadrupolar interactions, as:

$$H = H_Z^I + +H_Q^I \tag{3.10}$$

The Zeeman interaction is typically much larger than the quadrupolar interactions and the quadrupolar interactions can be often considered as a large perturbation to the Zeeman interaction. Often the perturbation is so significant that it is not sufficient to consider just the first term in perturbation theory, and higher order terms arise from this. Let us expand on this aspect and see where some of the higher order terms originate. The effect of the Zeeman interaction can be formally removed from the equations describing the NMR Hamiltonian, by moving into a frame rotating with rate of ω_0 around the *z*-axis of the laboratory frame. This frame is called rotating frame and the Hamiltonian of the quadrupolar nuclei in this frame can be expressed as:

$$H_Q(t) = \omega_Q \sum_{q=-2}^{2} (-1)^q\ T^{Q}_{2,q} V^{Q}_{2,-q}\ e^{+i\omega_0 t q} \tag{3.11}$$

The full Hamiltonian quadrupolar interactions is:

$$H_Q^{full} = H_Q^{(1)} + H_Q^{(2)} + \cdots \tag{3.12}$$

Using Average Hamiltonian Theory (AHT)[65-67] the first- and second-order quadrupolar couplings can be given as[64,68,69]:

$$H_Q^{(1)} = \omega_Q T_{2,0}^Q V\,{}^{Q}_{2,0} \tag{3.13}$$

$$H_Q^{(2)} = -\frac{{\omega_Q}^2}{\omega_0}\left\{V\,{}^{Q}_{2,-1}\,V\,{}^{Q}_{2,1}\left[T_{2,-1}^Q\,T_{2,1}^Q\right] + V\,{}^{Q}_{2,-2}\,V\,{}^{Q}_{2,2}\left[T_{2,-2}^Q\,T_{2,2}^Q\right]/2\right\} \tag{3.14}$$

These Hamiltonians can be rewritten under MAS and after using Clebsch-Gordan coefficients[70,71] to expand the V^Q which contain Wigner matrix elements as:

$$H_Q^{(1)} = \omega_Q T_{2,0}^Q \sum_{q=-2}^{2} D\,{}^{(2)}_{q,0}\left(\alpha_r, \beta_r, \gamma_r\right) \rho_{2,q}\, d\,{}^{(2)}_{0,0}(\theta_{MAS}) \tag{3.15}$$

$$H_Q^{(2)} = -\frac{{\omega_Q}^2}{\omega_0} \sum_{l=0,2,4} C_l(I, I_z) \times \sum_{q=-l}^{l} D\,{}^{(2)}_{q,0}\left(\alpha_r, \beta_r, \gamma_r\right) a\,{}^{(2)}_{l,q}\, d\,{}^{l}_{0,0}(\theta_{MAS}) \tag{3.16}$$

where $d\,{}^{l}_{0,0}$ is reduced rotation matrix and it can be given as:

$$d\,{}^{l}_{0,0}(\theta_S) = \mathrm{P}_l(cos\theta) \tag{3.17}$$

where $\mathrm{P}_l(cos\theta)$ is the Legendre polynomial of rank l.

It is important here to mention that in addition to the isotropic chemical shift, the peak position is also shifted by the Second Order Quadrupolar Shift (SOQS)[72,73], which originates from the second order quadrupolar Hamiltonian contribution and it is given by[74]:

$$\delta_Q^{iso} = \left\{-\frac{3}{40}\left(\frac{2\pi\chi_q}{\omega_0}\right)^2 [I(I+1) - 9m(m-1) - 3]/I^2(2I-1)^2\right\} \times 10^6 \tag{3.18}$$

where the χ_q is:

$$\chi_q = C_q\sqrt{1+\eta^2} \tag{3.19}$$

which means that the shift depends both on the quadrupole coupling and the Larmor frequency, hence on the magnetic fireld.

3.3 High Resolution solid state NMR of Quadrupolar Nuclei

3.3.1 Magic Angle Spinning (MAS)

MAS is an invaluable technique to average out the anisotropic interactions associated with second rank tensors in solid state NMR. As has shown in Eq. (3.15) the FOQI has a second rank orientation dependence term ($d^{(2)}_{0,0}$). Therefore, MAS technique has a significant effect to average out the anisotropic interactions, which comes from the FOQI. . SOQI has also orientation dependence, but the associated term $d^{l}_{0,0}$ in the Eq. (3.16) contains isotropic, second and fourth rank contributions. The second rank term may be averaged out completely using fast spinning frequency at magic angle. However, the fourth rank is modulated but not averaged out by MAS even with very rapid spinning frequency. For example, Fig. 3.2 shows the effect of the MAS on the central transition, which is affected just by the SOQI.

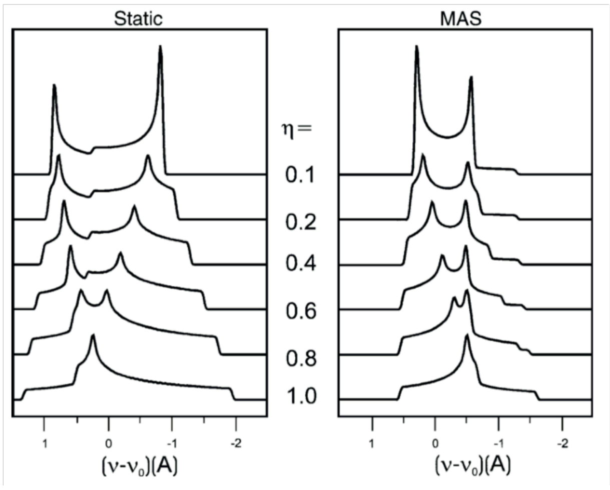

Fig. 3.2 Simulation of the central transition lineshape of half-integer quadrupole nuclei under MAS and static conditions. (Reprinted from Ref[64])

3.3.2 Double Rotation (DOR)

As already shown in Eq. (3.16), the SOQI has an orientation dependence term and this term is determined by the second and fourth rank of Legendre polynomials. The second rank term can be expressed as:

$$\mathrm{P}_2(cos\theta) = \frac{1}{2}(cos^2\theta - 1) \qquad (3.20)$$

Therefore this term is averaged out if the sample is rotating at the magic angle (54.74^o) with respect to the magnetic field. On the other hand, the fourth rank Legendre polynomial can be expressed as:

$$P_4(cos\theta) = \frac{1}{8}(35cos^4\theta - 30cos^2\theta + 3) \qquad (3.21)$$

This term is scaled down at the magic angle. However, using other angles for sample rotation leads to complete averaging of this term, namely 30.30^o and 70.12^o. Fig. 3.3 shows how the second and fourth rank Legendre polynomials values change with changing the rotation angle.

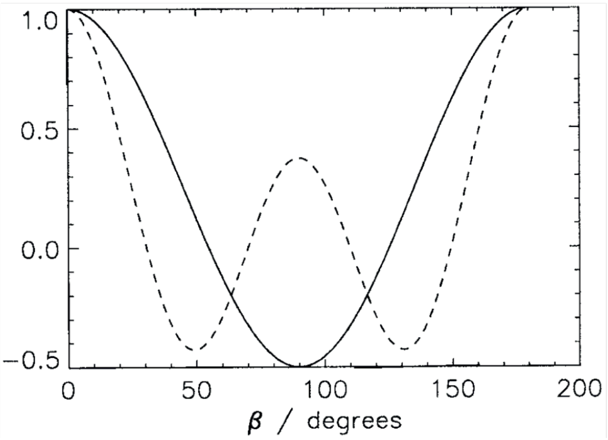

Fig. 3.3 Plot of the second (solid line) and fourth rank (dashed line) Legendre polynomials as a function of the rotating angle. (Reprinted from Ref[8])

Experimentally, averaging out of both the second and fourth rank Legendre polynomials was achieved by rotating the sample about these two angles ((54.74^o) and (30.30^o or 70.12^o)) at the same time using the Double Rotation (DOR) technique[75,76]. In order to achieve that, two rotors are set spinning, one inside the other (Fig. 3.4).

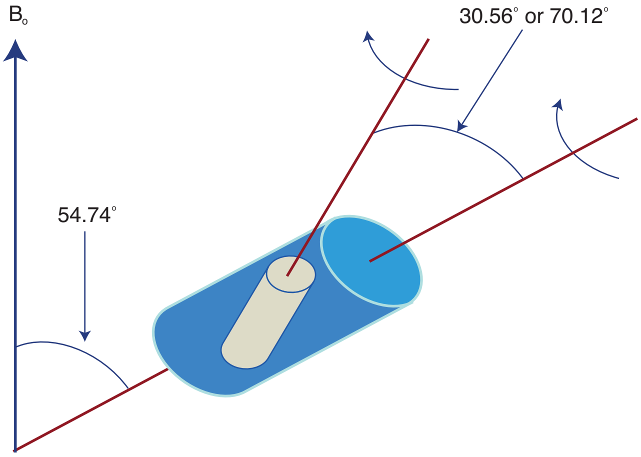

Fig. 3.4 Schematic presentation of the DOR set-up.

The spinning frequency which can be obtained in such a DOR probe is not very fast though, which leads to a number of spinning sidebands. The performance of this method is better at high magnetic field because the anisotropic quadrupolar line broadenings are reduced under these conditions, which reduces the number and the intensity of the spinning sidebands.

3.3.3 Dynamic Angle Spinning (DAS)

The Dynamic Angle Spinning (DAS) technique[77-79] averages out the Legendre polynomials of second and fourth rank by rotating the sample not simultaneously at two angles. It is a 2D experiment set up in such a way that one dimension presents the isotropic signal and the other dimension presents the anisotropic quadrupolar broadening. This can be implemented by applying a $\pi/2$ pulse to generate coherence under spinning at the first angle than evaluate this coherence under anisotropic quadrupolar broadening during t_1, then change the spinning angle to the second angle and applying a $\pi/2$ pulse then evaluate in multiples of t_1. By incrementing t_1, a 2D experiment can be obtained.

Since rotating the sample simultaneously about the two angles is not simple, one rotor at time can be used in the DAS and this is the advantage of DAS against DOR because higher spinning frequency can be achieved which leads to remove spinning sidebands. However none of the angle pairs for DAS is the magic angle, thus interactions like anisotropic chemical shift and dipolar couplings can not be averaged out completely.

3.3.4 Multiple Quantum Magic-Angle Spinning (MQMAS)

Both the DOR and DAS techniques are mechanical techniques to remove the line broadening of the SOQI by manipulating the spatial part of the Hamiltonian. New ways have been invented to remove the line broadening of the SOQI by manipulating both spatial and spin parts of the Hamiltonian. The first work was reported by Frydman and coworkers in 1995 which is Multiple Quantum Magic Angle Spinning (MQMAS)[80,81]. Since this method removes the line broadening of the SOQI under MAS, it is more efficient than DAS in averaging out the second rank interactions. In addition, it is easier than DAS and DOR and it can be implemented in any modern NMR spectrometer. MQMAS is a 2D experiment, which presents the quadrupolar line broadening in the first dimension and the isotropic peak shape in the second dimension. Fig. 3.5B shows an example of MQMAS spectra of ^{23}Na. MQMAS achieves a similar target as DAS, by refocusing the evolution during t_1 in a second period with is related to t_2 using strong pulses to excite multiple quantum coherence.

3.3.5 Satellite Transition Magic-Angle Spinning (STMAS)

The second pulsed method to achieve high resolution spectra of half integer quadrupolar nuclei was invented by Gan, which is known as Satellite Transition Magic Angle Spinning (STMAS)[69,82]. This is also a 2D experiment, which provides the quadrupolar line broadening in the first dimension and the isotropic peak shape in the second dimension after shearing FIDs. Fig. 3.5A shows an example of a STMAS spectrum for the case of ^{23}Na. The STMAS experiment correlates the satellite and the central transitions to generate coherence transfer echoes and isotropic NMR spectra in a similar way to the MQMAS experiment.

Both STMAS and MQMAS work in the central transition, which in not present for integer quadrupolar nuclei.

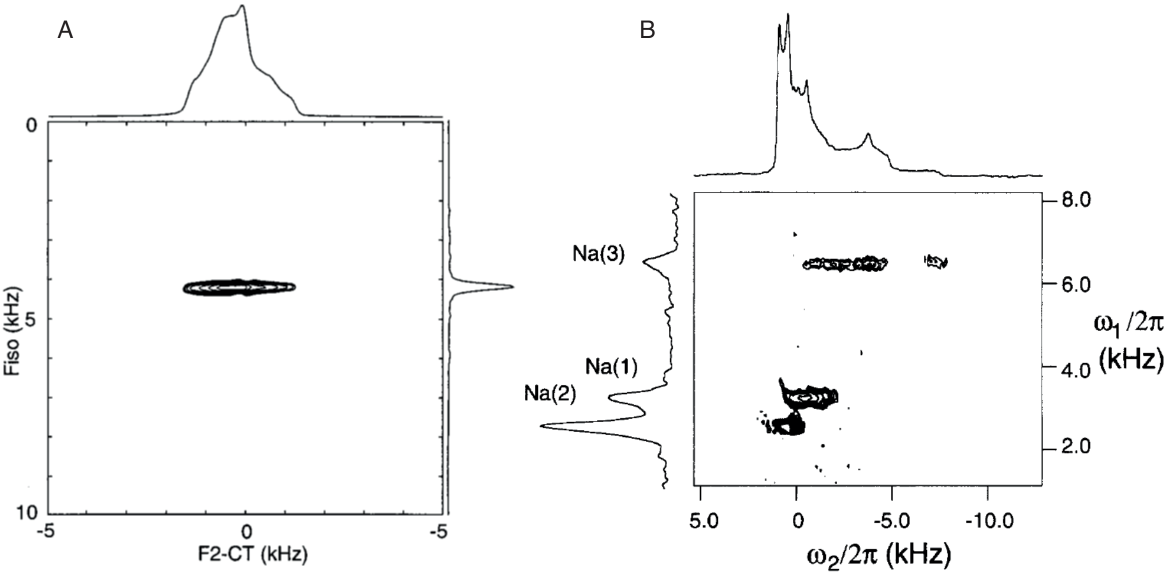

Fig. 3.5 (A) 2D STMAS spectra of Na_2SO_4 (B). 2D 3Q-MAS spectra of Na_2HPO_4. (Reprinted from Ref[69,83])

3.3.6 Sensitivity Enhancement on Quadrupole Nuclei

Many quadrupolar nuclei, which are interesting to study, have high natural abundance. For example, ^{27}Al, ^{23}Na have 100% and ^{14}N has 99.63% natural abundance[84]. However, some of them with low natural abundance (like ^{17}O which 0.038% natural abundance) or low gyromagnetic ratio are particularly challenging. Therefore, polarization transfer may be beneficial in some cases. Conventional cross polarization as used for spin-1/2 can be used to transfer magnetization to quadrupolar nuclei, with a small difference. The Hartmann-Hahn matching condition for the quadrupolar nuclei might be different than it is for spin ½ nuclei. This is because the nutation frequency on the quadrupolar nuclei is (1/2+*I*) ω_1 in case of the $\omega_1 \ll \omega_Q$. However, if the size of the quadrupolar interaction is very small or if the RF nutation frequency is too high ($\omega_1 \gg \omega_Q$) then the Hartmann-Hahn matching condition is the same as that for the spin-1/2 case. Other techniques have been adopted to enhance the NMR signal of quadrupolar nuclei, like Spin Population Transfer (SPT)[85,86] and Rotor-Assisted Population Transfer (RAPT)[87,88]. Recently, symmetry-based sequences have been used to transfer polarization from spin-1/2 nuclei to quadrupolar nuclei[51,52].

Chapter 4: Nitrogen-14 NMR

4.1 Introduction

Nitrogen is one of the most abundant elements in our solar system. It plays a significant role in sciences, like materials science, chemistry, biochemistry and pharmaceutical chemistry. In biochemistry, nitrogen plays important structural and functional roles in both proteins and nucleic acids.

Nitrogen has two NMR active isotope nuclei; ^{14}N has spin I=1, an electric quadrupolar moment of about 2.044 $\times 10^{-28}$ m^2 and 99.63% natural abundance, and ^{15}N has spin I=1/2 and has 0.37% natural abundance. The fact that ^{15}N has spin-1/2 leads to intrinsically sharper lines and ease of manipulation that makes it easier to study with high resolution in solid state NMR. The linewidth of ^{15}N in powdered glycine (Fig. 4.1C) is a few tens of Hz, instead the linewidth of ^{14}N in powdered glycine (Fig. 4.1A) is much broader (hundreds kHz). However, the low natural abundance of ^{15}N leads to a poor sensitivity. Although the poor sensitivity of ^{15}N can be overcome by isotopic labelling, this technique is expensive and moreover isotopic labelling is not always possible.

On the other hand, the electric quadrupolar moment of non-symmetrical ^{14}N nuclei in many materials containing nitrogen gives rise to large quadrupolar interactions (often in the MHz range). The line broadening of ^{14}N NMR spectra is due to these large quadrupolar interactions and this is the main disadvantage of ^{14}N solid state NMR. However, the large ^{14}N quadrupolar interaction is advantageous in some cases because it provides valuable information regarding the conformation and molecular dynamics. It provides a tool for the investigation of structure and dynamics of biomolecular systems. Another advantage of ^{14}N NMR is that its fast T_1 relaxation allows for quick scan repetition, hence more scans per unit time than what is typically used for spin ½ species.

The ^{14}N signal is distributed over several MHz due to the large quadrupolar interactions, with the single quantum transitions shifted well off the Larmor frequency[5,89,90]. In addition to the large quadrupolar interactions of ^{14}N, unlike the half-integer spin quadrupolar nuclei[64,69] spin-1 nuclei do not have a central transition which is unaffected by the FOQI. In addition to the lineshape perturbation of ^{14}N from the FOQI, also the SOQI and the CSA contribute to the overall width of the ^{14}N lineshape. Fig. 4.2 shows the Zeeman energy levels perturbed by the quadrupolar interactions and the CSA.

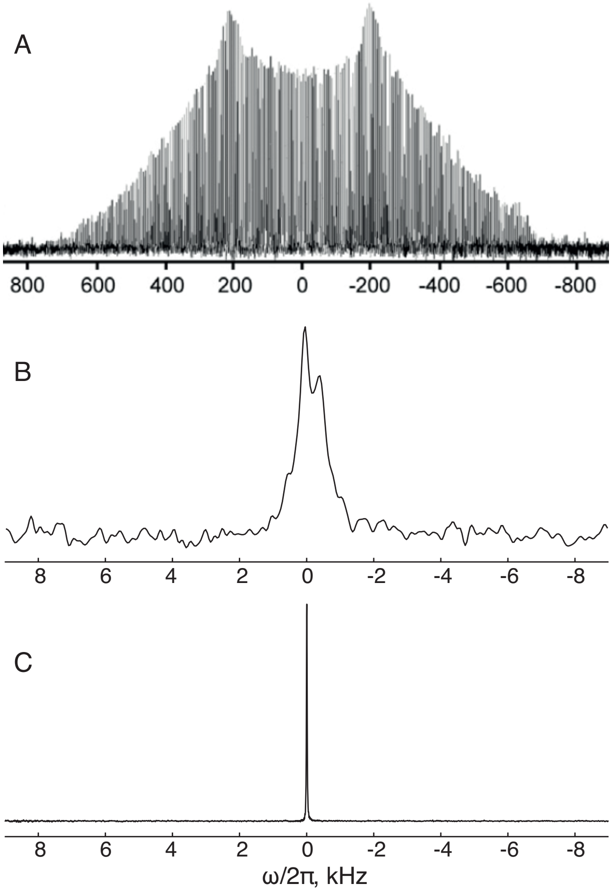

Fig. 4.1 NMR spectra of powdered glycine at 14.1 T (A) acquired in 44 h at a MAS rate of 6 kHz. (B) Direct excitation of ^{14}N overtone transition of glycine acquired with 1024 scans, 260 μs pulse length, 55 kHz nutation frequency on resonance with +2 spinning sideband at 19.840 kHz spinning frequency. (C) ^{15}N CP NMR spectrum of powdered ^{15}N labelled glycine acquired at 20 kHz spinning frequency. ((A) Reprinted from Ref[91])

Therefore, many ^{14}N studies have focused on the nitrogen sites with high symmetry, which have a small quadrupolar coupling (<100's kHz) or single crystal studies[8,89,92-96]. In addition, adiabatic excitation schemes have proved effective at exciting the broad spectra of ^{14}N sites with quadrupolar interactions up to 1 MHz[97]. For ^{14}N sites with large quadrupolar interactions (>1 MHz), direct detection to reproduce the quadrupolar lineshape have been employed using broadband excitation pulses[91,98,99] or step-wise acquisition[89,100,101].

Recently, a new approach has been developed independently by Gan[73,102] and Cavadini[103,104]. This technique was developed from Heteronuclear Multiple Quantum Coherence (HMQC) transfer and Heteronuclear Single Quantum Coherence (HSQC) transfer experiments, which were already used in liquid state NMR. Indirect detection of the ^{14}N NMR signal using a spy nearby spin-1/2 nucleus (typically ^{1}H or ^{13}C) can be achieved with this approach. Coherence transfer between the ^{14}N and the spy spin-1/2 nucleus are performed using a range of pulse sequences[5,102-113]. In addition to the *J*-coupling, the second-order quadrupolar-dipolar interactions that are not averaged by MAS, sometimes called residual dipolar splitting (RDS), transfer coherences to spin-1/2 nucleus[5,102-113]. Also the dipole-dipole interaction can be used to transfer coherence using suitable recoupling methods[112,114]. An alternative approach to detect ^{14}N NMR signal was developed, following the observation of the overtone transition which corresponds to the change in spin projection quantum number by $\Delta m = 2$ with direct detection at twice the Larmor frequency[115]. In general this transition is forbidden, but the presence of a large quadrupolar interaction in the ^{14}N nuclei mixes the Zeeman energy levels that in turn makes it weakly allowed[116-118]. This transition is not affected by FOQI; thus, the overtone transition is much narrower than the fundamental transition (Fig. 4.1B).

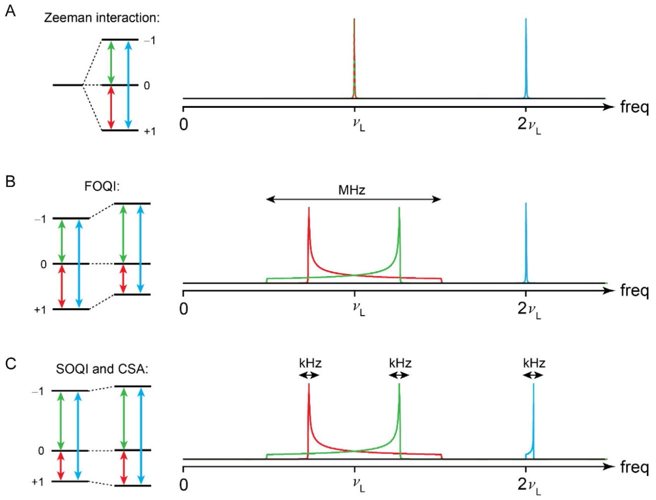

Fig. 4.2 Energy levels of spin-1 nuclei (A) Zeeman energy levels without any other interactions, (B) effect of the FOQI and (C) effect of the SOQI and CSA interactions. Red and green lines present the fundamental transitions and the blue line presents the overtone transition. (Reprinted from Ref[119])

4.2 Indirect Detection of Nitrogen-14 in Solid State NMR

Heteronuclear Multiple- or Single-Quantum Correlation (HMQC or HSQC) methods were earlier used in the beginning of 1980s for ^{15}N NMR[120,121]. At the same time, Ernst and co-workers reported that ^{14}N double-quantum coherences (DQCs) can be excited indirectly between ^{14}N and neighbouring spy nuclei[122,123]. Four years earlier Pines *et al.* reported that the frequencies of double-quantum transitions between $|m = +1>$ and $|m = -1>$ levels of ^{2}H, which has spin-1 and the same energy level structure as ^{14}N, are not affected by first-order quadrupolar interactions[124]. Thus, a new approach was developed for the indirect detection of the Single Quantum (SQ) or Double Quantum (DQ) coherence of ^{14}N transitions via suitable “spy” nuclei such as ^{1}H or ^{13}C, by transferring coherence back and forth between ^{14}N and the spy nuclei[73,102-104].

The coherence transfer occurs via RDS and J-coupling. In addition to the orientation of the EFG tensor (V) with respect to the dipolar tensor, the orientation of the crystallite with respect to the rotor axis affects the RDS. The RDS lead to a splitting of the S resonances into 1:2 doublets. The $|m = +1>$ and $|m = -1>$ states resonate at the same frequency thus they give the largest component and the $|m = 0>$ state resonates at a different frequency and it gives the smaller component. The heteronuclear scalar coupling (*J*-coupling) splits the $|m = +1>$ and $|m = -1>$ states into 1:1 doublets, and this splitting is small for ^{13}C but it is large in the case of protons. For instance the magnitude of the RDS for ^{14}N–^{1}H in glycine is about 106 Hz and the *J*-coupling is about 65 Hz[103]. Fig. 4.3 shows these splittings of $^{14}NH_3^+\ ^{13}C^{\alpha}\ HRCOO^-$ in zwitterionic amino acids at 9.4 T.

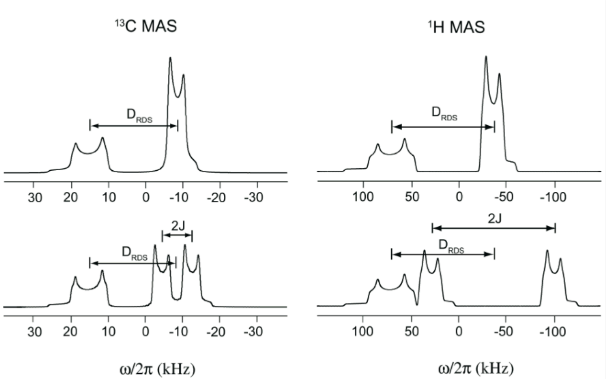

Fig. 4.3 Simulated spectra of $^{14}NH_3^+\ ^{13}C^{\alpha}\ HRCOO^-$ in zwitterionic amino acids at 9.4 T. On the top, ‘spy’ nuclei S (such as ^{13}C in the left and ^{1}H in the right) featuring only a residual dipolar splitting RDS), whereas at the bottom, a similar splitting is combined with a heteronuclear scalar coupling (*J*-coupling). (Reprinted from Ref[108])

Most of the ^{14}N HMQC and HSQC experiments in solid state NMR in the last years have been done via residual dipolar splitting (RDS) and *J*-coupling with some modification in the sequence and phases. For example, the first sequence was implemented by Gan and is shown in Fig. 4.4A. Cavadini independently implemented a similar sequnce using ^{1}H as spy nuclear instead of ^{13}C[103] (Fig. 4.4B).

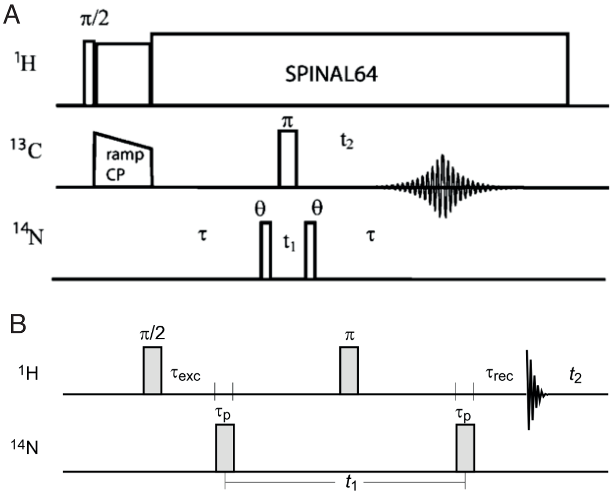

Fig. 4.4 (A)^{14}N-^{13}C coherence transfer pulse sequence (HMQC) under MAS. For completely average out of the FOQI, the magic-angle needs to be set precisely and the evolution time t_1 must be accurately rotor-synchronized. The pulse phases are chosen in such a way to select the single-quantum transition. (B) ^{14}N-^{1}H coherence transfer pulse sequence (HMQC) under MAS for coherence transfer of the indirect detection of ^{14}N single- or double-quantum spectra. (A and B Reprinted from Ref[73] and Ref[103] respectively)

HMQC is a 2D experiment that shows the direct detection of the spy nuclei in the first dimension and indirect detection of ^{14}N in the second dimension (Fig. 4.5). The ^{14}N lineshape in the second dimension is just affected by the second order quadrupolar broadening and higher order terms.

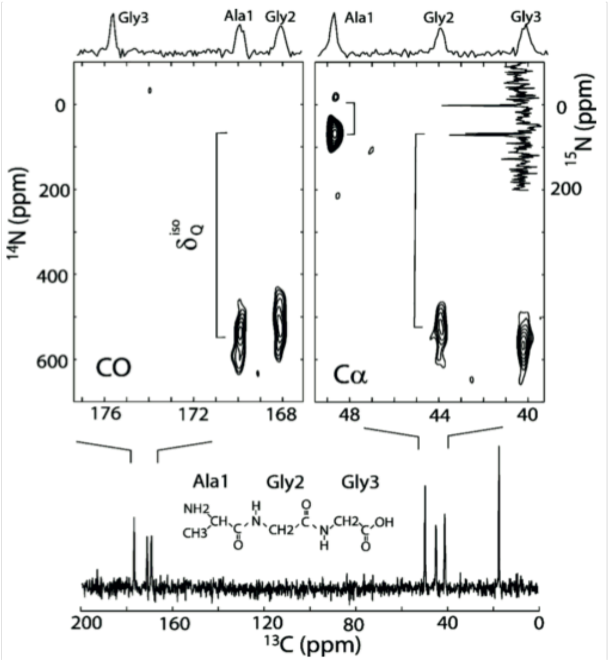

Fig. 4.5 HMQC ^{14}N-^{13}C correlation spectrum of natural abundance Ala-Gly-Gly acquired at 14.1 T, with τ = 15 ms, 25 kHz MAS, 16 t_1 increments, 8000 scans, 2 μs ^{14}N pulse with 50 kHz nutation frequency, SPINAL-64 ^{1}H decoupling with 125 kHz proton nutation frequency. The nitrogen chemical shift is referenced to solid NH$_4$Cl. (Reprinted from Ref[73])

The major challenge facing these experiments is the low efficiency of the two-way coherence transfer. The efficiency of coherence transfer can be estimated by comparing the spy signal (^{1}H or ^{13}C) obtained from using HMQC (applying nitrogen pulses) in 1D mode with the same spectrum obtained from a spin echo under the same conditions but without ^{14}N pulses, or to the direct excitation of the spy nucleus (^{1}H or ^{13}C). For example, Gan in 2007 reported experimental efficiency of 5-6% compared to a proton spin echo experiment without ^{14}N pulses[110]. Some modifications for the original sequences have been reported to increase the efficiency. For example: it has been found beneficial to add pulses to decrease the H-H interactions in order to improve the resolution, and for this purpose rotor-synchronized symmetry-based sequence and phase-modulated Lee-Goldburg (PMLG) method in the excitation and reconversion period have been used[125]. In 2011, Nishiyama *et al.* have used the $SR4_1^2$ scheme to remove H-H coupling and increase the H-N coupling with very fast magic angle spinning[112]. In addition, the two rectangular RF pulses on nitrogen have been replaced by rotor synchronized Delays Alternating with Notations of Tailored Excitation (DANTE) and overtone DANTE[126]. In 2013, Jarvis *et al.* used long nitrogen pulses (1.6-2 ms) without using excitation and reconversion intervals[111] (see further details in Paper 1). They reported experimental efficiency of 10% and 17% of the HMQC compare to direct CP and spin echo of ^{13}C respectively (Fig.4.6).

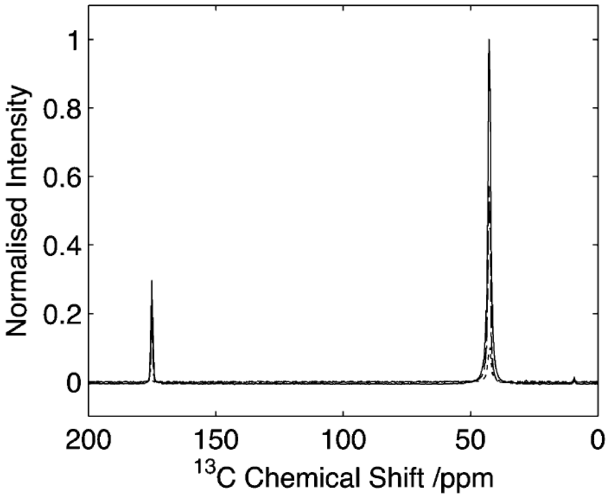

Fig. 4.6 Comparison of HMQC efficiency on U-^{13}C$_2$-glycine. Cross polarization spectrum (solid line), spin echo spectrum (dashed) and comparison to optimal transfer through ^{14}N (dotted). Data acquired at 14.1 T with 25 kHz spinning frequency, 2 ms for ^{14}N pulses and echo time and 35 kHz RF nutation frequency on the ^{14}N pulses. (Reprinted from Ref[111])

4.3 Nitrogen-14 Overtone Transition

The overtone transition is the transition corresponding to the change of the spin projection quantum number by Δm = 2. This transition was first reported in Electron Paramagnetic Resonance (EPR) studies by van der Waals and de Groot[127,128]. The ^{14}N overtone transition was observed in 1977 by Greel *et al.* using a Continuous Wave (CW) technique[129]. In 1986, Bloom and Legros reported the first direct detection NMR studies of the ^{14}N overtone transition[115]. In general, the Δm = 2 transition is not allowed, but the presence of large quadrupolar interactions mixes the $|+m>$ and $|-m>$ states, making it weakly allowed. The poor excitation efficiency is one of the most important challenges for the development of overtone NMR. Since the mixing of the states depends on the quadrupolar interaction magnitude, the probability of this transition increases for larger quadrupolar interactions. On the other hand, higher order quadrupolar interactions are associated with broader lines and hence have a negative effect on the NMR resolution.

The overtone transition is unaffected by the FOQI, which is the major advantage of this approach, as it leads to much narrower NMR lines, of the order of kilohertz (Fig. 4.1B), compared to the linewidth of the fundamental transition which is often of order of megahertz (Fig. 4.1A). The ^{14}N lineshape without FOQI can be obtained using indirect detection techniques as mentioned in section 4.2, but this approach is a direct detection technique which can be performed by exciting and detecting directly the ^{14}N NMR signal at proximately twice the ^{14}N Larmor frequency. The exact frequency of the ^{14}N overtone transition is determined by the isotropic chemical shift and the SOQS.

Bloom and Legros illustrated the first ^{14}N overtone solid state NMR experiment of single crystal material. Tycko and co-workers in the same year performed ^{14}N overtone solid state NMR experiment of *N*-acetylvaline (NAV) in both single crystal and powder[118]. They reported that the overtone transition could be excited and detected using an RF coil orientation in any direction, even parallel to the static magnetic field, which gives better lineshape (Fig. 4.7B,D). Tycko and co-workers published three papers in that time to report important developments of overtone excitation[116-118].

Unfortunately, the interest in this approach decreased by the end of the 1980s because of the low resolution and sensitivity of this transition. However, in 2011 O'Dell reported that ^{14}N overtone solid state NMR can be recorded with much higher resolution by using MAS[130]. This provided a new stimulus for this research area[90,131-135]. Although, the absence of the FOQI is promising, this technique has not became a routine experiment for detecting

^{14}N NMR because some challenges are still associated with the effective excitation of this nearly-forbidden transition.

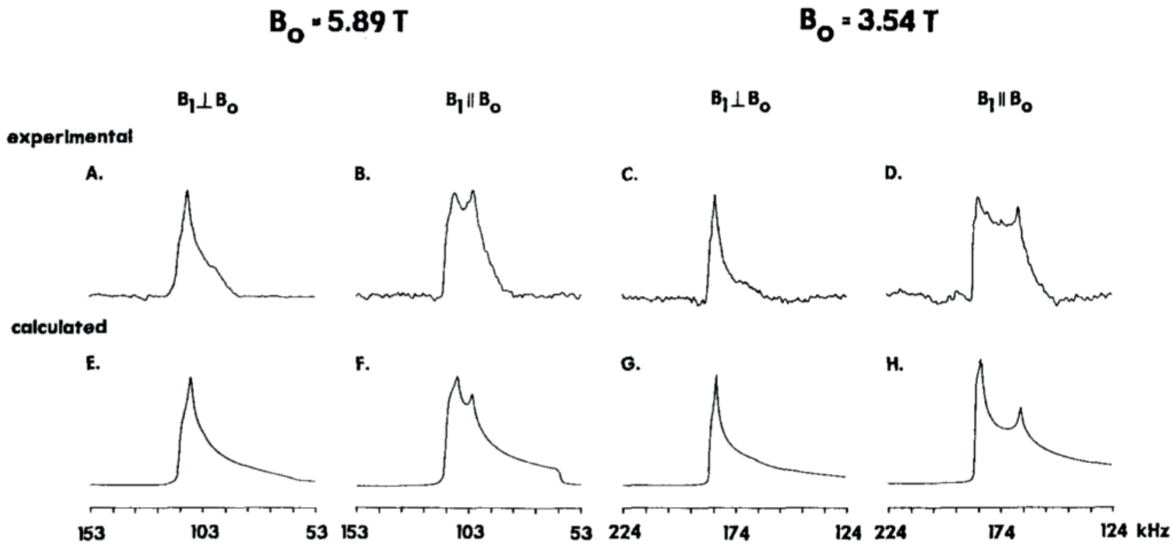

Fig. 4.7 Simulations (E, F, G, H) and experiments (A, B, C, D) for ^{14}N overtone NMR spectra of powdered NAV. Data were acquired with approximately 20000 scans using 200 mg of sample in static magnetic fields of 5.89 (A, B) and 3.54 T (C, D). The overtone RF pulse was applied and the signal detected both perpendicular (A, C) and parallel (B, D) to the static magnetic field. Simulated spectra include CSA. (Reprinted from Ref[117])

4.3.1 Nitrogen-14 Overtone Transition Under MAS

Already back in the 1980s, Tycko and Opella attempted to reduce the ^{14}N overtone linewidth by spinning the sample[117], but the results were far from satisfactory. The linewidth for powdered NAV under static conditions (Fig. 4.8A) is narrower than the linewidth under spinning at certain angles (Fig. 4.8B, C, D). In addition to the linewidth, the S/N under static conditions is better. No spectra under MAS were presented in this work.

In 1999 Marinelli *et al.* described the density matrix treatment of ^{14}N overtone transition NMR under static and spinning conditions[7]. They showed that when spinning the sample at frequency ω_r, the ^{14}N overtone signal splits into five components at (0, $\pm 1\omega_r$, $\pm 2\omega_r$). These spinning sidebands are unrelated to the familiar spinning sidebands, which are created from the modulation of anisotropic interactions. Overtone spinning sidebands are not removed or decreased no matter how fast the spinning frequency is.

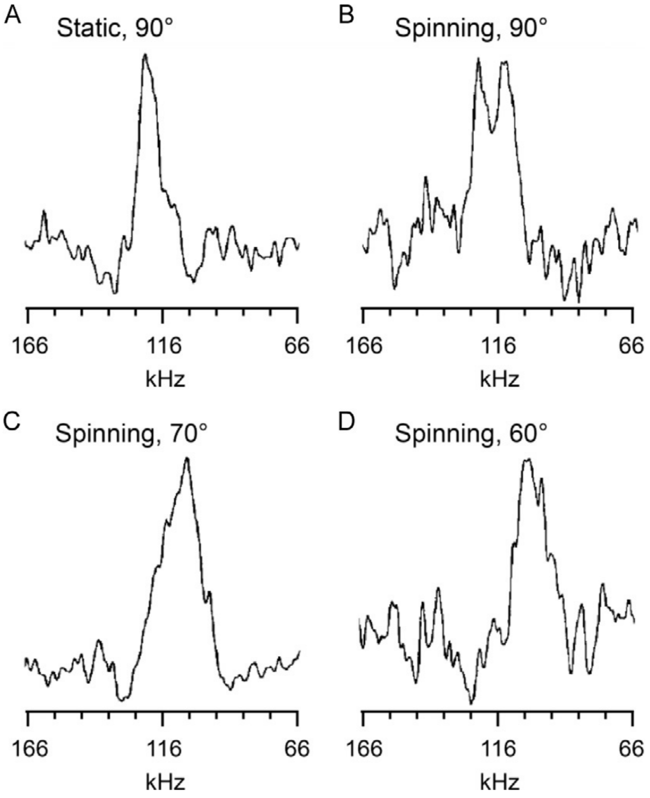

Fig. 4.8 Spin echo ^{14}N overtone NMR spectra of powdered NAV under static and spinning conditions. Data were acquired at 5.89 T with RF excitation and detection perpendicular to the magnetic field for (A, B). (A) Static condition with 45000 scans, (B) 4.8 kHz spinning frequency at a 90° angle with respect to the magnetic field with 44000 scans, (C) 4.8 kHz spinning frequency at 70° angle with respect to the magnetic field with RF irradiation and detection along the spinning axis and 159000 scans, (D) 4.8 kHz spinning frequency at 60° angle with respect to the magnetic field with RF irradiation and detection along the spinning axis and 43000 scans. (Reprinted from Ref[117])

Surprisingly, no ^{14}N overtone study under MAS was reported until 2011 when O'Dell and Ratcliffe presented the first overtone NMR study of this type[130]. They found that the signal under MAS is more intense and narrower than under static conditions (Fig. 4.9), largely due to the averaging of the CSA and the dipolar interactions.

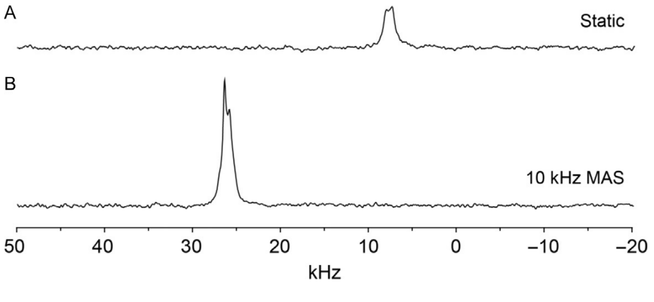

Fig. 4.9 ^{14}N overtone NMR spectra of powdered glycine acquired at 11.7 T using an on-resonance pulse with pulse length 100 μs, 0.5 s pulse recycle delay and 10000 scans. (A) Under static conditions, (B) under MAS with 10 kHz spinning frequency. (Reprinted from Ref[119])

In addition to higher resolution under MAS, they found that the peak moves linearly with spinning frequency and that it appears at a position shifted by $2\omega_r$ with respect to the centerband. Two years later O'Dell and Brinkmann reproduced this shift in the peak position though a numerical simulation of the ^{14}N overtone spectra under MAS and they found that this peak is the second spinning sideband at $+2\omega_r$. Their simulation showed that the intensity of the ^{14}N overtone centreband signal (Fig. 4.10A) decreases when the sample is rotated (peak at 6 kHz in Fig. 4.10B)[90].

Simulation also showed that the second spinning sideband is the most intense signal. They complemented their simulation with experimental data as well. The +2 spinning sideband of overtone NMR has a disadvantage, which is the peak position depends on the rate and direction of the spinning. Thus the second spinning sideband peak position of ^{14}N overtone NMR is determined by the isotropic chemical shift, isotropic SOQS, spinning frequency and direction of the spinning. However, the higher resolution of this signal compared to the centreband signal has triggered a new interested in the ^{14}N overtone transition.

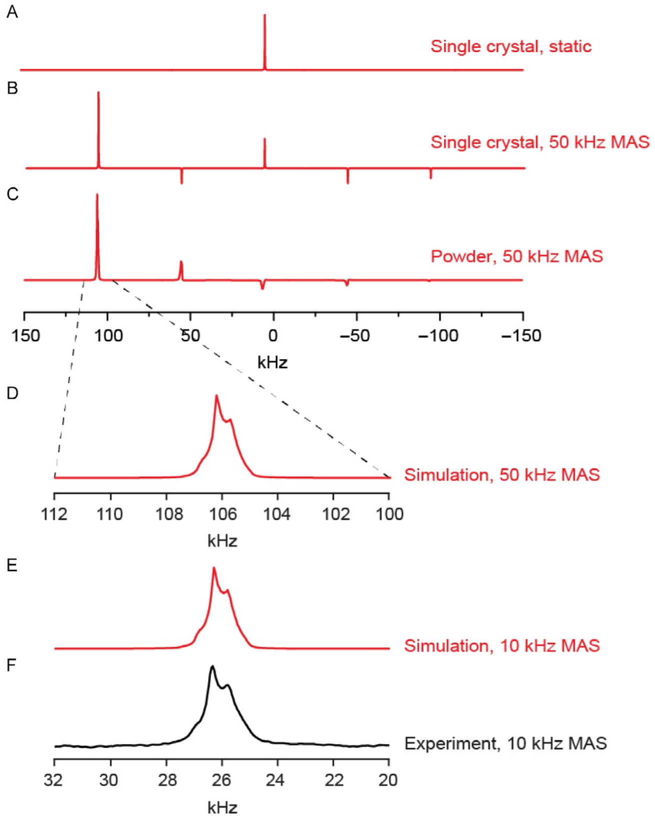

Fig. 4.10 ^{14}N overtone simulated (A, B, C, D, E) and experimental (F) NMR spectra of glycine at 11.7 T for (A) single crystal under static condition, (B) single crystal under MAS with 50 kHz spinning frequency, (C) powder sample under MAS with 50 kHz spinning frequency, (D) zoom on the $+2\omega_r$ spinning sideband, (E) $+2\omega_r$ spinning sideband with 10 kHz spinning and (F) experimental spectrum of (E). (Reprinted from Ref[90])

4.3.2 Weaknesses of Nitrogen-14 Overtone Transition

There are some challenges facing the development of this approach. The fact that this transition is only weakly allowed leads to poor signal excitation. Thus more scans are needed to get high quality spectra, for example, the ^{14}N glycine spectrum in Fig. 4.9B was acquired on a 4 mm probe with 10000 scans. Theoretically, a larger quadrupolar interaction or the use of low magnetic fields should increase states mixing, which again should increase the sensitivity of this transition. However, experimental overtone data at 14.1 T for NAV which has 3.21 MHz quadrupolar coupling[96] and 160000 scans (Fig. 4.11B) has lower signal intensity than for glycine which has 1.18 MHz quadrupolar coupling[90] at same conditions with 1000 scans (Fig. 4.11A), once scaled by the number of scans and the sample volume. Data on NAV at 20.0 T (Fig. 4.12C) show that the signal intensity is better than at lower field (Fig. 4.12B). These behaviours are somewhat contrary to the expectations based on the overtone transition probability.

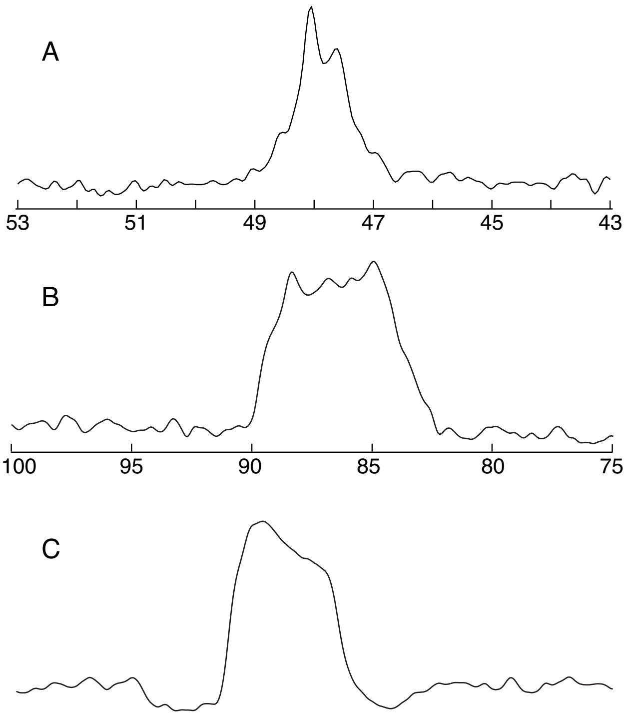

Fig. 4.11 Experimental ^{14}N overtone spectra of (A) glycine and (B, C) NAV. Data in A and B were acquired at 14.1 T with 260 μs pulse length and 55 kHz nutation frequency, 1000 and 160000 scans respectively. Data in C were acquired at 20.0 T with 275 μs pulse length and 71 kHz nutation frequency and 40000 scans. All data acquired on resonance with the second spinning sideband at 19.84 kHz spinning frequency using SPINAL-64 decoupling.

Overtone excitations with single pulses tend to be highly narrow-banded. Optimal signal excitation is only achieved with relatively long excitation pulses, because of the slow overtone nutation rates compared to the fundamental transitions, which leads to narrower excitation bandwidths. Theoretical studies[7] showed that about 25% of the ^{14}N overtone NMR coherence could be excited using 150 kHz RF nutation frequency with about 150 μs pulse length on-resonance at twice the Larmor frequency and half of this percentage can be excited when the pulse is applied with a 20 kHz off-resonance irradiation offset (Fig. 4.12).

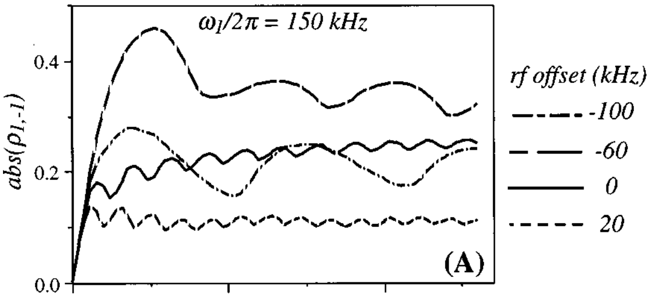

Fig. 4.12 Simulation for the nutation curve of the overtone transition as a function of RF offset. (Reprinted from Ref[7])

Unfortunately, the actual excitation efficiency is much lower and it was found that only 1% to 2% of the theoretical values can be obtained experimentally under optimal condition[7]. However, another study by O'Dell and Ratcliffe on the ^{14}N overtone second spinning sideband of powdered glycine (experimental and simulation) showed that the signal intensity goes to zero in some conditions, for example when the pulse length is 100 μs and the transmitter offset is more than 10 kHz at the conditions shown in the Fig. 4.13 caption. This study also illustrated that increasing the pulse length increases the signal intensity when the pulse is applied on-resonance. On the other hand if the pulse is off-resonance, the signal intensity decreases with increasing pulse length as regions further away from the carrier frequency start to fall outside the excitation bandwidth of the long pulse (Fig. 4.13).

Usually long pulses are needed to get optimal excitation for ^{14}N overtone signal. Therefore, the selective bandwidth and the weak resolution and sensitivity of the ^{14}N overtone signal are the major issues which need to be overcome to make this approach more routinely adopted for ^{14}N NMR studies, especially for biological studies. Typical biological materials contain multiple nitrogen sites with different chemical shift and quadrupolar interactions, thus it is impossible to obtain high resolution ^{14}N overtone NMR spectra for all nitrogen sites with a simple one pulse method for the excitation of the overtone transition.

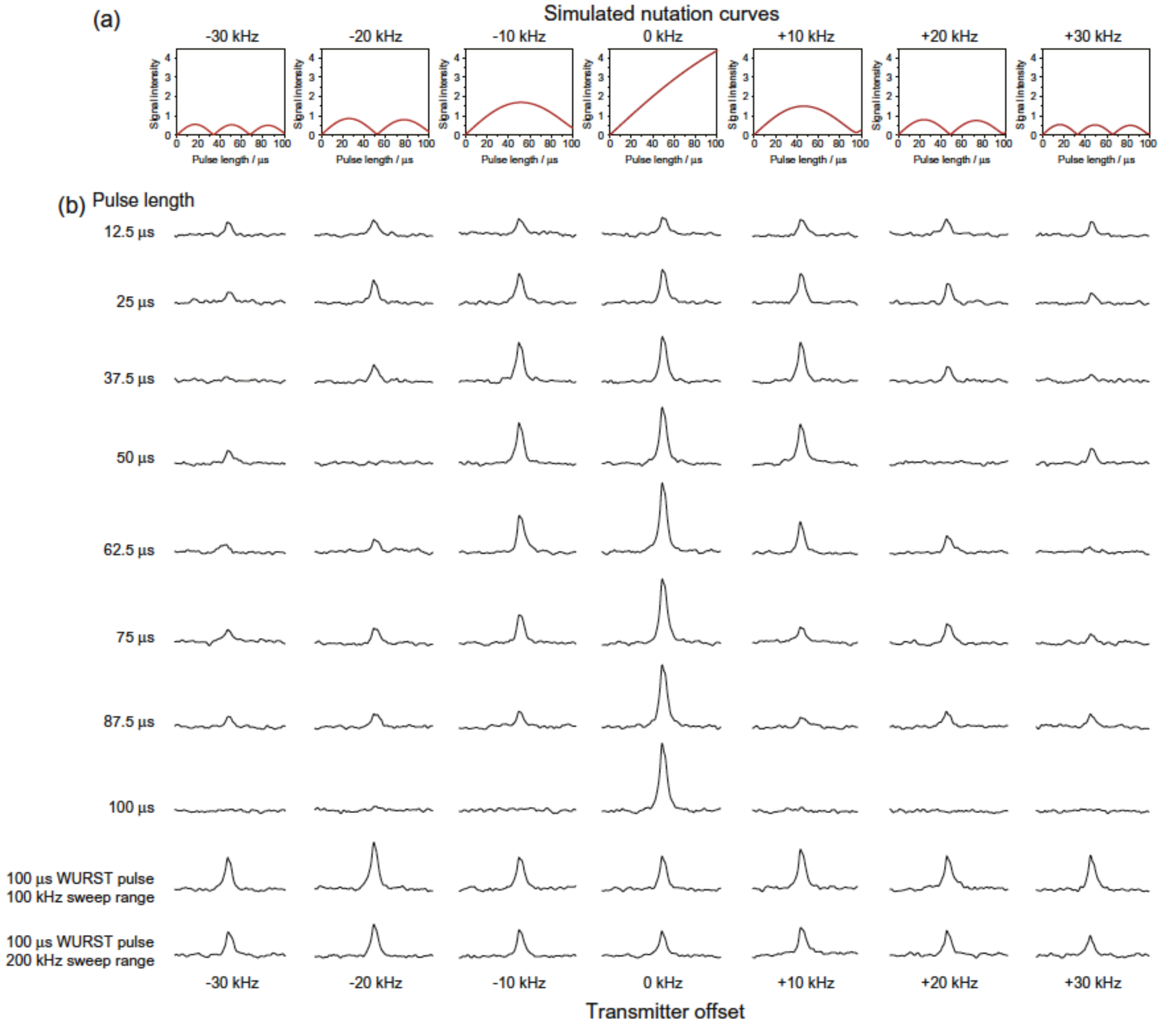

Fig. 4.13 ^{14}N overtone simulation (a) and experiments (b) of powdered glycine acquired at 11.7 T using different RF pulse offset and length with 42 kHz nutation frequencies with standard and WURST pulses. (Reprinted from Ref[130])

The^{14}N overtone linewidth, despite being immune to FOQI, is still significantly larger than typical linewidths encountered on ^{15}N measurements by orders of magnitudes due to higher orders terms. Therefore, the linewidth of ^{14}N overtone signal is about few hundred Hz for glycine but it is about few kHz for higher quadrupolar coupling nucleus, like an amide nitrogen, which has a few MHz quadrupolar coupling constant. Except from MAS methods, no technique has been reported to reduce ^{14}N overtone linewidth further. Haies *et al.* recently reported that the ^{14}N overtone linewidth can be reduced using DOR by a factor between 3 to 9 (see Paper 3).

In addition to the experimental challenges facing the overtone approach, simulation of the overtone spectra is not achievable in the common solid state NMR softwares, like SIMPSON[61] or SPINEVOLUTION[62]. For example, both of them can be used to simulate the HMQC spectra. Spinevolution has been used for the simulation of all spectra in paper

1. For overtone transitions, Tycko and Opella in 1987 calculated ^{14}N overtone spectra using their own program, which is not open source software. In 2013, O'Dell and Brinkmann simulated the ^{14}N overtone spectra using Mathematica software but this simulation needs long time and a high performance machine. A new ^{14}N overtone simulation strategy has been developed by Prof. Ilya Kuprov and his co-workers using the *Spinach* library[63]. This simulation approach is fast compared to simulation using Mathematica. Therefore, this software has been used to simulate spectra in papers 2, 3, 4 and the input files are available as part of the *Spinach* open source repository.

4.3.3 Development of Nitrogen-14 Overtone Approaches

4.3.3.1 Broadening the Excitation Bandwidth of Nitrogen-14 Overtone Transition

Although reducing ^{14}N overtone linewidths by MAS is a significant step forward, this approach is not close to be routinely adopted for nitrogen NMR studies. O'Dell and co-worker also tried to overcome the highly selective bandwidth of overtone excitation by a single pulse by using Wideband, Uniform Rate, Smooth Truncation[136-138] (WURST) pulse sequences[130,132,135]. Although the excitation bandwidth of the ^{14}N overtone transition using a simple 100 μs pulse is about 10 kHz, O'Dell and co-worker succeeded to acquire ^{14}N overtone signals of three nitrogen sites, for the case of histidine, with signals spread over a range of 50 kHz using a WURST pulse. The wide shift spread in this sample originates from a combination of different chemical shifts and SOQS (Fig. 4.14).

Application of a WURST pulse leads to a significant increase in the excitation bandwidth of the ^{14}N overtone transition, which makes analysis of materials with multiple nitrogen sites possible. However, the efficiency of ^{14}N overtone signal excitation is significantly reduced, compared to the standard (unmodulated) pulses as can be seen from Fig. 4.13 (last two rows)

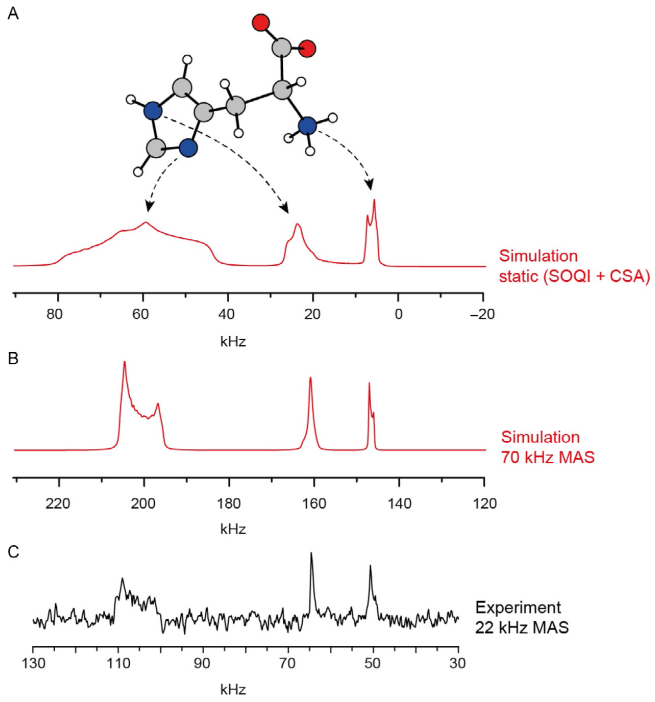

Fig. 4.14 ^{14}N overtone simulation and experimental NMR spectra of histidine at 11.7 T magnetic field. (A) Simulation under static condition including the effect of SOQI and CSA interactions. (B) Simulation under MAS with 70 kHz spinning frequency. (C) Experimental data under MAS acquired with 22 kHz spinning frequency and a WURST pulse with a 150 kHz sweep range and 65000 scans. (Reprinted from Ref[119])

4.3.3.2 Indirect Detection of Nitrogen-14 Overtone Transition

Recently, HMQC experiments were developed to be used for ^{14}N fundamental transitions by Gan [73,102] and Cavadini[103,104]. Nishiyama *et al.* in 2013 reported an extension of this approach towards ^{14}N overtone by detecting ^{14}N overtone transition indirectly using HMQC experiments. They showed that the efficiency of this experiment on the ^{14}N overtone transition for glycine with optimal conditions (Fig. 4.15c) is 1.8 times higher than efficiency of the ^{1}H-^{14}N DQ HMQC experiments at optimal conditions (Fig. 4.15b) but it is lower than that for the ^{1}H-^{14}N SQ HMQC experiments (Fig. 4.15a). However, much more precise magic angle adjustment and rotor synchronization are required for the SQ than the DQ and overtone HMQC experiments[131].

The authors also reported that all five ^{14}N overtone spinning sidebands give the same ^{1}H - ^{14}N overtone coherence transfer efficiency. This is because the ^{14}N overtone pulses were optimized on-resonance with the centreband overtone transition rather than with the spinning sidebands. O'Dell *et al.* in the same year found that optimizing the ^{14}N overtone pulses on-resonance with the second spinning sideband for ^{1}H-^{14}N overtone HMQC experiments provides shorter ^{14}N overtone pulses and higher ^{1}H -^{14}N overtone coherence transfer efficiency[132].

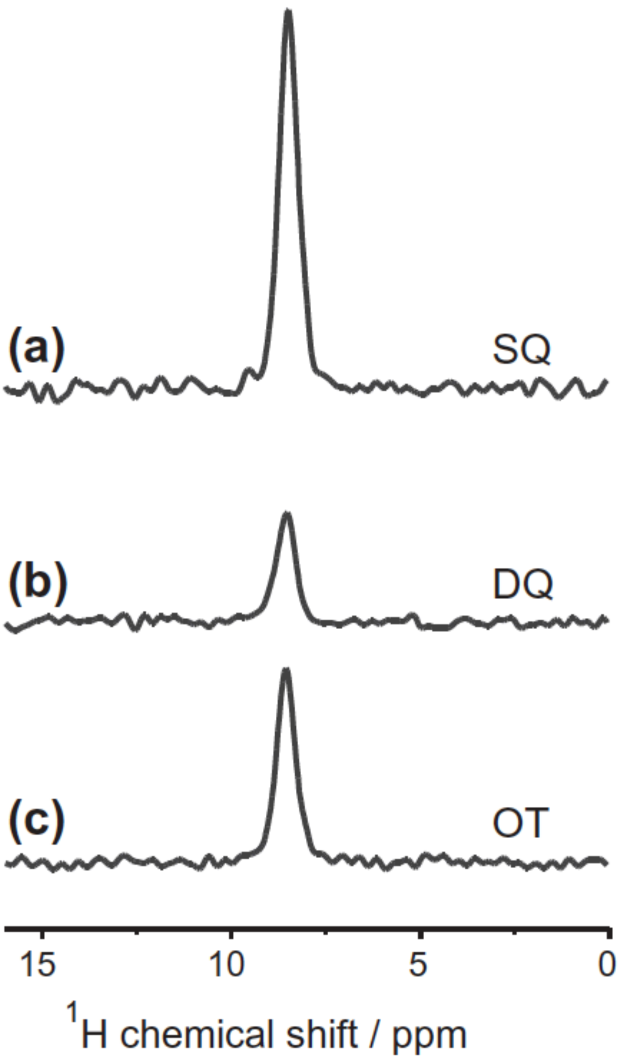

Fig. 4.15 ^{1}H HMQC filtered NMR spectra of glycine at 14.1 T under MAS with 80 kHz spinning frequency, 512 scans, the excitation and reconversion time of 600 µs. The nitrogen overtone pulses were set to 10 µs for the SQ (a), 14 µs for DQ (b) and 200 µs for the overtone experiment (c). (Reprinted from Ref[131])

In addition, O'Dell and co-workers broadened the ^{14}N overtone excitation bandwidth pulses of ^{14}N overtone HMQC experiment by using a WURST pulse during the excitation pulse or during both pulses (excitation and reconversion). They also used a ^{1}H-^{14}N overtone HMQC experiment to identifying H–N proximities and they presented ^{14}N overtone spectra of NAV indirectly in the second dimension (Fig. 4.16). This was the first ^{14}N overtone spectrum reported for ^{14}N nuclei with a quadrupolar coupling constant of more than 3 MHz under MAS[132].

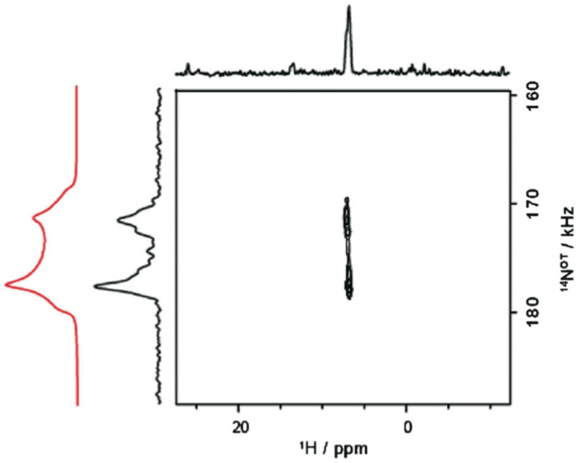

Fig. 4.16 ^{1}H-^{14}N overtone HMQC NMR spectra of NAV at 11.7 T under MAS with 62.5 kHz spinning frequency, 600 scans with 128 increments in t_1 and the nitrogen pulses were set to be 50 µs. (Reprinted from Ref[132])

To achieve high resolution ^{14}N overtone NMR using the HMQC approach, a very fast spinning frequency is required as under these conditions the ^{1}H transverse relaxation time lengthens and the proton line sharpens. Nishiyama *et al.* reported that the spinning frequency has a significant effect on the overall efficiency of the HMQC experiments for ^{14}N overtone NMR (Fig. 4.17).

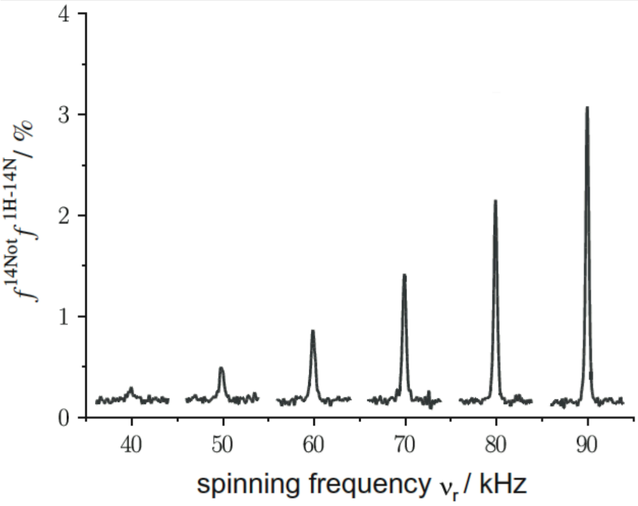

Fig. 4.17 ^{1}H HMQC filtered NMR spectra of glycine at 14.1 T under MAS with different spinning frequency, the excitation and reconversion time is 600 µs, and the nitrogen overtone pulses were set to be 200 µs. (Reprinted from Ref[131])

4.3.3.3 Sensitivity Enhancement of Nitrogen-14 Overtone Transition

Polarization enhancement is used routinely in solid state NMR to transfer magnetization from high gyromagnetic ratio nuclei to low gyromagnetic ratio nuclei. Since ^{14}N has a low gyromagnetic ratio, polarization can be transferred from a higher gyromagnetic nucleus like proton to enhance the ^{14}N overtone signal. Already in the 80s Tycko and Opella reported that the ^{14}N overtone signal for a single crystal can be enhanced using different CP pulse sequences. To overcome the difficulty of matching the Hartmann-Hahn condition, they used the Jeener-Broekaert and the Adiabatic Demagnetization in the Rotating Frame (ADRF) pulses sequence[117]. ^{14}N overtone signal enhancement were successfully achieved up to a factor of 5.9 with the ADRF sequence (Fig. 4.18C) and 3.6 with the Jeener-Broekaert sequence (Fig. 4.18B), on a model sample of single crystal NAV. Lee and Ramamoorthy in 1999 also used the Jeener-Broekaert sequence to enhance the ^{14}N signal under the static condition[139].

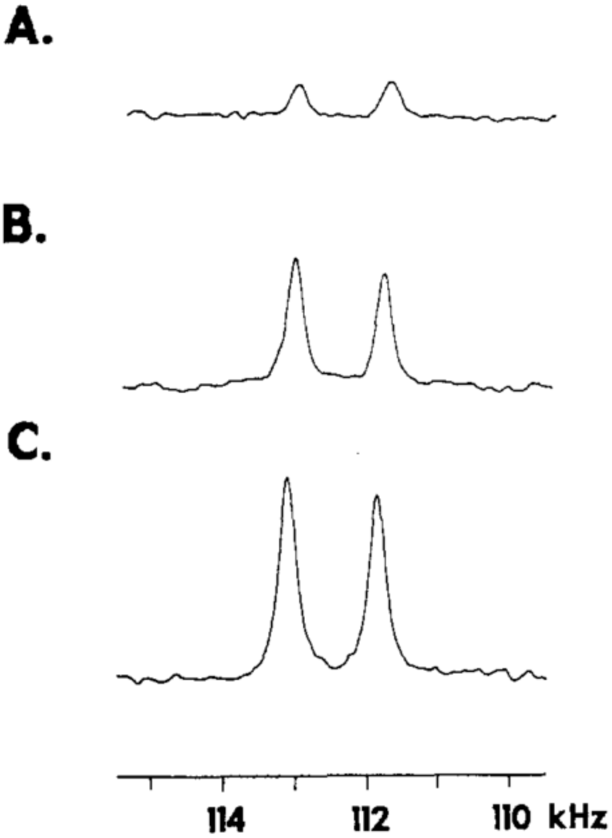

Fig. 4.18 ^{14}N overtone NMR spectra of a 60 mg single crystal of NAV acquired at 5.89 T magnetic field with 256 scans. (A) Direct excitation with 40 µs pulse length. (B) CP using Jeener-Broekaert sequence with 500 µs pulse on the overtone. (C) CP using ADRF sequence with 500 µs pulse on the overtone. (Reprinted from Ref[117])

In 2014 Rossini and co-workers reported the first ^{14}N overtone signal enhancement under MAS using ramped amplitude cross polarization Dynamic Nuclear Polarization (DNP)[133]. Signal enhancement by factor of 82 was obtained in this work for powdered glycine (Fig. 4.19). They acquired a high resolution ^{14}N overtone spectrum with 16 scans rather than thousands as in the normal case (without DNP). A long recycle delay (40 s) was used due to the long ^{1}H relaxation time at low temperature. In addition, a shorter contact time (125 μs), compared to the usual for ^{1}H-^{13}C cross polarization (1-5 ms), was found to give the optimal signal. The polarization is transferred from electron to proton using high power microwaves then to the overtone. The gyromagnetic ratio of electrons is about 660 times the gyromagnetic ratio of proton[140], thus signal enhancement by several orders of magnitude is possible. There is no evidence for significant enhancement due to the polarization transfer from proton alone, and this can be realized from Fig. 4.19B which shows that there is no signal without applying microwaves.

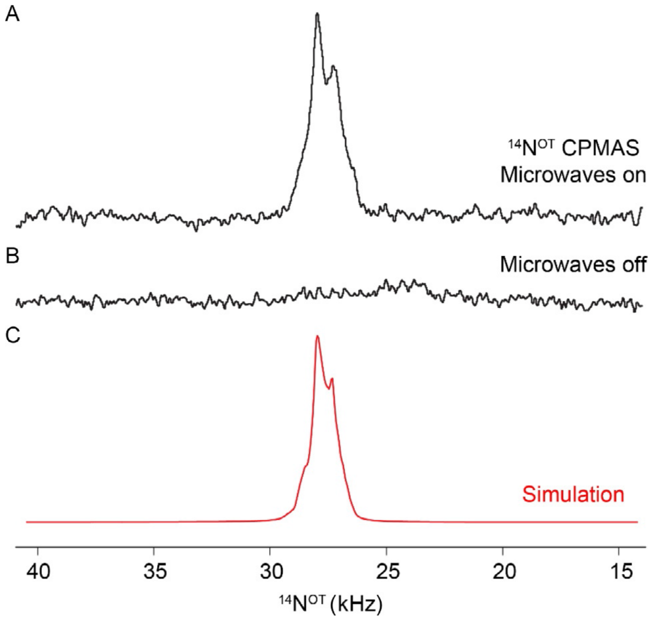

Fig. 4.19 ^{14}N overtone NMR spectra of powdered glycine acquired at 9.4 T magnetic field under MAS with 10 kHz spinning frequency. (A) DNP cross polarization spectrum acquired with 16 scans at 107 K with a 40 s recycle delay and a 125 μs CP contact pulse. (B) A spectrum acquired with the same conditions of A but without microwaves. (C) Simulated spectrum. (Reprinted from Ref[133])

^{14}N overtone signal enhancement without using microwave under MAS has been reported for the first time in 2015 (see Paper 2 for details). Enhancement by a factor of 2 has been obtained for NAV using PRESTO-II. In addition to PRESTO-II, cross polarization methods have been used to transfer magnetization to the ^{14}N overtone transition without microwaves. Enhancement by a factor up to 6.7 has been obtained for NAV(see Paper 4 for details).

Conclusions

1- ^{14}N has spin-1. Therefore, to obtain high resolution solid state NMR, different approaches from what is commonly used for half integer quadrupolar nuclei (MQMAS, STMAS) have to be developed.

2- One approach to obtain high resolution solid state NMR spectra consists in acquiring ^{14}N spectra indirectly via spy ½ spin nuclei using HMQC sequences. Different HMQC sequences have been implemented to improve this approach. Paper 1 reports a new and efficient sequence, which used long ^{14}N pulses (ms) without using excitation and reconversion intervals.

3- The second approach to obtain ^{14}N high resolution solid state NMR spectra is to exploit the ^{14}N overtone transition. Different researchers have developed further this approach during the last few years, especially after O'Dell and Ratcliffe in 2011 found that high resolution ^{14}N overtone spectra can be achieved under MAS. HMQC sequences can be implemented to obtain indirectly the ^{14}N overtone spectra. ^{14}N overtone signal can be enhanced using DNP methods. In addition, the ^{14}N overtone signal can be enhanced without using DNP through polarization transfer from protons, both with using PRESTO-II and CP (Papers 2 and 4).

   Moreover, a significant reduction of the ^{14}N overtone linewidth has been achieved using DOR for samples with moderate and large quadrupolar interaction respectively (Paper 3).

A novel simulation route for overtone transitions under MAS and DOR experiments has been implemented using the *Spinach* library under the leadership of Ilya Kuprov. This simulation approach is very fast (about 5 minutes for calculations). Simulations agree very well with experimental results with respect to the lineshape, which allow quadrupolar parameters to be accurately extracted.

Future Works

1- A new, robust and efficient HMQC sequence has been implemented using ^{13}C as spy nucleus to detect ^{14}N solid state NMR in small molecules. Therefore, to develop this sequence further using some recoupling sequences during the ^{14}N pulses and using proton nucleus as spy nucleus will be valuable targets. In addition, the application of these sequences to large scale molecules (biological samples) is also another important extension.

2- ^{14}N overtone signal enhancement has been obtained using PRESTO and CP, but with narrow excitation bandwidth. Therefore, improving the excitation bandwidth of these sequences without compromising the signal gain is important to study materials with different nitrogen sites. This can be tried using WURST pulses or other broad bandwidth pulses for exciting the ^{14}N overtone signal.

3- Second order quadrupolar line broadening can be removed from the ^{14}N overtone line using DOR, which has major disadvantages in terms of sensitivity. Therefore, removing this line broadening by manipulating the spin and space parts of the Hamiltonian on conventional probes, in analogy to MQMAS, is an important direction of research.

4- The use of optimal control theory to apply a pulse on the fundamental transition (at the Larmor frequency) and detect the signal at the overtone transition (at twice Larmor frequency) is amongst the next few experiments under planning and it is likely to bring a very significant signal enhancement if the theoretical predictions are fulfilled.

List of References

(1) Purcell, E. M.; Torrey, H. C.; Pound, R. V. *Phys. Rev.* **1946**, *69*, 37.

(2) Bloch, F. *Phys. Rev.* **1946**, *70*, 460.

(3) Levitt, M. H. *Spin Dynamics: Basics of Nuclear Magnetic Resonance*; Wiley, 2008.

(4) Sanders, J. K. M.; Hunter, B. K. *Modern NMR Spectroscopy: A Guide for Chemists*; Oxford University Press, 1993.

(5) Cavadini, S. *Prog. Nucl. Magn. Reson. Spectrosc.* **2010**, *56*, 46.

(6) Keeler, J. *Understanding NMR Spectroscopy*; John Wiley & Sons, 2010.

(7) Marinelli, L.; Wi, S.; Frydman, L. *J. Chem. Phys.* **1999**, *110*, 3100.

(8) Duer, M. J. *Introduction to Solid-State NMR Spectroscopy*; Wiley, 2002.

(9) Claramunt, R. M.; Perez-Torralba, M.; Maria, D. S.; Sanz, D.; Elena, B.; Alkorta, I.; Elguero, J. *J. Magn. Reson.* **2010**, *206*, 274.

(10) Barrow, N. S.; Yates, J. R.; Feller, S. A.; Holland, D.; Ashbrook, S. E.; Hodgkinson, P.; Brown, S. P. *Phys. Chem. Chem. Phys.* **2011**, *13*, 5778.

(11) Althaus, S. M.; Mao, K. M.; Stringer, J. A.; Kobayashi, T.; Pruski, M. *Solid State Nucl. Magn. Reson.* **2014**, *57-58*, 17.

(12) Thureau, P.; Mollica, G.; Ziarelli, F.; Viel, S. *J. Magn. Reson.* **2013**, *231*, 90.

(13) Perras, F. A.; Bryce, D. L. *J. Chem. Phys.* **2013**, *138*, 13.

(14) Gorter, C. J. *Physica* **1936**, *3*, 995.

(15) Gorter, C. J.; Broer, L. J. F. *Physica* **1942**, *9*, 591.

(16) Andrew, E. R.; Szczesniak, E. *Prog. Nucl. Magn. Reson. Spectrosc.* **1995**, *28*, 11.

(17) Andrew, E. R.; Bradbury, A.; Eades, R. G. *Nature* **1959**, *183*, 1802.

(18) Andrew, E. R.; Bradbury, A.; Eades, R. G. *Nature* **1958**, *182*, 1659.

(19) Lowe, I. J. *Phys. Rev. Lett.* **1959**, *2*, 285.

(20) Maricq, M. M.; Waugh, J. S. *J. Chem. Phys.* **1979**, *70*, 3300.

(21) Andrew, E. R. *Phil. Trans. R. Soc. A* **1981**, *299*, 505.

(22) Schaefer, J.; Stejskal, E. O.; Buchdahl, R. *J. Macromol. Sci. Phys.* **1977**, *B13*, 665.

(23) Stejskal, E. O.; Schaefer, J.; Waugh, J. S. *J. Magn. Reson.* **1977**, *28*, 105.

(24) Herzfeld, J.; Berger, A. E. *J. Chem. Phys.* **1980**, *73*, 6021.

(25) Dixon, W. T. *J. Chem. Phys.* **1982**, *77*, 1800.

(26) Filip, C.; Hafner, S.; Schnell, I.; Demco, D. E.; Spiess, H. W. *J. Chem. Phys.* **1999**, *110*, 423.

(27) Lesage, A.; Duma, L.; Sakellariou, D.; Emsley, L. *J. Am. Chem. Soc.* **2001**, *123*, 5747.

(28) Bennett, A. E.; Rienstra, C. M.; Auger, M. l.; Lakshmi, K. V.; Griffin, R. G. *J. Chem. Phys.* **1995**, *103*, 6951.

(29) Fung, B. M.; Khitrin, A. K.; Ermolaev, K. *J. Magn. Reson.* **2000**, *142*, 97.

(30) Lee, M.; Goldburg, W. *Phys. Rev.* **1965**, *140*.

(31) Waugh, J.; Huber, L.; Haeberlen, U. *Phys. Rev. Lett.* **1968**, *20*, 180.

(32) Bielecki, A.; Kolbert, A. C.; Levitt, M. H. *Chem. Phys. Lett.* **1989**, *155*, 341.

(33) Vinogradov, E.; Madhu, P. K.; Vega, S. *Chem. Phys. Lett.* **1999**, *314*, 443.

(34) Levitt, M. H. In *eMagRes*; John Wiley & Sons, Ltd: 2007.

(35) Gerstein, B. C.; Pembleton, R. G.; Wilson, R. C.; Ryan, L. M. *J. Chem. Phys.* **1977**, *66*, 361.

(36) Scheler, G.; Haubenreisser, U.; Rosenberger, H. *J. Magn. Reson.* **1981**, *44*, 134.

(37) Brown, S. P.; Spiess, H. W. *Chem. Rev.* **2001**, *101*, 4125.

(38) Schnell, I.; Spiess, H. W. *J. Magn. Reson.* **2001**, *151*, 153.

(39) Pines, A.; Gibby, M. G.; Waugh, J. S. *J. Chem. Phys.* **1973**, *59*, 569.

(40) Stejskal, E. O.; Memory, J. D. *High Resolution NMR in the Solid State: Fundamentals of CP/MAS*; Oxford University Press, 1994.

(41) Hartmann, S. R.; Hahn, E. L. *Phys. Rev.* **1962**, *128*, 2042.

(42) Peersen, O. B.; Wu, X. L.; Kustanovich, I.; Smith, S. O. *J. Magn. Reson., Ser A* **1993**, *104*, 334.

(43) Baldus, M.; Geurts, D. G.; Hediger, S.; Meier, B. H. *J. Magn. Reson., Ser A* **1996**, *118*, 140.

(44) Hediger, S.; Meier, B. H.; Ernst, R. R. *Chem. Phys. Lett.* **1995**, *240*, 449.

(45) Oas, T. G.; Griffin, R. G.; Levitt, M. H. *J. Chem. Phys.* **1988**, *89*, 692.

(46) Levitt, M. H.; Oas, T. G.; Griffin, R. G. *Isr. J. Chem.* **1988**, *28*, 271.

(47) Gullion, T.; Schaefer, J. *J. Magn. Reson.* **1989**, *81*, 196.

(48) Hing, A. W.; Vega, S.; Schaefer, J. *J. Magn. Reson.* **1992**, *96*, 205.

(49) van Rossum, B. J.; de Groot, C. P.; Ladizhansky, V.; Vega, S.; de Groot, H. J. M. *J. Am. Chem. Soc.* **2000**, *122*, 3465.

(50) Saalwachter, K.; Graf, R.; Spiess, H. W. *J. Magn. Reson.* **2001**, *148*, 398.

(51) Zhao, X.; Hoffbauer, W.; Schmedt auf der Gunne, J.; Levitt, M. H. *Solid State Nucl. Magn. Reson.* **2004**, *26*, 57.

(52) van Beek, J. D.; Dupree, R.; Levitt, M. H. *J. Chem. Phys.* **2006**, *179*, 38.

(53) Carravetta, M.; Eden, M.; Zhao, X.; Brinkmann, A.; Levitt, M. H. *Chem. Phys. Lett.* **2000**, *321*, 205.

(54) Carravetta, M.; Eden, M.; Johannessen, O. G.; Luthman, H.; Verdegem, P. J. E.; Lugtenburg, J.; Sebald, A.; Levitt, M. H. *J. Am. Chem. Soc.* **2001**, *123*, 10628.

(55) Brinkmann, A.; Eden, M.; Levitt, M. H. *J. Chem. Phys.* **2000**, *112*, 8539.

(56) Brinkmann, A.; Gunne, J.; Levitt, M. H. *J. Magn. Reson.* **2002**, *156*, 79.

(57) Brinkmann, A.; Levitt, M. H. *J. Chem. Phys.* **2001**, *115*, 357.

(58) Lee, Y. K.; Kurur, N. D.; Helmle, M.; Johannessen, O. G.; Nielsen, N. C.; Levitt, M. H. *Chem. Phys. Lett.* **1995**, *242*, 304.

(59) Debouregas, F. S.; Waugh, J. S. *J. Magn. Reson.* **1992**, *96*, 280.

(60) Smith, S. A.; Levante, T. O.; Meier, B. H.; Ernst, R. R. *J. Magn. Reson., Ser A* **1994**, *106*, 75.

(61) Bak, M.; Rasmussen, J. T.; Nielsen, N. C. *J. Chem. Phys.* **2000**, *147*, 296.

(62) Veshtort, M.; Griffin, R. G. *J. Magn. Reson.* **2006**, *178*, 248.

(63) Hogben, H. J.; Krzystyniak, M.; Charnock, G. T.; Hore, P. J.; Kuprov, I. *J. Chem. Phys.* **2011**, *208*, 179.

(64) Goldbourt, A.; Madhu, P. K. *Monatshefte fur Chemie / Chemical Monthly* **2002**, *133*, 1497.

(65) Haeberlen, U. *High Resolution NMR in Solids Selective Averaging: Supplement 1 Advances in Magnetic Resonance*; Academic Press , Inc. New York: New York, 1976.

(66) Mehring, M. *Principles of high-resolution NMR in solids*; 2 ed.; Springer-Verlag, 1983.

(67) Goldman, M.; Grandinetti, P. J.; Llor, A.; Olejniczak, Z.; Sachleben, J. R.; Zwanziger, J. W. *J. Chem. Phys.* **1992**, *97*, 8947.

(68) Wi, S.; Frydman, L. *J. Chem. Phys.* **2000**, *112*, 3248.

(69) Gan, Z. *J. Chem. Phys.* **2001**, *114*, 10845.

(70) Rose, M. E. *Elementary Theory of Angular Momentum*; Wiley: New York, 1957.

(71) Sakurai, J. J. *Advanced Quantum Mechanics*; Addison-Wesley Publishing Company, 1967.

(72) Samoson, A. *Chem. Phys. Lett.* **1985**, *119*, 29.

(73) Gan, Z. *J. Am. Chem. Soc.* **2006**, *128*, 6040.

(74) Tatton, A. S.; Pham, T. N.; Vogt, F. G.; Iuga, D.; Edwards, A. J.; Brown, S. P. *Mol. Pharm.* **2013**, *10*, 999.

(75) Samoson, A.; Lippmaa, E.; Pines, A. *Mol. Phys.* **1988**, *65*, 1013.

(76) Samoson, A.; Pines, A. *Rev. Sci. Instrum.* **1989**, *60*, 3239.

(77) Llor, A.; Virlet, J. *Chem. Phys. Lett.* **1988**, *152*, 248.

(78) Chmelka, B. F.; Mueller, K. T.; Pines, A.; Stebbins, J.; Wu, Y.; Zwanziger, J. W. *Nature* **1989**, *339*, 42.

(79) Mueller, K. T.; Sun, B. Q.; Chingas, G. C.; Zwanziger, J. W.; Terao, T.; Pines, A. *J. Magn. Reson.* **1990**, *86*, 470.

(80) Frydman, L.; Harwood, J. S. *J. Am. Chem. Soc.* **1995**, *117*, 5367.

(81) Medek, A.; Harwood, J. S.; Frydman, L. *J. Am. Chem. Soc.* **1995**, *117*, 12779.

(82) Gan, Z. H. *J. Am. Chem. Soc.* **2000**, *122*, 3242.

(83) Wu, G.; Rovnyank, D.; Sun, B. Q.; Griffin, R. G. *Chem. Phys. Lett.* **1996**, *249*, 210.

(84) Brauniger, T.; Jansen, M. *Z. Anorg. Allg. Chem.* **2013**, *639*, 857.

(85) Vega, S.; Naor, Y. *J. Chem. Phys.* **1981**, *75*, 75.

(86) Ashbrook, S. E.; Wimperis, S. *J. Chem. Phys.* **2004**, *120*, 2719.

(87) Yao, Z.; Kwak, H. T.; Sakellariou, D.; Emsley, L.; Grandinetti, P. J. *Chem. Phys. Lett.* **2000**, *327*, 85.

(88) Prasad, S.; Kwak, H. T.; Clark, T.; Grandinetti, P. J. *J. Am. Chem. Soc.* **2002**, *124*, 4964.

(89) MacKenzie, K. J. D.; Smith, M. E. *Multinuclear solid-state NMR of inorganic materials*; Pergamon, 2002.

(90) O'Dell, L. A.; Brinkmann, A. *J. Chem. Phys.* **2013**, *138*, 064201.

(91) Giavani, T.; Bildsoe, H.; Skibsted, J.; Jakobsen, H. J. *J. Magn. Reson.* **2004**, *166*, 262.

(92) Giavani, T.; Johannsen, K.; Jacobsen, C. J. H.; Blom, N.; Bildsoe, H.; Skibsted, J.; Jakobsen, H. J. *Solid State Nucl. Magn. Reson.* **2003**, *24*, 218.

(93) Giavani, T.; Bildsoe, H.; Skibsted, J.; Jakobsen, H. J. *J. Phys. Chem. B* **2002**, *106*, 3026.

(94) Haberkorn, R. A.; Stark, R. E.; Vanwilligen, H.; Griffin, R. G. *J. Am. Chem. Soc.* **1981**, *103*, 2534.

(95) Lindstrom, F.; Williamson, P. T.; Grobner, G. *J. Am. Chem. Soc.* **2005**, *127*, 6610.

(96) Stark, R. E.; Haberkorn, R. A.; Griffin, R. G. *J. Chem. Phys.* **1978**, *68*, 1996.

(97) O'Dell, L. A. *Prog. Nucl. Magn. Reson. Spectrosc.* **2011**, *59*, 295.

(98) Schurko, R. W. *Acc. Chem. Res.* **2013**, *46*, 1985.

(99) O'Dell, L. A.; Ratcliffe, C. I. *Chem. Commun.* **2010**, *46*, 6774.

(100) Harris, K. J.; Veinberg, S. L.; Mireault, C. R.; Lupulescu, A.; Frydman, L.; Schurko, R. W. *Chemistry – A European Journal* **2013**, *19*, 16469.

(101) O’Dell, L. A.; Schurko, R. W. *J. Am. Chem. Soc.* **2009**, *131*, 6658.

(102) Gan, Z. *Chem. Commun.* **2006**, 4712.

(103) Cavadini, S.; Antonijevic, S.; Lupulescu, A.; Bodenhausen, G. *J. Chem. Phys.* **2006**, *182*, 168.

(104) Cavadini, S.; Lupulescu, A.; Antonijevic, S.; Bodenhausen, G. *J. Am. Chem. Soc.* **2006**, *128*, 7706.

(105) Amoureux, J. P.; Trebosc, J.; Hu, B.; Halpern-Manners, N.; Antonijevic, S. *J. Magn. Reson.* **2008**, *194*, 317.

(106) Antonijevic, S.; Halpern-Manners, N. *Solid State Nucl. Magn. Reson.* **2008**, *33*, 82.

(107) Cavadini, S.; Abraham, A.; Bodenhausen, G. *J Magn Reson* **2008**, *190*, 160.

(108) Cavadini, S.; Antonijevic, S.; Lupulescu, A.; Bodenhausen, G. *ChemPhysChem* **2007**, *8*, 1363.

(109) Gan, Z. H. *J. Magn. Reson.* **2007**, *184*, 39.

(110) Gan, Z. H.; Amoureux, J. P.; Trebosc, J. *Chem. Phys. Lett.* **2007**, *435*, 163.

(111) Jarvis, J. A.; Haies, I. M.; Williamson, P. T. F.; Carravetta, M. *PCCP* **2013**, *15*, 7613.

(112) Nishiyama, Y.; Endo, Y.; Nemoto, T.; Utsumi, H.; Yamauchi, K.; Hioka, K.; Asakura, T. *J. Magn. Reson.* **2011**, *208*, 44.

(113) Vitzthum, V.; Borcard, F.; Jannin, S.; Morin, M.; Mieville, P.; Caporini, M. A.; Sienkiewicz, A.; Gerber-Lemaire, S.; Bodenhausen, G. *ChemPhysChem* **2011**, *12*, 2929.

(114) Cavadini, S.; Abraham, A.; Bodenhausen, G. *Chem. Phys. Lett.* **2007**, *445*, 1.

(115) Bloom, M.; LeGros, M. A. *Can. J. Phys.* **1986**, *64*, 1522.

(116) Tycko, R.; Stewart, P. L.; Opella, S. J. *J. Am. Chem. Soc.* **1986**, *108*, 5419.

(117) Tycko, R.; Opella, S. J. *J. Chem. Phys.* **1987**, *86*, 1761.

(118) Tycko, R.; Opella, S. J. *J. Am. Chem. Soc.* **1986**, *108*, 3531.

(119) O’Dell, L. A. In *Annual Reports on NMR Spectroscopy* 2015.

(120) Muller, L. *J. Electroanal. Chem.* **1979**, *101*, 363.

(121) Bodenhausen, G.; Ruben, D. J. *Chem. Phys. Lett.* **1980**, *69*, 185.

(122) Brunner, P.; Reinhold, M.; Ernst, R. R. *J. Chem. Phys* **1980**, *73*, 1086.

(123) Reinhold, M.; Brunner, P.; Ernst, R. R. *J. Chem. Phys.* **1981**, *74*, 184.

(124) Pines, A.; Ruben, D. J.; Vega, S.; Mehring, M. *Phys. Rev. Lett.* **1976**, *36*, 110.

(125) Cavadini, S.; Vitzthum, V.; Ulzega, S.; Abraham, A.; Bodenhausen, G. *J. Chem. Phys* **2010**, *202*, 57.

(126) Vitzthum, V.; Caporini, M. A.; Ulzega, S.; Bodenhausen, G. *J. Magn. Reson.* **2011**, *212*, 234.

(127) van der Waals, J. H.; de Groot, M. S. *Mol. Phys.* **1959**, *2*, 333.

(128) de Groot, M. S.; van der Waals, J. H. *Mol. Phys.* **1960**, *3*, 190.

(129) Creel, R. B.; Vonmeerwall, E. D.; Barnes, R. G. *Chem. Phys. Lett.* **1977**, *49*, 501.

(130) O'Dell, L. A.; Ratcliffe, C. I. *Chem. Phys. Lett.* **2011**, *514*, 168.

(131) Nishiyama, Y.; Malon, M.; Gan, Z.; Endo, Y.; Nemoto, T. *J. Chem. Phys.* **2013**, *230*, 160.

(132) O'Dell, L. A.; He, R. L.; Pandohee, J. *CrystEngComm* **2013**, *15*, 8657.

(133) Rossini, A. J.; Emsley, L.; O'Dell, L. A. *PCCP* **2014**, *16*, 12890.

(134) Haies, I. M.; Jarvis, J. A.; Bentley, H.; Heinmaa, I.; Kuprov, I.; Williamson, P. T.; Carravetta, M. *Phys. Chem. Chem. Phys.* **2015**, *17*, 6577.

(135) O'Dell, L. A. *Solid State Nucl. Magn. Reson.* **2013**, *55-56*, 28.

(136) Kupce, Ē.; Freeman, R. *J. Magn. Reson. Ser. A* **1995**, *117*, 246.

(137) Kupce, E.; Freeman, R. *J. Magn. Reson. Ser. A* **1995**, *112*, 134.

(138) Kupce, E.; Freeman, R. *J. Magn. Reson. Ser. A* **1995**, *115*, 273.

(139) Lee, D.-K.; Ramamoorthy, A. *Chem. Phys. Lett.* **1998**, *286*, 398.

(140) Maly, T.; Debelouchina, G. T.; Bajaj, V. S.; Hu, K. N.; Joo, C. G.; Mak-Jurkauskas, M. L.; Sirigiri, J. R.; van der Wel, P. C. A.; Herzfeld, J.; Temkin, R. J.; Griffin, R. G. *J. Chem. Phys.* **2008**, *128*, 19.

Appendices

Published and publishable papers

Appendix A : Paper I. An efficient NMR method for the characterisation of ^{14}N sites through indirect ^{13}C detection

by

Jarvis, J. A.; **Haies, I. M.**; Williamson, P. T. F.; Carravetta, M.

in

Phys. Chem. Chem. Phys. 2013, *15*, 7613.

Appendix A

PCCP

RSCPublishing

PAPER

View Article Online
View Journal | View Issue

Cite this: *Phys. Chem. Chem. Phys.*, 2013, **15**, 7613

An efficient NMR method for the characterisation of ^{14}N sites through indirect ^{13}C detection

James A. Jarvis,†[a] Ibraheem M. Haies,†[bc] Philip T. F. Williamson*[a] and Marina Carravetta*[b]

Received 21st February 2013,
Accepted 4th April 2013

DOI: 10.1039/c3cp50787d

www.rsc.org/pccp

Nitrogen is one of the most abundant elements and plays a key role in the chemistry of biological systems. Despite its widespread distribution, the study of the naturally occurring isotope of nitrogen, ^{14}N (99.6%), has been relatively limited as it is a spin-1 nucleus that typically exhibits a large quadrupolar interaction. Accordingly, most studies of nitrogen sites in biomolecules have been performed on samples enriched with ^{15}N, limiting the application of NMR to samples which can be isotopically enriched. This precludes the analysis of naturally occurring samples and results in the loss of the wealth of structural and dynamic information that the quadrupolar interaction can provide. Recently, several experimental approaches have been developed to characterize ^{14}N sites through their interaction with neighboring 'spy' nuclei. Here we describe a novel version of these experiments whereby coherence between the ^{14}N site and the spy nucleus is mediated by the application of a moderate rf field to the ^{14}N. The resulting $^{13}C/^{14}N$ spectra show good sensitivity on natural abundance and labeled materials; whilst the ^{14}N lineshapes permit the quantitative analysis of the quadrupolar interaction.

Introduction

Nitrogen is an abundant element in (bio)molecular systems playing important structural and functional roles in both proteins and nucleic acids. Accordingly, methods for the analysis of the naturally abundant isotope of nitrogen, ^{14}N, by nuclear magnetic resonance (NMR) are clearly desirable. With its high natural abundance, 99.63% and a gyromagnetic ratio 71% of the widely exploited isotope ^{15}N, ^{14}N would appear to be an attractive nucleus for investigation by NMR.

However, ^{14}N has remained largely unutilized due to the fact that it is a spin-1 nucleus that typically exhibits a moderately large quadrupolar interaction, often a few MHz in size, making its direct detection challenging. However, the presence of the large ^{14}N quadrupolar interaction can also be advantageous providing valuable information regarding the conformation and dynamics. Its accurate and efficient characterisation by NMR can potentially lead to novel insights into the structure and dynamics of (bio)molecular systems.

A number of methods have been developed to study ^{14}N by NMR. Direct detection has been employed for sites with small quadrupolar interactions[1–4] or single crystal studies.[5] For ^{14}N sites with quadrupolar interactions up to 1 MHz in size, adiabatic excitation schemes have proved effective at exciting the broad spectra.[6] However the analysis of larger quadrupolar interactions has typically relied on the "piece-wise" acquisition of a series of sub-spectra with different transmitter offsets, which are subsequently recombined to produce the overall powder pattern.[7] Such approaches have found application under static and magic-angle spinning (MAS) conditions. More recently however a class of MAS experiments has been proposed which utilizes a proximal spy nucleus, typically ^{13}C or protons, to probe the spectral properties of an adjacent ^{14}N site.[8–22]

Experiments utilizing these 'spy' nuclei approach lead to the indirect detection of the ^{14}N signal and are loosely based on the analogous liquid-state HMQC and HSQC experiments. However in this instance, coherence between the ^{14}N and the spy nuclei is mediated not only by the J-coupling but also by the second-order quadrupolar–dipolar interactions, sometimes referred to as the residual dipolar splittings, which are not completely averaged by MAS,[23] and by the dipole–dipole interaction if suitable recoupling methods are adopted.[11,14,21] These methods have enabled the spectral properties of the ^{14}N site to be determined without the need to uniformly excite or detect the ^{14}N spectrum. To date, they have proved useful in the structural and dynamic analysis of small molecules.[24,25]

---

[a] *Centre for Biological Sciences, University of Southampton, Highfield Campus, Southampton, SO17 1BJ, UK. E-mail: P.T.Williamson@soton.ac.uk*

[b] *School of Chemistry, University of Southampton, Highfield Campus, Southampton, SO17 1BJ, UK. E-mail: marina@soton.ac.uk*

[c] *College of Science, University of Mosul, Mosul, Iraq*

† These authors contributed equally to the work.

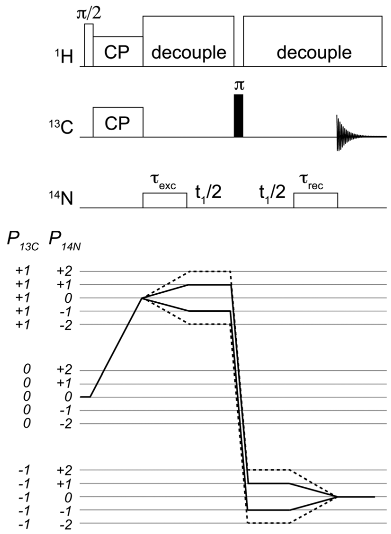

Fig. 1 Pulse sequence used for the acquisition of 2D ^{14}N/^{13}C correlation spectra. Coherence selection pathways are shown for the single quantum (solid line) and double quantum (dashed-line). Analogous 1D spectra were acquired with the same sequence with no t_1 evolution. Conditions for cross-polarization, decoupling and ^{14}N pulses are as described in the text.

Here we report on an analogous class of experiments that utilizes a proximal spy nucleus, specifically ^{13}C, to observe the spectral properties of the ^{14}N sites. Earlier methods typically generated coherence between the ^{14}N and the spy nuclei in two steps: first, the second-order quadrupolar–dipolar interactions was allowed to evolve freely during a period of mixing; then a ^{14}N pulse of duration of tens of microseconds was applied. In contrast the experiment described here generates coherence between the ^{14}N and spy nuclei under the action of a long, continuous, moderate (10's kHz) rf field applied to the ^{14}N at or close to its Larmor frequency, with no periods of free evolution (see Fig. 1). We have applied this experiment to a number of systems possessing a range of quadrupolar interactions up to about 3 MHz in size, sizes that are commonly found in organic molecules. Experimentally, by generating the ^{14}N/spy nuclei coherence under the application of a ^{14}N field, the resulting pulse sequence proves to be very robust, giving good efficiencies across a range of compounds with next to no optimization. It is well compensated for small changes in pulse duration, rf amplitude and resonance offset, making it easy to implement and apply. Indeed, experimental efficiencies are sufficient to permit the analysis of materials containing only natural abundance ^{14}N and ^{13}C in a matter of hours.

Furthermore, good agreement is observed between experimental data and numerical simulation, allowing for the accurate characterisation of the quadrupolar interaction at the ^{14}N site and providing a novel route to structural and dynamic information in small molecule, materials and biomolecular systems.

Theoretical description

The pulse sequence used in this work is shown in Fig. 1. After the initial step of ramped cross-polarization[26,27] (CP), the transverse ^{13}C magnetization evolves under the effect of the ^{13}C–^{14}N interactions during the rotor-synchronised ^{14}N pulse, of duration τ_N. During τ_N, the spin dynamics is influenced by the rf field, J-couplings, through-space dipolar couplings, quadrupole interaction and higher-second quadrupole–dipole terms.[10,19,23] The result is a complicated density operator. It has been verified by means of numerical simulations using SPINEVOLUTION[28] that both ^{14}N single quantum ($T^{N}_{1\pm1}$ and $T^{N}_{2\pm1}$) and double quantum ($T^{N}_{2\pm2}$) terms are generated with efficiencies well in excess of 20% with respect to the initial equilibrium magnetization. Hence this sequence can be effectively used to record both HSQC and HMQC-type of ^{14}N–^{13}C correlation experiments.

The pulse sequence presented for indirect ^{14}N leads to the generation of many different coherence orders, a property that is not unique to this scheme.[10,12,13,15–17] In the studies presented, the coherence order of interest has been isolated purely by means of phase cycling, as shown in Fig. 1. In this work, we demonstrate experimental results for ^{14}N SQ measurements.

Following a strong π pulse on ^{13}C, the signal is reconverted into observable ^{13}C magnetization during another ^{14}N pulse of equal duration, τ_N. Omission of the delays between the two ^{14}N pulses and the π-pulse allows the acquisition of ^{14}N-filtered ^{13}C spectra. Alternatively, an incremental delay can be inserted between the two ^{14}N pulses and the π pulse in order to allow the ^{14}N coherences to evolve, leading to the acquisition of two-dimensional (2D) spectra for indirect ^{14}N detection. The time increment in the indirect dimension must be chosen to be an integer multiple of the rotor period, *i.e.*, $\Delta t_1 = n\tau_r$, in order to ensure effective averaging of the first order quadrupolar interaction.

The π pulse has the purpose of refocusing ^{13}C isotropic and anisotropic ^{13}C chemical shifts during the ^{14}N signal evolution in the indirect dimension.

Experimental section

Materials

Natural abundance and ^{13}C labelled samples were purchased from Sigma and CIL (MA, USA) respectively and used without further purification. All samples used in this work were used as purchased without further purification. Gly-(1,2-$^{13}C_2$)Gly-Gly (>95%) was synthesized by Peptide and Protein Research using FMOC-(1,2-$^{13}C_2$)Gly purchased from CIL (MA, USA). The peptide was lyophilized and used without further purification for the studies conducted.

Numerical simulations

All 1D and 2D simulations have been performed using the SPINEVOLUTION-3.4.3 software package, whose capabilities have recently been extended to deal with quadrupolar nuclei.[28] For the sake of simplicity, the effect of protons is neglected in our simulations, which include only one ^{13}C–^{14}N spin pair. Specific details of the parameters used for each set of simulations are

Table 1 Parameters used in numerical simulations

Simulation	C_Q/ MHz	η_Q	Dipolar coupling/ kHz	Quadrupolar tensor orientation wrt dipolar tensor (α,β,γ)
Glycine (amine)[30]	1.18	0.54	−0.716	(0°,0°,0°)
Triglycine-N2 (amide)[31,32]	3.01	0.48	−0.928	(0°,90°,120°)

given in Table 1. The simulations are performed using 6044 powder points with the ZCW 3D angle sets.[29] It was verified that the simulated spectra converged under these conditions and there was no need for larger angle sets when dealing with large quadrupolar interactions (*e.g.* amide, 3.01 MHz). For the simulations, two limiting cases were considered, with quite different quadrupole size and orientations: for an NH_3 group, as found in glycine, a quadrupole interaction of 1.18 MHz, η = 0.54 aligned collinear with the dipolar interaction was employed.[30] For amide groups, as in the case of Gly-(1,2-$^{13}C_2$)Gly-Gly, we used 3.01 MHz, η = 0.48 with a relative dipole–quadrupole orientation of (0°,90°,120°), as described in Rabbani *et al.* 1987[31] and Bak *et al.* 2002.[32]

NMR experiments

Experimental data were acquired on a Bruker Avance-II spectrometer operating at 14.1 T (^{1}H, ^{13}C and ^{14}N Larmor frequencies of 600, 150 and 43.5 MHz respectively) equipped with a Bruker 2.5 mm triple resonance MAS probe modified in house to tune to ^{1}H, ^{13}C and ^{14}N. ^{13}C magnetization was generated by means of a CP using a 95 to 105% linear ramp of the proton field optimised to match a ^{13}C spin-lock field of 50 kHz. The rf amplitudes were calibrated on crystalline ammonium chloride. All ^{14}N spectra are referenced to crystalline ammonium chloride with a single resonance at 35.9 ppm.[33]

Excitation and reconversion ^{14}N pulses of equal duration were applied with a nutation frequency of 35 kHz (glycine and histidine) or 50 kHz (Gly-(1,2-$^{13}C_2$)Gly-Gly). Typically the ^{14}N pulse lengths, τ_N, were 2 ms although in each case this was optimised to give optimal efficiency and further details are given in the respective figure legends. During the ^{14}N pulses protons were decoupled using SPINAL64 decoupling with an rf amplitude of 115 kHz. Effective heteronuclear decoupling during the long ^{14}N pulses is very critical to achieve good experimental efficiency with this approach. During the t_1 and t_2 intervals, protons were decoupled using SPINAL64 with a reduced rf amplitude of 100 kHz to mitigate sample heating.[34]

^{13}C/^{14}N 2D correlation spectra were acquired phase sensitively using States acquisition.[35] Unless stated, data were processed with 30 Hz line-broadening in the t_2 prior to Fourier transform and the data zero filled to 1024 data points in each dimension. In the indirect dimension the data was acquired rotor synchronously with $\Delta t_1 = \tau_r$, until the signal had decayed to noise, typically no more than 64 t_1 increments.

Results and discussion

When compared to other methods reported in the literature, this ^{14}N excitation scheme is efficient and very easy to set-up, as the parameters vary little among different spin systems and any variations are typically minor and can to a large extent be predicted *a priori*, *i.e.*, stronger rf pulses on ^{14}N on amide groups. If all power levels are properly optimised on a model sample, like NH_4Cl, the sequence can be run on the sample of interest with minor to no optimization. These properties are highlighted in the following examples given below.

Glycine

Initial studies were performed on U-$^{13}C_2$-glycine to assess the efficiency of the experiment. Comparison of the ^{14}N/^{13}C filtered experiment conducted at 25 kHz MAS with a 2 ms ^{14}N pulse of 35 kHz rf amplitude resulted in a signal from the C_α site which was 10% of that observed from direct CP (Fig. 2). When comparison is made with the equivalent echo experiment with a 2 ms evolution period before and after the refocusing pulse, this figure increases to 17%. We attribute the improved efficiency to the unfavourable T_2 relaxation and evolution of ^{13}C–^{13}C J-couplings that occurs during the echo period which together significantly attenuates the ^{13}C signal intensity. These points are discussed in more detail below.

The corresponding 2D ^{13}C/^{14}N correlation spectrum of U-$^{13}C_2$-glycine is shown in Fig. 3 with a strong correlation observed between the amine and the C_α of the glycine. Comparison of the ^{14}N slice with that obtained by numerical simulations with literature parameters,[30] which describe the quadrupolar interaction to be 1.18 MHz with an asymmetry of η = 0.54 and aligned with the ^{13}C–^{14}N dipolar interaction, shows good agreement between them. This suggests that for smaller quadrupolar interactions, the lineshapes obtained from this experiment can be used to quantitatively characterise the quadrupolar interaction at the ^{14}N site.

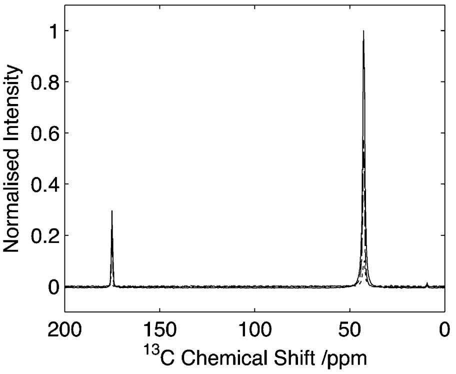

Fig. 2 Comparison of HNC efficiency on U-$^{13}C_2$-glycine. Cross polarization spectrum (solid line), echo spectrum (dashed) in comparison to optimal transfer through ^{14}N (dotted). Intensity of the C_α signal of glycine is 9% with respect to the CP signal. Data acquired with 25 kHz spinning. Data processed with 30 Hz line-broadening prior to Fourier transform.

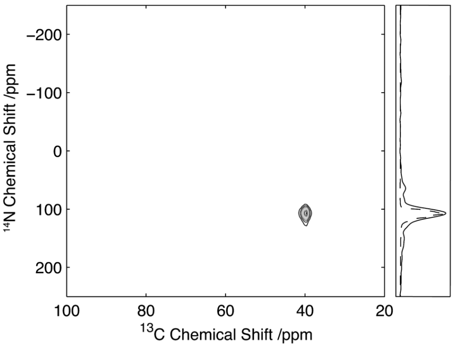

Fig. 3 ^{13}C/^{14}N 2D correlation spectrum of U-$^{13}C_2$-glycine. Data acquired with 25 kHz MAS and 2 ms, 35 kHz ^{14}N excitation and reconversion pulses. Slice through the C_α glycine peak (solid) with the corresponding simulated spectrum (dashed).

To assess the robustness of this experiment, the efficiency of transfer was measured as a function of ^{14}N pulse duration, amplitude and resonance offset on U-$^{13}C_2$-glycine. The results of these studies are shown in Fig. 4. Fig. 4A shows the build-up of the C_α intensity as a function of the ^{14}N pulse duration, τ_N, for a fixed field strength of 35 kHz with a broad maximum between 1800 μs and 2200 μs. The broad maximum observed here remained remarkably similar across all compounds reported in this manuscript, with little variation between compounds exhibiting large (∼3 MHz) and small (∼1 MHz) couplings. Experimentally, we typically observed that during the experimental setup the pulse length can be set to 2 ms, with moderate improvements (∼5%) in sensitivity being realised through subsequent experimental optimisation. Fig. 4B shows the effect of ^{14}N rf amplitude on the C_α intensity. The experimental efficiencies observed in ^{14}N filtered ^{13}C experiments conducted on U-$^{13}C_2$-glycine show a broad maximum centred at 35 kHz. Beyond this, a drop in efficiency was observed, suggesting that for quadrupolar couplings of about 1 MHz, optimal transfer between the ^{13}C and ^{14}N can be attained with currently available MAS probes. Furthermore, the weak dependency of experimental efficiency on the strength of the rf amplitude close to the optimal field makes the implementation of the experiment less challenging.

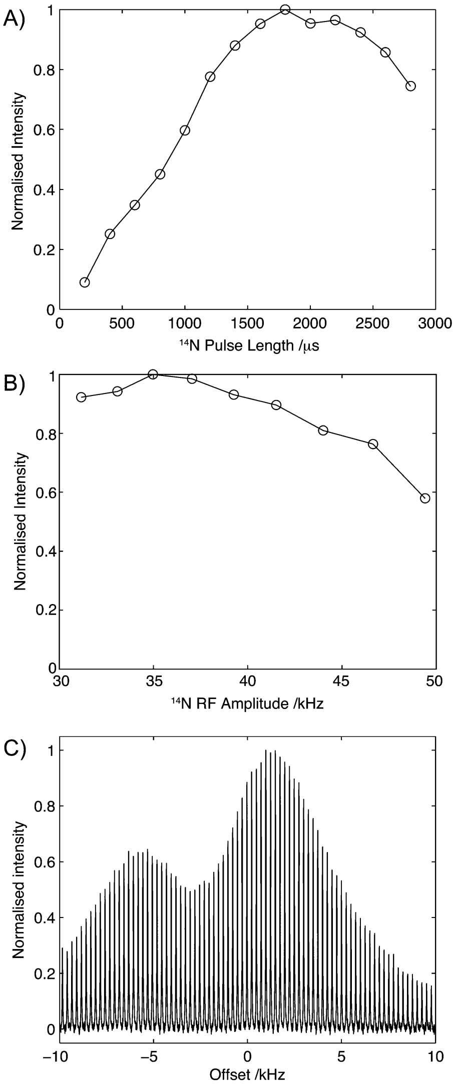

Fig. 4 Effect of pulse length (A), rf amplitude (B) and ^{14}N offset (C). In each case, the data was acquired with all other parameters optimised. In each case data normalised such that the maximum intensity is 1.0.

Due to the width of the ^{14}N spectrum, a major consideration in the implementation of these experiments is the dependence of the efficiency with respect to the ^{14}N offset. During the setup of the experiments, the initial ^{14}N offset was set to that measured for the ^{14}N signal of ammonium chloride. The efficiency of the experiment a function of the ^{14}N offset is shown in Fig. 4C and similar profiles were observed for the other compounds studied. Importantly and in contrast to direct detection, optimal efficiencies are observed close to the isotropic chemical shift values, which are frequently known from studies of other model compounds or through comparison with the respective chemical shifts observed in ^{15}N spectra.[36,37] Over the range of offsets studied here, two peaks in efficiency are observed. However, within 10 kHz (∼250 ppm) of the isotropic chemical shift of ammonium chloride, efficiencies of over 50% are recorded. The relatively high efficiencies observed across a range of frequencies which match the distribution of ^{14}N chemical shifts in most organic molecules again serves to simplify the implementation of this experiment.

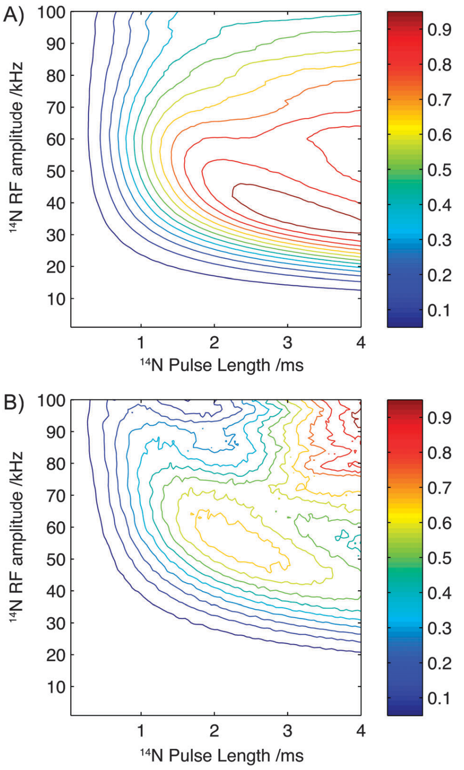

Fig. 5 Contour plots showing the simulated efficiency of the experiment as a function of pulse length and rf amplitude for parameters describing the structure and spin interactions present in glycine (A) and Gly-(1,2-^{13}C)Gly-Gly (B). Each plot is scaled such that the maximum intensity is normalised to 1.0.

To further investigate the sensitivity of the experiment to pulse length and field strength, numerical simulations have been performed with parameters which reflect the structure and spin interactions present in glycine and a single ^{13}C–^{14}N spin pair, while neglecting the presence of protons and relaxation effects. The results of these simulations are plotted in Fig. 5A. In agreement with experimental observations, optimal efficiencies are observed at experimentally accessible rf field strengths of approximately 40 kHz with efficiencies plateauing when pulse lengths exceed 2 ms.

Application to biopolymers

Results on model amino acids revealed a robust and efficient experiment, however the quadrupolar interaction typically observed in these compounds is relatively small (~1.18 MHz)[30] due to the high degree of symmetry and rotation of the amine group. Furthermore the quadrupolar interaction is typically aligned with the N–C bond which may further influence transfer efficiencies.

To ascertain the effectiveness of this experimental strategy on compounds with significantly larger quadrupolar couplings and with geometries mimicking those found in biomolecules, experiments have been conducted on Gly-(1,2-^{13}C$_2$)Gly-Gly where the labelled C^i_α and CO^i sites in residue i = 2 are found adjacent to the nitrogens at residues i = 2 and i = 3 respectively. In this tripeptide, the ^{14}N in residues i = 2 and i = 3 are contained within the peptide bond, exhibiting an sp^2 hybridization state with a lower symmetry than the amines studied previously, resulting in a quadrupolar interaction of 3.01 MHz.[31] A comparison of the ^{14}N filtered spectrum compared to the direct CP and the corresponding echo is shown in Fig. 6. For the carbonyl resonance (178.2 ppm) efficiencies of 7% are observed when compared with direct CP rising to 9% when compared to the corresponding echo experiment. In contrast, the C$_\alpha$ resonance (45.5 ppm) exhibits efficiencies of 4% when compared with the direct CP rising to 4.7% for the corresponding echo experiment. These efficiencies are comparable with efficiencies reported by other authors for indirect detection of ^{14}N in when applied to systems with similar quadrupolar interactions.[8–17,19–21]

To assess the sensitivity of the experiment to rf amplitude and ^{14}N pulse lengths when applied to polypeptides, numerical simulations were performed. In this instance, using parameters that mimic the chemical structure and spin interactions found in the backbone of a polypeptide chain, and perhaps most importantly the larger quadrupolar interaction (3.01 MHz).[31] The results of these simulations are plotted in Fig. 5B. As observed for the simulation of glycine, above 2.0 ms the efficiency shows only a weak dependency on pulse length although an optimal performance is observed between 2.0 and 2.5 ms. In contrast to the simulations calculated using parameters which represent glycine the optimal efficiency is now observed at a slightly higher ^{14}N rf amplitude, with an

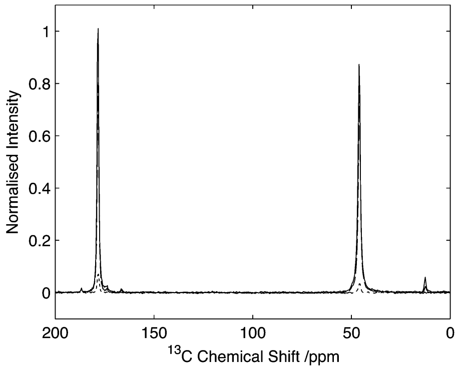

Fig. 6 Comparison of HNC efficiency on Gly-(1,2-^{13}C$_2$)Gly-Gly. Cross polarization spectrum (solid line), echo spectrum (dashed) in comparison to optimal transfer through ^{14}N (dotted). Intensity normalised with respect to maximal CP signal. Data acquired with 25 kHz spinning. Data processed with 30 Hz line-broadening prior to Fourier transform.

experimentally accessible maximum observed at fields of 50–55 kHz. Interestingly Fig. 5B highlights that for larger quadrupolar interactions, better theoretical efficiencies may be expected at higher field strength (100 kHz) and with slightly longer pulse lengths, indicating that improvements in hardware and dedicated ^{14}N probes may further enhance the efficiencies of this experiment quite significantly.

The 2D ^{14}N/^{13}C correlation spectra for Gly-(1,2-^{13}C)Gly-Gly is shown in Fig. 7. Analysis of the resonance between the CO-Gly$_2$ (178.2 ppm, ^{13}C) and the N-Gly$_3$ reveals a strong resonance centred at 420 ppm in the ^{14}N dimension with intensity spread over approximately 280 ppm (see slice in Fig. 6). In addition, a weaker resonance is observed at 120 ppm with intensity spread over approximately 100 ppm (see slice in Fig. 6). The resonance between N-Gly$_2$ and the C$_\alpha$-Gly$_2$ (45.5 ppm, ^{13}C) shows a single resonance peaking at 350 ppm with the ^{14}N with intensity spread over 165 ppm. Direct comparison of the ^{14}N slice through the carbonyl resonance with numerical simulations revealed a relatively poor agreement with the experimental data, with the simulated spectra showing a number of well-defined features that were poorly characterised in the experimental data. A better fit of the experimental data was obtained when the simulations were performed when the magic-angle deviated from 54.74° by 0.05°. This highlights the importance of setting the magic-angle accurately when the ^{14}N lineshapes are to be studied quantitatively and recently a number of protocols have been proposed which offer improvements in accuracy over utilizing the sidebands in the ^{79}Br spectra of KBr when setting the magic angle.[38,39] Despite the ^{14}N spectra being significantly broader than those observed for the equivalent amine, these spectra demonstrate that for quadrupolar couplings up to ~3.0 MHz, spectra can be acquired with reasonable efficiency with a quality sufficient to enable the characterisation of the quadrupolar interactions at the individual sites.

Application to natural abundance materials

To assess the feasibility of using this method to study samples without ^{13}C isotope enrichment that would facilitate the broader application of the experiment to unlabelled biomaterials and environmental samples spectra were acquired of natural abundance L-histidine. Spectra of L-histidine recorded with 15 kHz spinning and a 2 ms ^{14}N pulse with a field strength of 35 kHz showed excellent sensitivity compared to labelled samples with efficiencies of between 16 and 23% depending on the carbon site when compared to the direct CP. (Fig. 8). The spectrum ^{14}N/^{13}C filtered spectrum of histidine also serves to highlight the broadbanded nature of the experiment with a range of different chemistries across a range of ^{13}C resonances frequencies all showing relatively high levels of efficiencies. The efficiencies observed were sufficient to permit the acquisition of 2D data set in less than 20 h on 12 mg of material (Fig. 9). The presence of the ^{13}C spin echo means that this method will be inherently more sensitive (when compared to direct ^{13}C CP) when the T_2 of the sample is long. As demonstrated in the case of the natural abundance histidine, this serves to highlight the importance of efficient decoupling during this experiment. As postulated from our studies on U-^{13}C$_2$-Glycine, significant enhancements in efficiency are observed in this natural abundance material as the unfavourable evolution of the homonuclear ^{13}C J-couplings that would otherwise attenuate the overall echo intensity are absent. Such an observation suggests that the sensitivity of this method when applied to labelled materials would be significantly enhanced through suppression of the

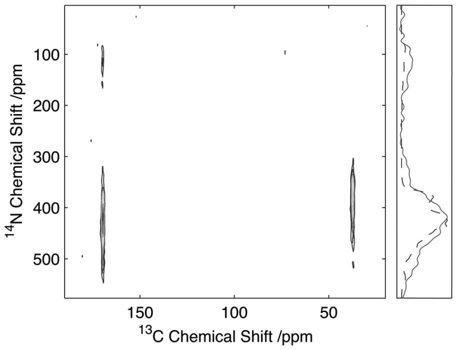

Fig. 7 ^{13}C/^{14}N 2D correlation spectrum of Gly(1,2-^{13}C$_2$-Gly)Gly. Data acquired with 25 kHz MAS and 2 ms, 35 kHz ^{14}N excitation and reconversion pulses. Slice through the CO Gly$_2$ resonance (solid) with the corresponding simulated spectrum (dashed).

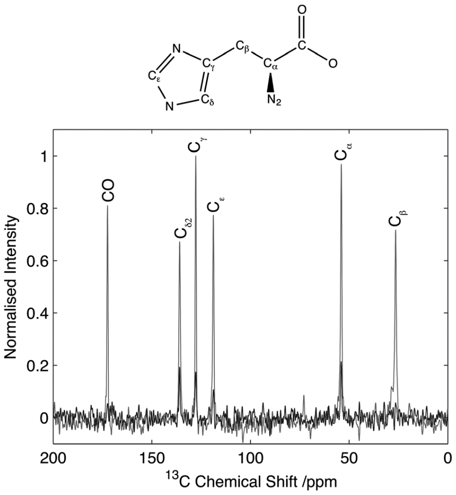

Fig. 8 Comparison of HNC efficiency on natural abundance histidine. CP spectrum (grey) in comparison to optimal transfer through ^{14}N (black). Data normalized to maximum CP intensity. Intensity of the C$_\alpha$ signal of histidine is 22% with respect to the CP signal. Data acquired with 15 kHz spinning. Data processed with 30 Hz line-broadening prior to Fourier transform.

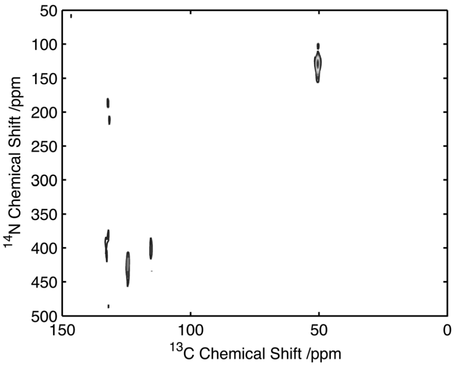

Fig. 9 ^{14}N/^{13}C correlation spectra of natural abundance histidine acquired on 12 mg of material in 20 h. Data acquired with 25 kHz MAS and 2 ms, 35 kHz ^{14}N excitation and reconversion pulses.

homo-nuclear J-couplings, with selective refocusing schemes potentially offering significant improvement for the study of backbone amide sites.[40]

Conclusion

Here we report on a novel method for studying ^{14}N sites indirectly through proximal spy nuclei. In contrast to earlier methods, transfer is mediated through extended (ms) periods of rf irradiation at moderate field strength (30–50 kHz). Experimental studies of a range of compounds supported with extensive numerical simulations have demonstrated the experiment to be robust, with little variation in efficiency across a relatively broad range of pulse lengths and rf amplitudes. Furthermore, the relatively moderate demands in rf levels and efficiencies showing only a moderate dependence on the structure and nuclear spin interactions present within the sample the experiment has proven simple to implement. Two-dimensional spectra were obtained for a range of ^{14}N sites and comparison of the simulated lineshapes shows good agreement, allowing the characterization of the ^{14}N quadrupolar interaction for all the organic compounds considered here. As highlighted above, for particular molecular systems significant improvement can be envisaged be it through the suppression of homonuclear J-couplings in labelled molecules or through the application of alternative ^{14}N excitation schemes.[22]

The ease of implementation and the good experimental efficiencies observed offer the potential to characterise the ^{14}N sites in a range of labelled and unlabelled materials providing novel routes to the characterization of their molecular structure and dynamics. These properties provide opportunities to study nitrogen in sites where before our inability to introduce isotope labels has hindered studies, areas including environmental samples, pharmaceuticals and other natural products.

Acknowledgements

NMR studies were performed at the University of Southampton's Interdisciplinary NMR Centre on equipment purchased with Wellcome Trust funding (Equipment Grant 090658/Z/09/Z and a Career Development Fellowship) to PTFW. MC thanks the Royal Society University Research Fellowship scheme for support. JJ is supported by a University of Southampton PhD studentship. We thank Ole Johannessen for experimental support.

References

1 F. Lindstrom, P. T. F. Williamson and G. Grobner, *J. Am. Chem. Soc.*, 2005, **127**, 6610–6616.
2 T. M. Rothgeb and E. Oldfield, *J. Biol. Chem.*, 1981, **256**, 6004–6009.
3 J. P. Doux, B. A. Hall and J. A. Killian, *Biophys. J.*, 2012, **103**, 1245–1253.
4 L. A. O'Dell and A. Brinkmann, *J. Chem. Phys.*, 2013, **138**, 064201.
5 R. E. Stark, R. A. Haberkorn and R. G. Griffin, *J. Chem. Phys.*, 1978, **68**, 1996–1997.
6 L. A. O'dell, R. W. Schurko, K. J. Harris, J. Autschbach and C. I. Ratcliffe, *J. Am. Chem. Soc.*, 2011, **133**, 527–546.
7 E. A. Hill and J. P. Yesinowski, *J. Am. Chem. Soc.*, 1996, **118**, 6798–6799.
8 S. Cavadini, A. Lupulescu, S. Antonijevic and G. Bodenhausen, *J. Am. Chem. Soc.*, 2006, **128**, 7706–7707.
9 S. Cavadini, S. Antonijevic, A. Lupulescu and G. Bodenhausen, *J. Magn. Reson.*, 2006, **182**, 168–172.
10 Z. H. Gan, *J. Am. Chem. Soc.*, 2006, **128**, 6040–6041.
11 Z. H. Gan, J. P. Amoureux and J. Trebosc, *Chem. Phys. Lett.*, 2007, **435**, 163–169.
12 Z. H. Gan, *J. Magn. Reson.*, 2007, **184**, 39–43.
13 S. Cavadini, S. Antonijevic, A. Lupulescu and G. Bodenhausen, *ChemPhysChem*, 2007, **8**, 1363–1374.
14 S. Cavadini, A. Abraham and G. Bodenhausen, *Chem. Phys. Lett.*, 2007, **445**, 1–5.
15 S. Cavadini, A. Abraham and G. Bodenhausen, *J. Magn. Reson.*, 2008, **190**, 160–164.
16 S. Antonijevic and N. Halpern-Manners, *Solid State Nucl. Magn. Reson.*, 2008, **33**, 82–87.
17 J.-P. Amoureux, J. Trebosc, B. Hu, N. Halpern-Manners and S. Antonijevic, *J. Magn. Reson.*, 2008, **194**, 317–320.
18 S. Ulzega, *Chimia*, 2010, **64**, 157–160.
19 S. Cavadini, *Prog. Nucl. Magn. Reson. Spectrosc.*, 2010, **56**, 46–77.
20 V. Vitzthum, F. Borcard, S. Jannin, M. Morin, P. Mieville, M. A. Caporini, A. Sienkiewicz, S. Gerber-Lemaire and G. Bodenhausen, *ChemPhysChem*, 2011, **12**, 2929–2932.
21 Y. Nishiyama, Y. Endo, T. Nemoto, H. Utsumi, K. Yamauchi, K. Hioka and T. Asakura, *J. Magn. Reson.*, 2011, **208**, 44–48.
22 V. Vitzthum, M. A. Caporini, S. Ulzega, J. Trebosc, O. Lafon, J. P. Amoureux and G. Bodenhausen, *J. Magn. Reson.*, 2012, **223**, 228–236.
23 S. Wi and L. Frydman, *J. Chem. Phys.*, 2000, **112**, 3248–3261.

24 A. S. Tatton, T. N. Pham, F. G. Vogt, D. Iuga, A. J. Edwards and S. P. Brown, *Mol. Pharmaceutics*, 2013, **10**, 999–1007.

25 K. Maruyoshi, D. Iuga, O. N. Antzutkin, A. Alhalaweh, S. P. Velaga and S. P. Brown, *Chem. Commun.*, 2012, **48**, 10844–10846.

26 S. Hediger, B. H. Meier, N. D. Kurur, G. Bodenhausen and R. R. Ernst, *Chem. Phys. Lett.*, 1994, **223**, 283–288.

27 O. B. Peersen, X. L. Wu, I. Kustanovich and S. O. Smith, *J. Magn. Reson., Ser. A*, 1993, **104**, 334–339.

28 M. Veshtort and R. G. Griffin, *J. Magn. Reson.*, 2006, **178**, 248–282.

29 V. B. Cheng, H. H. Suzukawa and M. Wolfsberg, *J. Chem. Phys.*, 1973, **59**, 3992–3999.

30 M. Strohmeier, D. W. Alderman and D. M. Grant, *J. Magn. Reson.*, 2002, **155**, 263–277.

31 S. R. Rabbani, D. T. Edmonds, P. Gosling and M. H. Palmer, *J. Magn. Reson.*, 1987, **72**, 230–237.

32 M. Bak, R. Schultz, T. Vosegaard and N. C. Nielsen, *J. Magn. Reson.*, 2002, **154**, 28–45.

33 Y. Wei, A. C. de Dios and A. E. McDermott, *J. Am. Chem. Soc.*, 1999, **121**, 10389–10394.

34 B. M. Fung, A. K. Khitrin and K. Ermolaev, *J. Magn. Reson.*, 2000, **142**, 97–101.

35 D. J. States, R. A. Haberkorn and D. J. Ruben, *J. Magn. Reson.*, 1982, **48**, 286–292.

36 R. Siegel, J. Trebosc, J. P. Amoureux and Z. Gan, *J. Magn. Reson.*, 2008, **193**, 321–325.

37 X. Song, C. M. Rienstra and A. E. McDermott, *Magn. Reson. Chem.*, 2001, **39**, S30–S36.

38 S. Antonijevic and G. Bodenhausen, *Angew. Chem.*, 2005, **44**, 2935–2938.

39 A. P. M. Kentgens, *Geoderma*, 1997, **80**, 271–306.

40 C. P. Jaroniec, B. A. Tounge, J. Herzfeld and R. G. Griffin, *J. Am. Chem. Soc.*, 2001, **123**, 3507–3519.

Appendix B : Paper II. ^{14}N overtone NMR under MAS: signal enhancement using symmetry-based sequences and novel simulation strategies

by

Haies, I. M.; Jarvis, J. A.; Bentley, H.; Heinmaa, I.; Kuprov, I.; Williamson, P.; Carravetta, M.

in

Phys. Chem. Chem. Phys. 2015, 17, 6577.

Appendix B

PCCP

PAPER

View Article Online
View Journal | View Issue

Cite this: *Phys. Chem. Chem. Phys.*, 2015, **17**, 6577

^{14}N overtone NMR under MAS: signal enhancement using symmetry-based sequences and novel simulation strategies†

Ibraheem M. Haies,[ab] James A. Jarvis,[c] Harry Bentley,[a] Ivo Heinmaa,[d] Ilya Kuprov,[a] Philip T. F. Williamson[c] and Marina Carravetta*[a]

Received 5th September 2014,
Accepted 30th January 2015

DOI: 10.1039/c4cp03994g

www.rsc.org/pccp

Overtone ^{14}N NMR spectroscopy is a promising route for the direct detection of ^{14}N signals with good spectral resolution. Its application is currently limited, however, by the absence of efficient polarization techniques for overtone signal enhancement and the lack of efficient numerical simulation techniques to aid in both the development of new methods and the analysis and interpretation of experimental data. In this paper we report a novel method for the transfer of polarization from ^{1}H to the ^{14}N overtone using symmetry-based R-sequences that overcome many of the limitations of adiabatic approaches that have worked successfully on static samples. Refinement of these sequences and the analysis of the resulting spectra have been facilitated through the development of an efficient simulation strategy for ^{14}N overtone NMR spectroscopy of spinning samples, using effective Hamiltonians on top of Floquet and Fokker–Planck equations.

Introduction

Nitrogen is a key element in both natural and synthetic systems, present in the amino acids and nucleotides that constitute the building blocks of biological systems as well as in many man-made materials such as polymers and pharmaceuticals. Accordingly, NMR methods for the analysis and characterization of the nitrogen sites within these materials are of great interest. Nitrogen has two naturally occurring NMR active isotopes: ^{15}N with nuclear spin 1/2 and a natural abundance of 0.37%, and ^{14}N with nuclear spin 1 and a natural abundance of 99.6%. The majority of nitrogen NMR studies to date have used ^{15}N because of the intrinsically sharper lines and ease of manipulation, albeit frequently at the expense of isotope labeling due to its low natural abundance. Despite its high natural abundance, ^{14}N NMR studies are frequently complicated by the large quadrupolar interaction. In contrast to half-integer spin quadrupolar nuclei, where the central transition is located close to the Larmor frequency and unaffected by the quadrupolar interaction to first order,[1,2] the single-quantum transitions of ^{14}N are frequently distributed over a MHz frequency range and distant from the Larmor frequency, complicating the detection of the NMR signal.[3–5] The large quadrupolar interactions also limit the application of magic-angle spinning, a technique designed to improve resolution and sensitivity for powder samples through the averaging of anisotropic interactions.[3] Accordingly, most ^{14}N investigations have focused on single crystal studies or nitrogen sites that exhibit a small ($<$100's kHz) quadrupolar coupling, such as those with high symmetry,[3,6–10] while for large quadrupolar interactions ($>$1 MHz) step-wise acquisition can faithfully reproduce the quadrupolar line shape.[3,11,12] In recent years, several methods for indirect detection of ^{14}N under MAS have been developed, where the ^{14}N signal is characterized indirectly through its interaction with a nearby spin-1/2 nucleus (typically ^{1}H or ^{13}C),[5,13–24] but a high-resolution method for direct detection of ^{14}N is currently lacking.

An alternative approach to ^{14}N NMR relies on the detection of the so-called overtone transition which corresponds to the change in spin projection quantum number by $\Delta m = 2$, formally a double-quantum transition, with direct detection at twice the Larmor frequency.[25] Multiple-quantum transitions are in general forbidden, but the presence of a strong quadrupolar interaction mixes Zeeman energy levels which in turn leads to a non-zero probability for the overtone transition.[26–28] Overtone transitions are insensitive to the first order quadrupolar interaction and have been observed on both static and spinning samples containing ^{14}N since the 1980's.[26–28] Both direct excitation and cross-polarization excitation schemes have been employed, the latter

---

[a] School of Chemistry, University of Southampton, SO17 1BJ, Southampton, UK. E-mail: m.carravetta@soton.ac.uk

[b] Department of Chemistry, College of Science, University of Mosul, Mosul, Iraq

[c] School of Biological Sciences, University of Southampton, SO17 1BJ, Southampton, UK

[d] National Institute of Chemical Physics and Biophysics, Akadeemia tee 23, Tallinn, 12618, Estonia

† Electronic supplementary information (ESI) available. See DOI: 10.1039/c4cp03994g

giving enhancements in sensitivity of up to a factor of 5.9 in single crystals.[27] O'Dell and co-workers demonstrated that direct excitation of ^{14}N overtone transitions with high resolution is possible under MAS,[4,29] proving that good resolution is indeed achievable in ^{14}N NMR. While direct excitation schemes are typically narrow-band, broadband excitation of the ^{14}N overtone transition has been achieved using WURST-based methods,[29] but this leads to a further loss in signal intensity. More recently, very fast MAS experiments on ^{14}N overtone demonstrated that the overtone signal can be acquired in the indirect dimension of a 2D experiment using an approach that resembles indirect detection ^{14}N NMR experiments.[30–32] Adiabatic CP methods demonstrated for static overtone excitation have not been successfully extended to rotating solids so far. The only successful report to date of ^{14}N overtone based CP methods on rotating solids is from Rossini *et al.*,[30] who used cryogenic MAS dynamic nuclear polarization (DNP) conditions, where ramped CP was applied to transfer polarization to ^{14}N overtone from hyperpolarized ^{1}H nuclei. The ^{14}N overtone signal is significant,[30] but the same experiment produced no visible signal in the absence of ^{1}H hyperpolarization.

In part the slow development of ^{14}N-overtone NMR can be attributed to the absence of efficient simulation strategies, which have been employed so successfully elsewhere for the development of solid-state NMR experiments. Simulation of the overtone transitions is demanding because: (i) there is no rotating frame that would remove all time dependence from the Hamiltonian; (ii) overtone transition moment is small, therefore all ^{14}N overtone pulses are very long and cannot be treated as ideal; (iii) the system is time-dependent at both twice the Larmor frequency and at the MAS frequency, and those frequencies are orders of magnitude away from each other; (iv) for powdered samples, three-angle spherical averaging is needed. Currently the simulations are performed by brute force in the laboratory frame and are therefore very time consuming.[4]

In this work we present a new approach based on the PRESTO (Phase-shifted Recoupling Effects a Smooth Transfer of Order), a symmetry based R-sequence, to establish ^{1}H to ^{14}N overtone correlation and achieve polarization transfer to enhance the ^{14}N overtone transition under MAS.[33–35] Complementing earlier indirect methods that employ high spinning speeds ($>$50 kHz) and high RF field ($>$250 kHz), the PRESTO sequence provides significant enhancements at moderate spinning speeds ($<$20 kHz) and moderate RF fields ($<$70 kHz), which makes it applicable to larger samples. Through the development of computationally efficient methods for the simulation of ^{14}N OT spectra we have been able to simulate the line shapes obtained under both direct excitation and PRESTO, accounting for both finite pulse effects and the polarization transfer process. The algorithm uses effective Hamiltonians on top of Floquet and Fokker–Planck equations. All methods described below are implemented into versions 1.5 and later of the Spinach library.[36]

The PRESTO approach is demonstrated on two model samples, glycine and *N*-acetyl-valine (NAV), which represent two different situations in terms of the magnitude of the quadrupolar interaction. Sensitivity increases significantly with PRESTO, with enhancements factors between 2.5 and 3.8 compared to direct excitation, when comparing the experiments by the number of acquisitions. There is no enhancement from the polarization transfer alone if the signal is measured per unit time on these samples, as the relaxation time for proton is longer than for ^{14}N (from literature). We also demonstrate the application of PRESTO technique to the acquisition of ^{1}H–^{14}N overtone correlation spectra.

Materials and methods

Sample preparation

NMR experiments were performed on glycine (identified as the alpha-glycine polymorph from X-ray diffraction) and *N*-acetyl-valine (NAV), both acquired from Sigma-Aldrich and used without further purification.

Solid state NMR equipment

NMR measurements at 14.1 T were performed using Agilent DD2 600 MHz spectrometer equipped with a 3.2 mm narrow-bore triple resonance T3 style probe and 3.2 mm zirconium oxide rotors. The resonance frequency of the ^{14}N overtone signal at this field is expected to be 86.7448 MHz. All 14.1 T spectra were referenced to this frequency.

NMR measurements at 20.0 T were performed using 850 MHz Bruker spectrometer equipped with a 3.2 mm wide-bore triple resonance probe and 3.2 mm zirconium oxide rotors. At this field the ^{14}N overtone transitions are expected to be located at 122.8331 MHz. All 20.0 T spectra were referenced to this frequency.

Solid-state NMR experiments – direct excitation and calibration

At 14.1 T, the RF power level for the ^{14}N overtone was calibrated to 55 kHz on a water sample using the ^{17}O NMR signal with a resonance frequency of 81.397 MHz. At 20.0 T, the RF power level for the ^{14}N overtone was calibrated to 70 kHz on a water sample using the ^{17}O NMR signal with a resonance frequency of 115. 262 MHz.

All experiments were performed with the RF carrier frequency in resonance with the +2 overtone spinning sideband. For direct excitation, the optimal excitation pulse width was found by taking the time of maximum signal intensity with respect to the pulse duration using direct overtone excitation under MAS with a pulse acquire sequence (shown in Fig. 1). Optimal pulse durations for direct detection were found to be 260 μs for both glycine and NAV at 14.1 T and 275 μs for glycine at 20 T.

During acquisition, 72 kHz SPINAL proton decoupling[37] was applied at 14.1 T and 89 kHz SPINAL decoupling was used for the experiments at 20.0 T. The effect of decoupling during the pulse was considered at 14.1 T and was found to be very minor for glycine, but improved significantly the excitation performance of the NAV signal. The pulse repetition delay for direct overtone excitation and spin echo were set to 0.5 s for glycine and 0.4 s for NAV (these values are compatible with previous overtone studies[4,29]). Repetition delays for PRESTO were set to 2.5 s for both glycine and NAV. Due to probe ringing near the

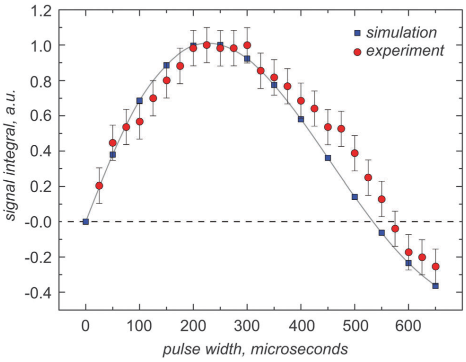

Fig. 1 Experimental data and the corresponding simulation of the nutation curve for the ^{14}N overtone signal of glycine powder, observed at its +2 spinning sideband under MAS at 9.92 kHz, using an RF pulse with a nominal RF amplitude of 55 kHz, as calibrated on the ^{17}O signal from a water sample. The simulation was performed as described in the theory section using experimental parameters for glycine from literature (Table 1), and probe geometry without any fitting or adjustment, except for the arbitrary overall scaling multiplier. The π/2 and π pulses for the ^{14}N overtone are found to be 260 μs and 520 μs, respectively.

overtone frequency, the first 70 μs of the FID were removed by applying the appropriate left shift of the experimental data points followed by phase correction for all direct excitation experiments.

Data were referenced indirectly to 0 ppm (liquid ammonia) using the ^{14}N signal of ammonium chloride at 39.3 ppm.[38] The overtone reference frequency was taken to be twice the ^{14}N reference frequency.

Solid-state NMR experiments and spin-echo

Spin echo experiments were performed at 14.1 T using the pulse sequence in Fig. 2C. Optimal pulse durations are different from the optimal pulse width obtained from direct excitation, but they are equal to the durations used in the PRESTO-II sequence. The π/2 and π ^{14}N overtone pulse lengths were set to 360 μs and 720 μs respectively for glycine, 170 μs and 340 μs respectively for NAV. The spin echo experiments used τ_1 = 0 μs and τ_2 = 10 μs for both NAV and glycine. Additional experimental data with longer τ_1 and τ_2 values are presented in the ESI.† The τ_2 delay includes the probe dead-time.

Solid-state NMR experiments and PRESTO-II

PRESTO-II sequence is described in detail elsewhere[33,34] and is used here to achieve polarization transfer between ^{1}H and the ^{14}N overtone transition using symmetry-based RN_n^ν sequences[35] that reintroduce the ^{1}H–^{14}N overtone dipolar interaction under MAS. The variants of PRESTO used in this work are summarized in Fig. 2. The basic principle behind the RN_n^ν sequences is that only selected NMR interactions can be recoupled to first order, while removing all others, by rotor-synchronizing the sequence in such a way that NR pulses (where each R pulse is a simple or composite π pulse) fit exactly in n rotor periods.

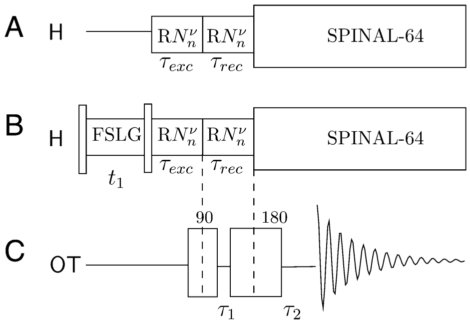

Fig. 2 (A) PRESTO-II sequence for polarization transfer from ^{1}H to ^{14}N overtone, (B) 2D PRESTO, providing ^{1}H–^{14}N overtone correlation information with homonuclear decoupling (FSLG) during t_1. The two experiments share the same ^{14}N overtone channel event sequence, which is an overtone spin-echo sequence (C).

The phase of each R pulse is determined by the third number ν in such a way that $\varphi_R = (\pi\nu)/N$ and it is alternated between $+\varphi_R$ and $-\varphi_R$. The result is an average Hamiltonian such that:

$$\bar{H}_{lm\lambda\mu} = 0 \quad \text{if} \quad mn - \mu\nu \neq Z_\lambda \frac{N}{2} \tag{1}$$

Different NMR interactions are classified in terms of their space and spin ranks, where l is the space rank of the interaction tensor, m is the space component, λ is the spin rank, μ is the spin component and Z_λ is an integer with the same parity as λ. For the $R18_2^5$ and $R18_1^7$ symmetries used here, the terms which are recoupled correspond to $\{l,m,\lambda,\mu\} = \{2,\pm2,1,\pm1\}$, that is, CSA and heteronuclear dipole–dipole interactions.[33–35] These symmetries were selected based on the practical concerns of available RF power and spinning frequencies in our probe.

The experimental optimization of PRESTO was done in stages. First, the signal intensity was optimized by direct ^{14}N overtone detection (described above), then the conditions for the spin echo were optimized. These parameters were used to set up the experiment using PRESTO-II. Then both the π/2 and π ^{14}N overtone pulse lengths were optimized again and the best pulse durations were found to be 360 μs and 720 μs respectively for glycine at 14.1 T, 375 μs and 750 μs respectively for glycine at 20.0 T, 170 μs and 340 μs respectively for NAV. Excitation and reconversion times were kept equal and the optimal duration was found to be 231 μs at 20.0 T and 201 μs at 14.1 T. Optimal spin echo pulse durations within PRESTO-II are not necessarily the same, but were found to be similar to the basic spin echo sequence.

PRESTO-II measurements were conducted using the following experimental conditions: spinning frequency $\omega_r/2\pi$ = 9.92 kHz for $R18_1^7$ (data shown only as 2D) and $\omega_r/2\pi$ = 19.84 kHz for $R18_2^5$. During PRESTO, the basic element $R = \{180_{+\varphi_R}180_{-\varphi_R}\}_0$ was employed during the excitation block, and $R = \{180_{+\varphi_R}180_{-\varphi_R}\}_{90}$ during the reconversion block.

The phase of the excitation block was cycled in two steps to remove contributions coming from direct overtone excitation, both in the experiments and in the simulations. The signal contributions from excitation through the spin echo as well as PRESTO could both be retained without this phase cycling step. For PRESTO-II, a pre-acquisition delay of 10 μs prior to detection was found to be sufficient, as for the overtone spin echo experiments.

Proton RF amplitudes of 89.2 was utilized during PRESTO. For the two-dimensional version of the PRESTO-II sequence displayed in Fig. 2B, Frequency-Switched Lee–Goldburg (FSLG) decoupling was used during the t_1 time interval to suppress the homonuclear ^{1}H couplings and improve resolution. The proton RF amplitude was set to 89.2 kHz corresponding to a LG frequency offset of 63 kHz.[39]

The narrow bandwidth of the PRESTO experiments is attributed to the overtone spin echo step in the pulse sequence, which is currently using simple sinusoidal wave ^{14}N overtone pulses.

Theoretical methods

Overtone MAS NMR is a difficult simulation target. The primary reason is the presence of two distinct large frequencies in the laboratory frame spin Hamiltonian:[40]

$$\begin{aligned}\hat{H} &= \omega_Z\hat{S}_Z + \hat{\hat{R}}(\vec{n},\omega_{\mathrm{MAS}},t)\sum_{k=-2}^{2}a_k\hat{T}_{2,k} + a_{\mathrm{RF}}\left[\hat{S}_Z\cos\theta + \hat{S}_X\sin\theta\right]\\ &\quad\times\cos[(2\omega_Z+\Delta)t] \qquad (2)\\ \hat{\hat{R}}(\vec{n},\omega_{\mathrm{MAS}},t)\hat{T}_{2,k} &= \sum_{m=-2}^{2}\hat{T}_{2,m}\mathfrak{D}^{(2)}_{mk}(\vec{n},\omega_{\mathrm{MAS}}t)\end{aligned}$$

where ω_Z is the Zeeman precession frequency, $\hat{\hat{R}}(\omega_{\mathrm{MAS}},t)$ is a spinning superoperator, $\vec{n}$ is the spinning axis, ω_{MAS} is the spinning rate in angular frequency units, $\{a_k\}$ are the five irreducible spherical components of the quadrupolar interaction tensor, $\hat{T}_{2,k}$ are the corresponding irreducible spherical tensor operators,[41] $\mathfrak{D}^{(2)}_{mk}(\vec{n},\varphi)$ are second-rank Wigner *D*-functions in angle-axis parameterization,[42,43] a_{RF} is the radiofrequency (RF) irradiation amplitude, often called the RF nutation frequency (in some conventions requiring a factor of 2 in front[34]), θ is the angle accounting for the coil orientation relative to the magnet and Δ is the offset of the RF irradiation frequency relative to the frequency of the double-quantum transition. From the computational perspective the following complications arise:

(1) There is no convenient rotating frame. The standard Zeeman rotating frame normally used in high-field MAS NMR[44,45] is ineffectual against the double-quantum frequency under the cosine. A double-quantum rotating frame would flip the sign of the Zeeman term, but not eliminate it. Laboratory frame simulations require two points per period of the fastest oscillation, meaning many millions of propagation steps per evolution second in a 14.1 T magnet, taking hours to days on modern workstations.[4]

(2) The pulses cannot be assumed to be ideal (defined as "short enough for the background Hamiltonian evolution to be negligible during the pulse") – the mixing caused by the strong quadrupolar interaction means that the transition between the outer energy levels under $\hat{S}_X$ is no longer forbidden,[46] but the transition moment for the overtone is two orders of magnitude smaller than that of the fundamental frequency. At the limit of the available hardware, the 90 degrees pulse on ^{14}N overtone is around 200 μs long. The RF pulse term in eqn (2) cannot be avoided by starting the simulation from $\hat{\rho}_0 = \hat{S}_X$ as the initial condition and a finite-duration pulse must be properly accounted for.[29]

(3) The system is spinning with a frequency typically in the range of 10–70 kHz, which is three orders of magnitude away from the frequencies of the spin evolution processes. This makes the Hamiltonian time-dependent in a numerically difficult way. At the matrix exponentiation stage, the difference between the adjacent time slices of the laboratory frame propagation problem are perilously close to the numerical accuracy limits of double-precision arithmetic.

(4) The system is a powder and a spherical average is therefore required. The lab frame simulation with millions of time steps would have to be repeated thousands of times to obtain a three-angle powder pattern.[44,45,47] Our simulations indicate that the spherical integration grid ranks required to converge an overtone powder pattern are considerably greater than those needed for the single-quantum transition signal with a comparable number of spinning sidebands.

To overcome these issues we have developed the following simulation method that avoids the time-consuming laboratory frame time propagation. Its stage are:

(1) The time dependence is eliminated from the MAS part of eqn (2) by switching it into Floquet[48] or Fokker–Planck[49] formalism (both give identical results), in which MAS is treated as a time-independent interaction between spin space and lab space degrees of freedom. In the Fokker–Planck picture[49] we get:

$$\begin{aligned}\frac{\partial}{\partial t}\hat{\rho}(\vec{x},t) &= -i\hat{\hat{H}}(\vec{x},t)\hat{\rho}(\vec{x},t) - \frac{i\omega_{\mathrm{MAS}}}{\sqrt{3}}\left[\hat{L}_X+\hat{L}_Y+\hat{L}_Z\right]\hat{\rho}(\vec{x},t)\\ \hat{\hat{H}}(\vec{x},t) &= \omega_Z\hat{S}_Z + \hat{\hat{R}}(\vec{x})\sum_{k=-2}^{2}a_k\hat{T}_{2,k} + a_{\mathrm{RF}}\left[\hat{S}_Z\cos\theta+\hat{S}_X\sin\theta\right]\\ &\quad\times\cos[(2\omega_Z+\Delta)t] \qquad (3)\end{aligned}$$

where $\hat{\hat{H}}(\vec{x},t)$ denotes a Hamiltonian commutation superoperator, $\hat{\hat{R}}(\vec{x})$ is now a time-independent rotation into the orientation specified by $\vec{x}$ and $\{\hat{L}_X, \hat{L}_Y, \hat{L}_Z\}$ are angular momentum (not spin) operators. Spherical averaging within the Fokker–Planck MAS formalism is performed automatically.[49] The Floquet picture is similar,[48] but a two-angle spherical integration grid is still required:

$$\begin{aligned}\frac{\partial}{\partial t}\hat{\rho}(\varphi,t) &= -i\hat{\hat{H}}(\varphi)\hat{\rho}(\varphi,t) + \omega_{\mathrm{MAS}}\frac{\partial}{\partial\varphi}\hat{\rho}(\varphi,t)\\ \hat{\hat{H}}(\varphi,t) &= \omega_Z\hat{S}_Z + \hat{\hat{R}}(\varphi)\sum_{k=-2}^{2}a_k\hat{T}_{2,k} + a_{\mathrm{RF}}\left[\hat{S}_Z\cos\theta+\hat{S}_X\sin\theta\right]\\ &\quad\times\cos[(2\omega_Z+\Delta)t] \qquad (4)\end{aligned}$$

where φ is the spinner phase. Both formalisms eliminate explicit time dependence from the MAS part of the problem – the time-dependent Hamiltonian problem is mapped into a time-independent Hamiltonian problem in a space of higher dimension. The increase in the matrix dimension is by a factor of $2l + 1$ (Floquet) and $(1 + l)(1 + 2l)(3 + 2l)/3$ (Fokker–Planck), where l is the cut-off rank (approximately equal to the number of spinning sidebands expected in the simulation). This dimension increase used to be a significant limitation,[50] but recent developments in sparse matrix manipulation techniques,[51] in Krylov subspace techniques[52] and particularly in tensor train methods[49,53] have removed the problem – spin Hamiltonian matrices with dimensions in the millions are now handled routinely,[53,54] although the functionality in question currently appears to be unique to *Spinach* library.[36] Floquet and Fokker–Planck methods are also preferable to time slicing from the end user perspective – both methods treat MAS as a static interaction within the Hamiltonian, thereby avoiding the complicated event scheduling[55] during pulse sequence execution and signal detection: pulse sequences programming becomes easy.

(2) The effective Hamiltonian method,[56] using matrix logarithms, is employed to remove the time dependence from the pulse part of eqn (2). The matrix logarithm technique is used because the corresponding Magnus expansion[57] does not converge even at the fourth order, due to the above mentioned lack of convenient rotating frame in overtone NMR. We could not find a way around the slow convergence of the Magnus series and the exact effective Hamiltonian expression is therefore used instead:

$$\left\langle \hat{\hat{H}}(\vec{x}) \right\rangle = \frac{i}{T} \ln\left[\exp_{(\mathrm{O})}\left(-i\int_0^T \hat{\hat{H}}(\vec{x},t)\mathrm{d}t\right)\right] \tag{5}$$

where $T = 2\pi/(2\omega_{\mathrm{Z}} + \Delta)$ is the RF period and $\exp_{(\mathrm{O})}$ denotes a time-ordered exponential. The latter is computed by slicing the RF period T and multiplying up slice propagators – sixteen slices using a second-order product integral quadrature[58] were in practice found to be sufficient. Matrix logarithm is not a straightforward operation, but numerically stable methods have recently emerged.[59] Eqn (5) eliminates the last time-dependent term without making any assumptions about the RF period or its relation to the MAS period. The Hamiltonian is now time-independent. Importantly, the total cost of getting this far is only a few dozen matrix operations.

(3) Pulses are applied using propagator squaring. The effective Hamiltonian in eqn (5) is over the RF period (about 10 nanoseconds), but the following relation:[55]

$$\begin{aligned} \exp\left[-i\hat{H}(2^n\Delta t)\right] &= \exp\left[-i\hat{H}\Delta t\right]^{2^n} \\ &= \left(\left(\exp\left[-i\hat{H}\Delta t\right]^2\right)^2\ldots\right)^2 \end{aligned} \tag{6}$$

allows to amplify this time step exponentially quickly, by squaring the propagator. A 200 μs pulse is obtained at the cost of about 17 squaring operations. The resulting propagator is then applied to the system in a single multiplication – this highlights one advantage of exponential propagation compared to linear multistep methods.[4] This final operation takes the problem to the signal detection stage, where the system evolves freely from the state $|\hat{\rho}_0\rangle$ that it has reached at the end of the pulse.

(4) The problem is moved into the frequency domain before the detection stage simulation is run. The overtone spectrum only occupies a few hundred points within a very large laboratory frame frequency range – it is therefore advantageous to replace millions of points that would be needed in the time domain with a few hundred points directly evaluated in the frequency domain. With a known initial condition and a time-independent Hamiltonian (both of which are available as a result of applying stages 1–3) the problem can be moved into the frequency domain analytically:

$$\begin{aligned} f(\omega) &= \int_0^\infty \langle \hat{S}_+ | \exp\left(-i\hat{\hat{H}}t\right) | \hat{\rho}_0 \rangle \mathrm{e}^{-i\omega t}\mathrm{d}t \\ &= \langle \hat{S}_+ | \left[\int_0^\infty \exp\left(-i\hat{\hat{H}}t\right)\mathrm{e}^{-i\omega t}\mathrm{d}t\right] | \hat{\rho}_0 \rangle \\ &= -i\langle \hat{S}_+ | \left(\hat{\hat{H}} + \omega\hat{\hat{E}}\right)^{-1} | \hat{\rho}_0 \rangle \end{aligned} \tag{7}$$

where $\hat{S}_+$ is the quadrature detection state, $\hat{\hat{E}}$ is the unit operator of the same dimension as $\hat{\hat{H}}$ and the Hamiltonian itself no longer contains the pulse term:

$$\begin{aligned} \frac{\partial}{\partial t}\hat{\rho}(\vec{x},t) &= -i\hat{\hat{H}}(\vec{x})\hat{\rho}(\vec{x},t) - \frac{i\omega_{\mathrm{MAS}}}{\sqrt{3}}\left[\hat{L}_{\mathrm{X}} + \hat{L}_{\mathrm{Y}} + \hat{L}_{\mathrm{Z}}\right]\hat{\rho}(\vec{x},t) \\ \hat{\hat{H}}(\vec{x}) &= \omega_{\mathrm{Z}}\hat{S}_{\mathrm{Z}} + \hat{\hat{R}}(\vec{x})\sum_{k=-2}^{2} a_k \hat{T}_{2,k} \end{aligned} \tag{8}$$

In practical calculations it is important to make sure that $\hat{\hat{H}}$ contains a relaxation superoperator to regularize the denominator in eqn (7) – this is the frequency domain equivalent of signal apodization. Another useful practicality is that the matrix–inverse–times–vector operation (known as *backslash*[60]) is computed directly and much faster than a matrix inverse followed by a matrix–vector multiplication. The individual frequency points also correspond to independent calculations that may be sent to different CPUs of a large parallel computer.

Nuclei other than ^{14}N are kept in their corresponding rotating frames for the entirety of the simulation. The simulation procedure described above is implemented in version 1.5 of *Spinach* library[36] available at http://spindynamics.org. Complete annotated source code for the simulations performed in this paper is included with the example set. For the systems described below, the wall clock simulation time depends on the number of spectrum digitization points as well as target accuracy, determined by Wigner *D*-function rank in the Fokker–Planck formalism[49] and spherical integration grid rank in the Floquet formalism,[48] but is generally of the order of minutes to hours.

Results and discussion

Direct excitation ^{14}N overtone experimental spectra and simulations

The ^{14}N overtone resonance position depends upon the isotropic second order quadrupolar shift and the chemical shift. Here we have optimized all experiments for the second (+2) spinning sideband, as this is the most intense sideband, which can be seen from the spectrum acquired for glycine (ESI,† Fig. S1 and previous studies[4,29]). To obtain an efficient spin echo and validate the simulation strategies employed to simulate the effects of the weak pulses on exciting the overtone transition, nutation curves for the ^{14}N overtone signal under MAS were measured at 14.1 T at a RF amplitude of 55 kHz (Fig. 1). For glycine at 9.92 kHz the agreement between experimental data and simulations is excellent, using the experimental parameters summarized in Table 1 for glycine and appropriate for the probe geometry, and demonstrate that the ^{14}N overtone finite-duration pulses are accurately simulated. The excitation pulses are significantly longer than would be predicted based on nutation curves measured on model compounds, in this case the ^{17}O signal of water, because we are dealing with a partially forbidden transition. For spin echo experiments and PRESTO, optimal pulse duration differs from the apparent 90 degree pulse and was found to be 360 μs.

For NAV, the signal we observe is very weak, possibly also because of the long dead time of 70 μs. Even though simulations suggest shorter pulses are needed for systems with large quadrupolar interaction,[32] a reliable nutation curve as in Fig. 1 was not obtained for NAV as for long pulse widths we burn a hole through the overtone line shape. The NAV signal shows a local maximum near 75 μs but after a small drop it increases again, and the ''global'' maximum signal intensity is observed close to 260 μs, and therefore this value was used for the direct excitation measurements reported here. The optimal pulse duration for echo measurements on NAV was found to be 170 μs. These cannot be related to well-defined flip angles.

The signals obtained through direct excitation of the ^{14}N overtone signal of glycine and NAV at 14.1 T and 20.0 T, as well as the corresponding simulations, are shown in Fig. 3. All measurements were performed at $\omega_r/2\pi$ = 19.84 kHz. While overtone transitions are insensitive to the first order quadrupolar interaction, lines can still be significantly broadened by higher order terms. However, it is still possible to record direct overtone spectra in a matter of minutes for glycine, which has a line width of approximately 0.83 kHz at 14.1 T (Fig. 3B). NAV is more challenging system because its larger quadrupolar interaction broadens the observed overtone signal to about 5 kHz. Combined with the long dead time of 70 μs, this results in an acquisition time of about 17 hours for the data displayed in Fig. 3A.

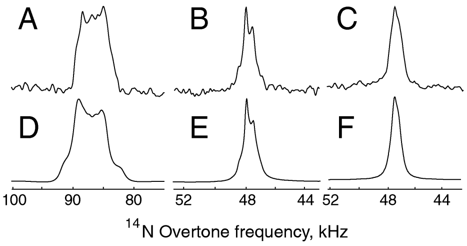

Fig. 3 ^{14}N overtone direct excitation experimental and simulated spectra obtained at the +2 spinning sideband under MAS at 19.84 kHz with a nominal RF amplitude of 55 kHz at 14.1 T and 70 kHz at 20.0 T, as calibrated on a water sample. (A) Experimental data for NAV, 160 000 scans at 14.1 T and with an excitation pulse width τ_p = 260 μs. (B) Experimental data for glycine, 1024 scans at 14.1 T with τ_p = 260 μs. (C) Experimental data for glycine, 1024 scans at 20.0 T with τ_p = 275 μs. (D, E) Simulation for NAV and glycine, respectively, at 14.1 T. (F) Simulation for glycine at 20.0 T. The simulation approach is described in the Theoretical methods section, with the input parameters summarized in Table 1, and probe geometry at the magic angle, without any fitting or adjustment, except for an arbitrary overall scaling multiplier. The simulated spectra used Lorentzian line broadening of 2000 Hz for NAV, 300 Hz for glycine.

As expected, the line shape for glycine is significantly narrower at higher magnetic field (Fig. 3C), but there is no noticeable loss in signal intensity. For all systems, the line shape and peak position can be reproduced by numerical simulations. The simulation conditions and parameters are summarized in Table 1 – the protons are kept in the direct excitation simulation to make sure that identical spin systems are being compared for the two methods. For glycine, we assume that the nitrogen–proton interaction can be replaced by a spin pair with the proton on the symmetry axis to account for the NH_3 rotation.[61,62] NAV is also more challenging from the simulation point of view, as convergence requires a large number of orientations in the spherical grid. As a consequence, typical simulation times on a contemporary workstation are up to an hour for direct excitation.

Spin echo experiments and simulations

The spin echo sequence is shown in Fig. 2(C). In conventional spin echo measurements on spin-1/2 species, the times τ_1 and

Table 1 Summary of parameters used for the simulations for glycine and NAV. The motional averaging of the NH_3 rotation is accounted for by including a single H–N dipolar interaction along the rotation axis, with an inter-nuclear distance of 1.28 Å. In both cases Floquet theory convergence is achieved at rank 5

	C_Q (MHz)	η_Q	r_{NH} (Å)	Euler angles, DD[a]	σ_{ISO} (ppm)	$\Delta\sigma$ (ppm)	η	Euler angles, CSA[a]	Lebedev grid rank
Gly[9,63]	1.18	0.53	1.28	[0, 0, 0]	32.4	—	—	—	77
NAV[64–66]	3.21	0.32	1.06	[0, 90°, 0]	121	105	0.23	[−90°, −90°, −17°]	131

[a] Dipolar and CSA interaction tensor orientations are quoted relative to the eigenframe of the ^{14}N quadrupolar interaction tensor.

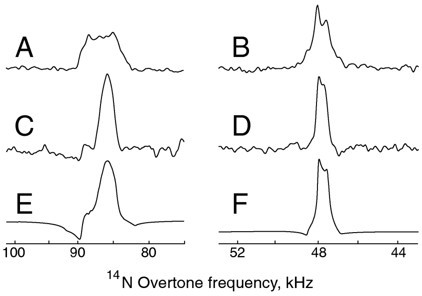

Fig. 4 Experimental direct excitation and spin-echo spectra and simulations at 14.1 T and 19.84 kHz on resonance with the +2 spinning sideband of the ^{14}N overtone signal. (A) Experimental direct excitation on NAV with 160 000 scans. (B) Experimental direct excitation on glycine with 1024 scans. (C) Experimental spin-echo data on NAV with 40 000 scans and durations of 170 μs and 340 μs for the overtone pulses, τ_1 = 0 μs and τ_2 = 10 μs for the delays. The signal enhancement is 2.0 in terms of peak height, and 0.8 in terms of peak area. (D) Experimental spin-echo spectrum on glycine, 1024 scans and durations of 360 μs and 720 μs for the overtone pulses, τ_1 = 0 μs and τ_2 = 10 μs. The signal enhancement is 1.2 in terms of peak height, and 0.8 in terms of peak area. (E and F) Numerical simulations of spin-echoes in data sets C and D, using the spin system parameters given in Table 1 and the same signal processing parameters as those used for the experimental data.

τ_2 are adjustable delays of similar duration, the 90° and 180° RF pulses provide signal excitation and inversion respectively and are typically strong enough to neglect the internal Hamiltonian during the pulse. The spin echo is an essential step within the PRESTO-II sequence for polarization transfer discussed below, but to date there has been no report of overtone spin-echo spectra. In order to achieve a spin echo on the overtone transition, some modifications of the "traditional" approach are essential, since overtone pulses are so long that there is a significant contribution from the internal Hamiltonian during the pulse (soft pulses). The pulse durations for the optimal echo do not match the durations obtained through direct optimization of the pulse lengths, and overtone pulse durations of 360–720 μs and 170–340 μs for glycine and NAV (in analogy to PRESTO). The excitation pulses are consistently longer than the expected 90 degree pulse duration for both systems.

Optimal signal intensity was achieved under unusual conditions, with no delay between the overtone pulses. Experimental data at 14.1 T and corresponding simulations were obtained for τ_1 = 0, τ_2 = 10 μs and are shown in Fig. 4, together with the corresponding simulations. Data and simulations are presented with no phase correction. More "traditional" echo experiments, with a non-zero delay between the overtone pulses, are provided in the ESI† (see Fig. S2), with only minor signal loss. Spin echo lines are visibly narrower than direct excitation, there is a small loss in integrated signal intensity, but the echo signal height increases by a factor of 1.2 and 2.0 respectively for glycine and NAV, without any need for a change in the pulse delay.

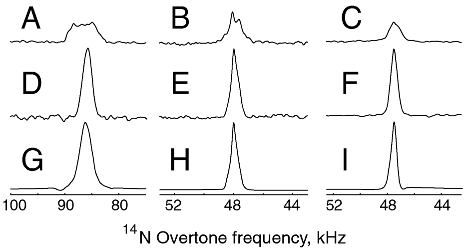

Fig. 5 Experimental direct excitation and PRESTO-II spectra and PRESTO-II simulations at 19.84 kHz on resonance with the +2 spinning sideband of the ^{14}N overtone signal. (A) Experimental direct excitation on NAV with 160 000 scans at 14.1 T (B) Experimental direct excitation on glycine with 1024 scans at 14.1 T. (C) Experimental direct excitation on glycine with 1024 scans at 20.0 T, τ_1 = 0 μs and τ_2 = 10 μs. (D) Experimental PRESTO-II data on NAV at 14.1 T with 20 000 scans and durations of 170 μs and 340 μs for the overtone pulses. The signal enhancement is 3.8 in terms of peak height, and 2.0 in terms of peak area. (E) Experimental PRESTO-II spectrum on glycine at 14.1 T with 1024 scans and durations of 360 μs and 720 μs for the overtone pulses, τ_1 = 0 μs and τ_2 = 10 μs. The signal enhancement is 2.5 in terms of peak height, and 1.5 in terms of peak area. (F) Experimental PRESTO-II spectrum on glycine at 20.0 T, 1024 scans and durations of 375 μs and 750 μs for the overtone pulses, τ_1 = 43 μs and τ_2 = 40 μs. The signal enhancement is 3.3 in terms of peak height, and 2.0 in terms of peak area. (G–I) Numerical simulations of PRESTO-II, corresponding to data sets D–F, using the spin system parameters given in Table 1 and the same signal processing parameters as those used for the experimental data.

PRESTO-II ^{14}N overtone experimental spectra and simulations

The PRESTO-II sequence has already been used to transfer polarization from high-gamma species to other spin 1/2 nuclei as well as to half-integer quadrupolar spins.[33,34] The strength of PRESTO is its simplicity when it comes to manipulation of the low-gamma spins, in this case the ^{14}N overtone. While conventional CP methods are relatively demanding on both channels, as they typically require a spin lock, PRESTO-II consists of a rather simple spin echo on the *S* channel while the complicated and demanding part of the pulse sequence is on the *I* channel.

To enhance the sensitivity of the directly detected overtone signal, PRESTO-II was applied to transfer polarization from protons. The resulting spectra for glycine and NAV are shown in Fig. 5 for the symmetry $R18_2^5$ at $\omega_r/2\pi$ = 19.84 kHz and two fields (PRESTO-II data were also obtained on glycine at 9.92 kHz and 14.1 T using $R18_1^7$, with similar performance). A comparison between the ^{14}N overtone signals as obtained through direct excitation and PRESTO-II, and the corresponding simulations are shown in Fig. 5. There is no enhancement if the signal is measured per unit time using the fully relaxed proton bath as starting condition, as the repetition delay for PRESTO-II is set to 2.5 s, significantly longer than the values used for the ^{14}N overtone measurements. In the PRESTO-II experiments reported here we focus purely on the polarization transfer step from protons in order to address strengths and limitations of this approach, hence we implemented a two-step phase cycling which removes the signal coming from direct excitation through the overtone spin echo within the PRESTO sequence. A comparison between PRESTO and spin echo data acquired with a small delay between overtone pulses at 14.1 T is given in the ESI† (Fig. S2). The directly excited spin echo overtone signal could potentially be retained and lead to a further increase of the PRESTO signal intensity and peak shape. PRESTO data acquisition can be achieved much more time-effectively by pre-saturating the ^{1}H bath and transferring polarization with just 1 s delay, while retaining about 80% of the signal (see Fig. S3 in ESI†).

When comparing experimental signal intensity for a given number of scans, the PRESTO-II experiment leads to signal enhancement by a factor of 2.5 and 3.8 for glycine and NAV respectively at 14.1 T, and by a factor of 3.3 on glycine at 20.0 T. PRESTO-II gives a narrower signal than direct excitation; hence the signal enhancement is smaller in terms of peak area, with factors of 1.5 and 2.0 respectively when compared to direct excitation on glycine and NAV at 14.1 T, and 2.0 for glycine at 20.0 T. The simulated PRESTO-II overtone peak position and line shape are in good agreement with the experimental data for both samples, and are quite sensitive to the size of the quadrupolar interaction. The signal enhancement with PRESTO is only moderately affected by an increase in magnetic field, which is encouraging for applications to more complex systems, where the added resolution and line narrowing from higher magnetic fields may be important.

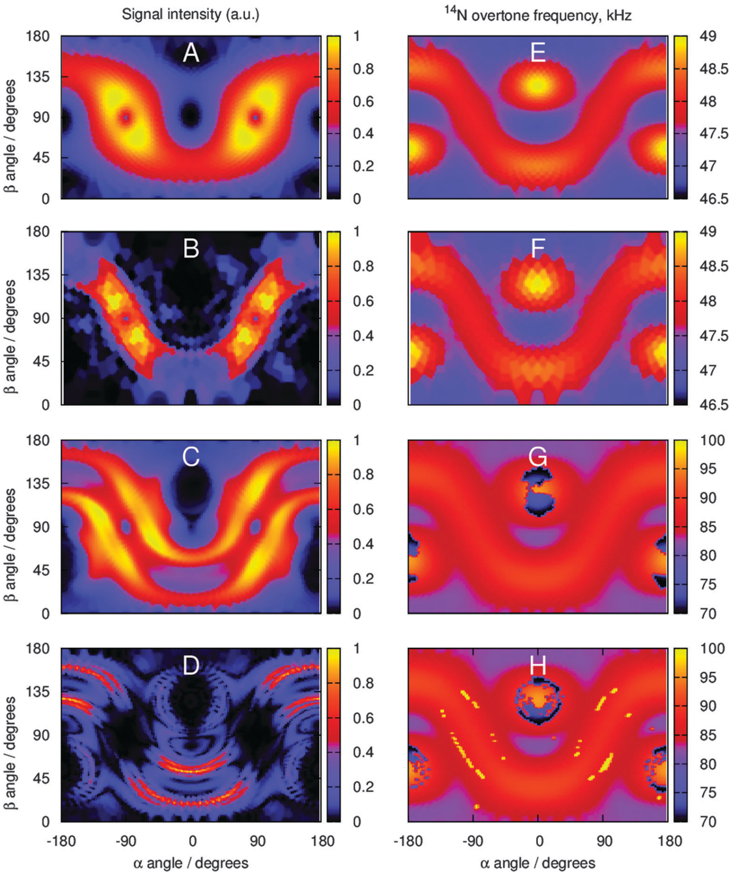

Fig. 6 Simulated signal intensity (A–D) and position (E–H) distributions with respect to $\{\alpha,\beta\}$ angles of the spherical averaging grid (two-angle Lebedev sets specified in Table 1, γ angle is averaged over by the Floquet formalism). (A) Signal intensity distribution for direct excitation on glycine. (B) Signal intensity distribution for PRESTO-II acquisition on glycine. (C) Signal intensity distribution for direct excitation on NAV. (D) Signal intensity distribution for PRESTO-II acquisition on NAV. (E) Signal position distribution for direct excitation on glycine. (F) Signal position distribution for PRESTO-II acquisition on glycine. (G) Signal position distribution for direct excitation on NAV. (H) Signal position distribution for PRESTO-II acquisition on NAV.

There have been reports of polarization transfer to the overtone transitions under MAS using ramped CP, but with unclear evidence of signal enhancement due to the ^{1}H to ^{14}N overtone transfer. Rossini and co-workers have reported significant signal enhancements using DNP,[30] but these enhancements come mainly from the hyperpolarization of the ^{1}H bath through DNP rather than the polarization transfer,[30] enhancements we expect would be mirrored when applying PRESTO. Transfer from protons is an essential step when using DNP methods and the high-gamma species allow for a more effective spread of the hyperpolarization signal, hence direct excitation of ^{14}N under those conditions would be much more unfavourable, despite its shorter relaxation time.

The experimental enhancement in the signal intensity is moderate on glycine, but is significant on NAV. This is encouraging, as it indicates the potential for applications in biological samples, because NAV is a good model system for the peptide bond. In the past, enhancement factors close to 6 have been reported for static solids, in particular for single crystals, using static adiabatic CP methods.[27] PRESTO-II achieves significant enhancement in peak heights, but with the advantages of MAS in terms of partial averaging of other anisotropic interactions. The combination of higher signal enhancement provided by polarization transfer in combination with the narrowing of the overtone transition with PRESTO-II may prove advantageous in more complex systems, but only if narrowing of the lines can be maintained while enhancing the very modest bandwidth of the current PRESTO-II sequence (see Fig. S4 in ESI†). The reduced bandwidth of PRESTO is attributed to the reduced bandwidth of the spin-echo part of the sequence, which we will address in future with the use of broadband instead of continuous-wave pulses.

This approach complements methods for indirect overtone detection *via* protons under ultra-fast MAS. PRESTO-II operates at moderate spinning frequencies and RF fields easily achievable on common 3.2 mm or 4 mm probes. On the other hand, methods based on detection *via* ^{1}H have been very successfully demonstrated on a very fast spinning probes,[31,32] but achieving optimal performance in that case requires a combination of both high RF power and high spinning speed.

Orientation dependence of direct excitation and PRESTO signals

The origin of the line narrowing observed on all samples with spin echoes and PRESTO-II has been further investigated, as it was quite surprising. Despite the same timings as for the spin echoes (Fig. 4), the PRESTO-II signals are moderately narrower. We have analyzed the position and intensity of the signals excited by each orientation of our γ-averaged (due to automatic spinner phase averaging within Floquet formalism[49]) $\{\alpha,\beta\}$ Lebedev powder grid to establish more clearly which orientations are preferentially excited by direct excitation and by PRESTO.

Simulation results using the parameters in Table 1 are shown in Fig. 6. While both direct excitation and PRESTO excite the same spectral regions, signal intensity distribution is significantly different and there are many more orientations which do not contribute much to the overall signal intensity when using PRESTO. The jagged intensity distribution pattern obtained for NAV also explains why a large number of spherical grid angles is required to achieve convergence. The narrow line shapes seen in PRESTO spectra are therefore the result of the very long overtone transition pulses only exciting a part of the full powder pattern.

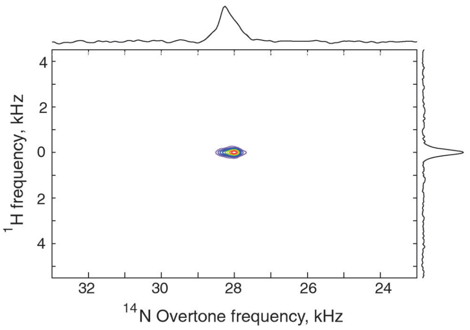

Fig. 7 ^{1}H–^{14}N overtone correlation experiment obtained with pulse sequence in Fig. 2B. The 2D data set consists of 96 t_1 increments, 48 scans per increment using the PRESTO-II sequence with symmetry $R18_1^7$ at $\omega_r/2\pi$ = 9.92 kHz.

Two-dimensional ^{1}H–^{14}N overtone correlation *via* PRESTO-II

The development of an efficient polarization transfer method at moderate spinning speeds (10–20 kHz) and RF amplitudes allows for the acquisition of multidimensional data sets that would improve signal separation in more complex systems. The PRESTO sequence described above is easily expanded to allow the acquisition of a ^{1}H–^{14}N overtone correlation spectrum under MAS, as shown in Fig. 7, and obtained with the pulse sequence sketched in Fig. 2B. The application of FSLG homonuclear decoupling during the indirect dimension results in a single correlation, between the nitrogen site and the amine protons.[27,30]

Conclusions

This work demonstrates that the ^{14}N overtone signal can be enhanced using symmetry based sequences like PRESTO-II and those polarization transfer schemes can be employed to perform correlation spectroscopy. The experimental data are consistent with numerical simulations obtained using an algorithm based on frequency-domain detection with an effective Hamiltonian treatment applied on top of Floquet or Fokker–Planck methods. The approach we describe here is faster than the brute-force lab frame simulation; it will help in both the development of improved experimental techniques and in the interpretation of the resulting spectra.

A number of ways are known to enhance the sensitivity of ^{14}N overtone detection – both fast MAS and very strong RF fields have been demonstrated to be beneficial for the efficient excitation of the overtone transition.[31,32] Here we have investigated an alternative approach to ^{14}N overtone signal enhancement that relies on the efficient transfer of polarization from the abundant protons to the ^{14}N overtone using the PRESTO-II sequence. We found this method to be effective with moderate RF fields and MAS spinning frequencies. This work also demonstrates alternative methods for obtaining multidimensional correlation experiments involving ^{14}N overtone and describes the computational tools required to continue their development.

Acknowledgements

This research was supported by the Wellcome Trust (PTFW and MC), EPSRC (EP/H003789/1, IK) and by the Royal Society University Research Fellowship (MC). Ibraheem Haies thanks The Higher Committee for Education Development in Iraq for financial support. We are grateful to Vadim Zorin (Agilent) and Aaron Rossini for helpful discussions. With thank Richard Bounds for the XRD measurements on glycine. The UK 850 MHz solid-state NMR Facility instruments used in this research were funded by EPSRC and BBSRC, as well as the University of Warwick, including *via* part funding through Birmingham Science City Advanced Materials Projects 1 and 2 supported by Advantage West Midlands (AWM) and the European Regional Development Fund (ERDF). Ivo Heinmaa was supported by Estonian Research Council through grant IUT23-3.

References

1 A. Goldbourt and P. K. Madhu, *Monatsh. Chem.*, 2002, **133**, 1497.
2 Z. H. Gan, *J. Chem. Phys.*, 2001, **114**, 10845.
3 K. J. D. MacKenzie and M. E. Smith, *Multinuclear solid-state NMR of inorganic materials*, Pergamon, 2002.
4 L. A. O'Dell and A. Brinkmann, *J. Chem. Phys.*, 2013, **138**, 064201.
5 S. Cavadini, *Prog. Nucl. Magn. Reson. Spectrosc.*, 2010, **56**, 46.
6 M. J. Duer, *Solid-state NMR Spectroscopy Principles and Applications*, Blackwell Science Ltd, Oxford, 2002.
7 T. Giavani, K. Johannsen, C. J. H. Jacobsen, N. Blom, H. Bildsoe, J. Skibsted and H. J. Jakobsen, *Solid State Nucl. Magn. Reson.*, 2003, **24**, 218.
8 T. Giavani, H. Bildsoe, J. Skibsted and H. J. Jakobsen, *J. Phys. Chem. B*, 2002, **106**, 3026.
9 R. A. Haberkorn, R. E. Stark, H. Vanwilligen and R. G. Griffin, *J. Am. Chem. Soc.*, 1981, **103**, 2534.
10 F. Lindstrom, P. T. F. Williamson and G. Grobner, *J. Am. Chem. Soc.*, 2005, **127**, 6610.
11 K. J. Harris, S. L. Veinberg, C. R. Mireault, A. Lupulescu, L. Frydman and R. W. Schurko, *Chem. – Eur. J.*, 2013, **19**, 16469.
12 L. A. O'Dell and R. W. Schurko, *J. Am. Chem. Soc.*, 2009, **131**, 6658.
13 J. P. Amoureux, J. Trebosc, B. Hu, N. Halpern-Manners and S. Antonijevic, *J. Magn. Reson.*, 2008, **194**, 317.
14 S. Antonijevic and N. Halpern-Manners, *Solid State Nucl. Magn. Reson.*, 2008, **33**, 82.
15 S. Cavadini, A. Abraham and G. Bodenhausen, *J. Magn. Reson.*, 2008, **190**, 160.
16 S. Cavadini, S. Antonijevic, A. Lupulescu and G. Bodenhausen, *J. Magn. Reson.*, 2006, **182**, 168.
17 S. Cavadini, S. Antonijevic, A. Lupulescu and G. Bodenhausen, *ChemPhysChem*, 2007, **8**, 1363.
18 S. Cavadini, A. Lupulescu, S. Antonijevic and G. Bodenhausen, *J. Am. Chem. Soc.*, 2006, **128**, 7706.
19 Z. H. Gan, *J. Magn. Reson.*, 2007, **184**, 39.
20 Z. H. Gan, J. P. Amoureux and J. Trebosc, *Chem. Phys. Lett.*, 2007, **435**, 163.
21 J. A. Jarvis, I. M. Haies, P. T. F. Williamson and M. Carravetta, *Phys. Chem. Chem. Phys.*, 2013, **15**, 7613.
22 Y. Nishiyama, Y. Endo, T. Nemoto, H. Utsumi, K. Yamauchi, K. Hioka and T. Asakura, *J. Magn. Reson.*, 2011, **208**, 44.
23 V. Vitzthum, F. Borcard, S. Jannin, M. Morin, P. Mieville, M. A. Caporini, A. Sienkiewicz, S. Gerber-Lemaire and G. Bodenhausen, *ChemPhysChem*, 2011, **12**, 2929.
24 Z. H. Gan, *J. Am. Chem. Soc.*, 2006, **128**, 6040.
25 M. Bloom and M. A. LeGros, *Can. J. Phys.*, 1986, **64**, 1522.
26 R. Tycko, P. L. Stewart and S. J. Opella, *J. Am. Chem. Soc.*, 1986, **108**, 5419.
27 R. Tycko and S. J. Opella, *J. Chem. Phys.*, 1987, **86**, 1761.
28 R. Tycko and S. J. Opella, *J. Am. Chem. Soc.*, 1986, **108**, 3531.
29 L. A. O'Dell and C. I. Ratcliffe, *Chem. Phys. Lett.*, 2011, **514**, 168.
30 A. J. Rossini, L. Emsley and L. A. O'Dell, *Phys. Chem. Chem. Phys.*, 2014, **16**, 12890.
31 Y. Nishiyama, M. Malon, Z. H. Gan, Y. Endo and T. Nemoto, *J. Magn. Reson.*, 2013, **230**, 160.
32 L. A. O'Dell, R. He and J. Pandohee, *CrystEngComm*, 2013, **15**, 8657.
33 X. Zhao, W. Hoffbauer, J. S. A. D. Gunne and M. H. Levitt, *Solid State Nucl. Magn. Reson.*, 2004, **26**, 57.
34 J. D. van Beek, R. Dupree and M. H. Levitt, *J. Magn. Reson.*, 2006, **179**, 38.
35 M. H. Levitt, D. M. Grant and K. J. Harris, *Encyclopedia of Magnetic Resonance*, John Wiley and Sons, 2007, vol. 9.
36 H. J. Hogben, M. Krzystyniak, G. T. P. Charnock, P. J. Hore and I. Kuprov, *J. Magn. Reson.*, 2011, **208**, 179.
37 B. M. Fung, A. K. Khitrin and K. Ermolaev, *J. Magn. Reson.*, 2000, **142**, 97.
38 P. Bertani, J. Raya and B. Bechinger, *Solid State Nucl. Magn. Reson.*, 2014, **61–62**, 15.
39 A. Bielecki, A. C. Kolbert and M. H. Levitt, *Chem. Phys. Lett.*, 1989, **155**, 341.
40 L. Marinelli, S. Wi and L. Frydman, *J. Chem. Phys.*, 1999, **110**, 3100.
41 P. P. Man, *Concepts Magn. Reson., Part A*, 2013, **42**, 197.
42 M. Siemens, J. Hancock and D. Siminovitch, *Solid State Nucl. Magn. Reson.*, 2007, **31**, 35.
43 D. A. Varshalovich, A. N. Moskalev and V. K. Khersonskiī, *Quantum theory of angular momentum: irreducible tensors, spherical harmonics, vector coupling coefficients, 3nj symbols*, World Scientific, 1988.
44 M. Edén, *Concepts Magn. Reson., Part A*, 2003, **17A**, 117.
45 P. Hodgkinson and L. Emsley, *Prog. Nucl. Magn. Reson. Spectrosc.*, 2000, **36**, 201.

46 S. E. Ashbrook, J. McManus, M. J. Thrippleton and S. Wimperis, *Prog. Nucl. Magn. Reson. Spectrosc.*, 2009, **55**, 160.

47 M. Bak, J. T. Rasmussen and N. C. Nielsen, *J. Magn. Reson.*, 2000, **147**, 296.

48 M. Leskes, P. K. Madhu and S. Vega, *Prog. Nucl. Magn. Reson. Spectrosc.*, 2010, **57**, 345.

49 L. J. Edwards, D. V. Savostyanov, A. A. Nevzorov, M. Concistre, G. Pileio and I. Kuprov, *J. Magn. Reson.*, 2013, **235**, 121.

50 S. A. Smith, T. O. Levante, B. H. Meier and R. R. Ernst, *J. Magn. Reson., Ser. A*, 1994, **106**, 75.

51 U. Schendel, *Sparse matrices: numerical aspects with applications for scientists and engineers*, Halsted Press, 1989.

52 I. Kuprov, *J. Magn. Reson.*, 2008, **195**, 45.

53 D. V. Savostyanov, S. V. Dolgov, J. M. Werner and I. Kuprov, *Phys. Rev. B: Condens. Matter Mater. Phys.*, 2014, **90**, 085139.

54 L. J. Edwards, D. V. Savostyanov, Z. T. Welderufael, D. H. Lee and I. Kuprov, *J. Magn. Reson.*, 2014, **243**, 107.

55 W. B. Blanton, J. W. Logan and A. Pines, *J. Magn. Reson.*, 2004, **166**, 174.

56 M. Edén, Y. K. Lee and M. H. Levitt, *J. Magn. Reson., Ser. A*, 1996, **120**, 56.

57 J. S. Waugh, *eMagRes*, Wiley, 2007, vol. 1, p. 179.

58 J. D. Dollard and C. N. Friedman, *J. Math. Phys.*, 1977, **18**, 1598.

59 N. J. Higham, *Functions of Matrices: Theory and Computation*, SIAM, 2008.

60 I. S. Duff and J. K. Reid, *ACM Trans. Math. Software*, 1983, **9**, 302.

61 M. Veshtort and R. G. Griffin, *J. Chem. Phys.*, 2011, **135**, 134509.

62 C. H. Wu, B. B. Das and S. J. Opella, *J. Magn. Reson.*, 2010, **202**, 127.

63 R. E. Taylor and C. Dybowski, *J. Mol. Struct.*, 2008, **889**, 376.

64 R. E. Stark, R. A. Haberkorn and R. G. Griffin, *J. Chem. Phys.*, 1978, **68**, 1996.

65 E. Salnikov, P. Bertani, J. Raap and B. Bechinger, *J. Biomol. NMR*, 2009, **45**, 373.

66 M. Bak, R. Schultz, T. Vosegaard and N. C. Nielsen, *J. Magn. Reson.*, 2002, **154**, 28.

Appendix C : Supporting information for Paper II. Supporting information for “^{14}N Overtone NMR under MAS: signal enhancement using symmetry-based sequences and novel simulation strategies ”

by

Haies, I. M.; Jarvis, J. A.; Bentley, H.; Heinmaa, I.; Kuprov, I.; Williamson, P.; Carravetta, M.

in

Phys. Chem. Chem. Phys. 2015, 17, 6577.

Electronic Supplementary Material (ESI) for Physical Chemistry Chemical Physics.

Supporting information for

"^{14}N Overtone NMR under MAS: signal enhancement using symmetry-based sequences and novel simulation strategies "

Ibraheem Haies[a,b], James A. Jarvis[c], Harry Bentley[a], Ivo Heinmaa[d],
Ilya Kuprov[a], Philip T.F. Williamson[c], Marina Carravetta[a]*.

[a] *School of Chemistry, University of Southampton,*
SO17 1BJ, Southampton, United Kingdom.

[b]*Department of Chemistry, College of Science,*
University of Mosul, Mosul, Iraq.

[c] *School of Biological Sciences, University of Southampton,*
SO17 1BJ, Southampton, United Kingdom.

[d] *National Institute of Chemical Physics and Biophysics*
Akadeemia tee 23, Tallinn, 12618, Estonia.

(Dated: 11 September 2014)

FIGURE S1:

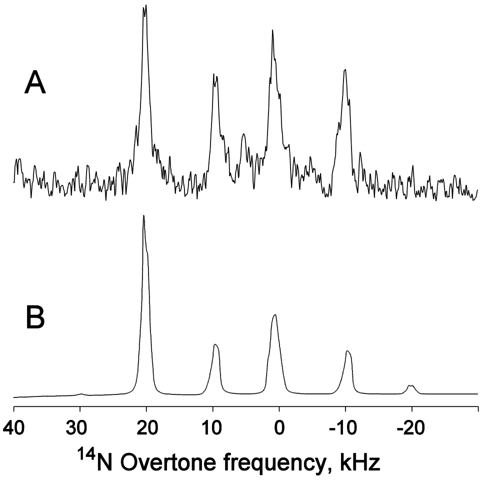

Fig. S1. (A) Experimental overtone sidebands, acquired with the RF carrier set on resonance with the central overtone transition, at $\omega_r/2\pi$ = 9.92 kHz, using 450000 scans and a pulse width of 50 µs. The first 109 µs from the end of the RF pulse were removed (dead-time and left-shift) before the FID was Fourier transformed. The resulting spectra are reported in magnitude mode. (B) Simulation, using the formalism described in the main text with GSQ rank 29 and Floquet rank 10, of the same experiment using experimental probe geometry and pulse amplitudes.

The sideband spectrum was acquired on resonance for the overtone center band. As can be seen from the above spectra, the intensity of the full sideband family is much weaker (data acquired with 450,000 scans, with 38 mg of glycine in a 3.2 mm thin walled rotor) than the detection of the single sideband (see main manuscript). The removal of the first 100 µs of signal acquisition due to severe ringing was also reported by O'Dell and Brinkmann. This large time gap causes significant phase distortions, and thus data is presented in magnitude mode and compared with simulations processed in an identical fashion. The experimental data in Fig. S1A and simulations in Fig. S1B show that the $\pm\omega_r$ spinning sidebands, $+2\omega_r$spinning sideband, and the center band peaks can be clearly detected. The $-2\omega_r$ spinning sideband is expected to be very weak and did not appear at these conditions. The $+2\omega_r$ spinning sideband is the most intense peak and used in all studies within the paper.

FIGURE S2:

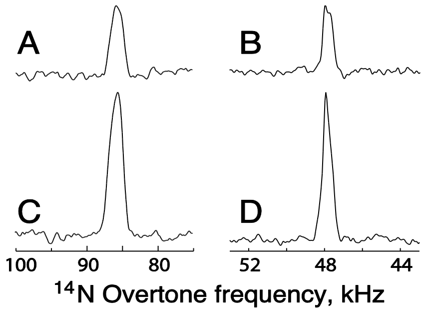

Fig. S2. Experimental comparison between spin-echo and PRESTO-II data at 14.1 T and a spinning frequency of 19.84 kHz on resonance with the +2 spinning sideband of the ^{14}N overtone signal. (A) Spin echo on NAV, 40000 scans with $\tau_1 = 116.6$ μs, $\tau_2 = 116.4$ μs, overtone pulses of 170 and 340 μs. The signal height is 1.9 times larger than direct excitation and the integrated signal intensity changes by a factor of 0.8. (B) Spin echo on glycine, 1024 scans with $\tau_1 = 21.6$ μs, $\tau_2 = 20.0$ μs, overtone pulses of 360 and 720. The signal height is 1.2 times larger than direct excitation and the integrated signal intensity changes by a factor of 0.8. (C) PRESTO-II on NAV, 20000 scans with $\tau_1 = 116.6$ μs, $\tau_2 = 116.4$ μs, overtone pulses of 170 and 340. The signal height is 3.7 times larger than direct excitation and the integrated signal intensity increases by a factor of 1.9. (D) PRESTO-II on glycine, 1024 scans with $\tau_1 = 21.6$ μs, $\tau_2 = 20.0$ μs, overtone pulses of 360 and 720 μs and 2.5 s repetition delay. The signal height is 2.4 times larger than direct excitation and the integrated signal intensity increases by a factor of 1.4.

Besides the case of no delay between overtone pulses, we also provide a more conventional example of overtone spin echo, with a delay between pulses in the range of tens to hundreds of microseconds. The timings were chosen in such a way to be compatible with a PRESTO-II sequence where the second overtone pulse starts exactly at the end of the PRESTO reconversion block. As can be seen, the PRESTO spectra are only moderately narrower than the corresponding spin echo spectra under these conditions. Efficiencies are nearly identical to what reported in the main paper both for PRESTO and for the echo.

FIGURE S3:

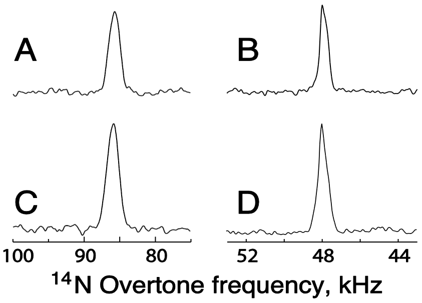

Fig. S3. Experimental comparison between PRESTO-II data at 14.1 T and 19.84 kHz on resonance with the +2 spinning sideband of the ^{14}N overtone signal, acquired using with $\tau_1 = 0$ µs, $\tau_2 = 10.$ µs acquired with different repetition delays. (A) NAV, 20000 scans with overtone pulses of 170 and 340 µs and 1 s repetition delay. The signal height is 2.4 times larger than direct excitation and the integrated signal intensity increases by a factor of 1.5. (B) Glycine, 1024 scans overtone pulses of 360 and 720 and 1 s repetition delay. The signal height is 2.0 times larger than direct excitation and the integrated signal intensity increases by a factor of 1.2. (C) NAV, 20000 scans with overtone pulses of 170 and 340 with 2.5 s pulse delay. (D) Glycine, 1024 scans with overtone pulses of 360 and 720 µs and 2.5 s repetition delay.

Time-effective PRESTO-data acquisition is possible if we reduce the pulse delay from 2.5 s used in the key paper to show the maximum enhancement from a fully relaxed ^{1}H signal, to only 1 s. This leads to a PRESTO-II sequence in which the signal per unit time is about equal of slightly larger than the signal with direct excitation.

FIGURE S4:

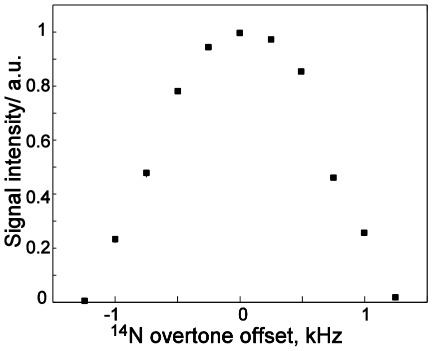

Fig. S4. Experimental PRESTO-II signal intensity for glycine at 14,1 T, 19.84 kHz spinning frequency, 1024 with 55 kHz RF power on the overtone transition as a function of the offset in the ^{14}N overtone field. There is a very strong offset dependence and the overall bandwidth is about 1 kHz.

Appendix D : Paper III. ^{14}N overtone transition in double rotation solid-state NMR

by

Haies, I. M.; Jarvis, J. A.; Brown, L. J.; Kuprov, I.; Williamson, P.; Carravetta, M.

in

Accepted in *Phys. Chem. Chem. Phys.* 2015.

Appendix D

PCCP

PAPER

View Article Online
View Journal

Cite this: DOI: 10.1039/c5cp03266k

^{14}N overtone transition in double rotation solid-state NMR†

Ibraheem M. Haies,[ab] James A. Jarvis,[c] Lynda J. Brown,[a] Ilya Kuprov,[a]
Philip T. F. Williamson[c] and Marina Carravetta*[a]

Solid-state NMR transitions involving outer energy levels of the spin-1 ^{14}N nucleus are immune, to first order in perturbation theory, to the broadening caused by the nuclear quadrupole interaction. The corresponding overtone spectra, when acquired in conjunction with magic-angle sample spinning, result in lines, which are just a few kHz wide, permitting the direct detection of nitrogen compounds without the need for labeling. Despite the success of this technique, "overtone" resonances are still broadened due to indirect, second order effects arising from the large quadrupolar interaction. Here we demonstrate that another order of magnitude in spectral resolution may be gained by using double rotation. This brings the width of the ^{14}N solid-state NMR lines much closer to the region commonly associated with high-resolution solid-state NMR spectroscopy of ^{15}N and demonstrates the improvements in resolution that may be possible through the development of pulsed methodologies to suppress these second order effects.

Received 5th June 2015,
Accepted 4th August 2015

DOI: 10.1039/c5cp03266k

www.rsc.org/pccp

Introduction

Nitrogen is one of the most abundant elements in nature, but most nitrogen NMR studies have so far been restricted to the ^{15}N isotope (natural abundance ~0.4%) to avoid problems associated with the large ^{14}N quadrupolar interaction, often in the MHz range.[1–4] Significant attention has been given to the possibility of developing high-resolution versions of ^{14}N solid state NMR to ease the acquisition of data without isotopic labelling, as well as to harvest additional information of the nitrogen site and its environment as provided by the quadrupolar interaction. This has led to the development of a number of promising techniques including ultra-wideband acquisition,[2,3,5] indirect detection[4,6–14] and excitation of ^{14}N overtone transitions.[15–24] Overtone NMR spectroscopy is advantageous because the width of the ^{14}N overtone powder pattern is unaffected, to first order in perturbation theory, by the quadrupolar interaction.[25] The experimental feasibility of directly detecting the ^{14}N overtone transition by NMR was first demonstrated in the 1980's by Tycko and Opella on static samples.[21–23,25] More recently, ^{14}N overtone spectra acquired under magic-angle spinning (MAS) have been reported, demonstrating the existence of only five ^{14}N spinning sidebands.[17,24] However, even under MAS, the overtone powder line is still in the kHz range, due to the presence of quadrupolar interaction terms of the spherical rank higher than 2 in the effective Hamiltonian. Any further improvements in resolution will necessitate the removal of these terms. Several methods exist for the elimination of high-rank quadrupole interaction terms. For half-integer quadrupolar nuclei, MQMAS[26–28] and STMAS[29] methods remove them by modifying the spin part of the effective Hamiltonian. For the spatial part, double rotation (DOR)[30–32] and dynamic angle spinning (DAS)[31,33] achieve the same objective by mechanical averaging.

One of the main challenges for the routine application of ^{14}N solid state NMR is resolution. In this communication we address this issue and demonstrate experimentally that, when applied to ^{14}N overtone NMR, DOR can bring about a significant further reduction in line width and take the NMR lines into the sub-kHz domain more commonly associated with NMR of spin-1/2 nuclei. Information on the size of the quadrupolar interaction is still present in the DOR spectra as the peak position is determined by a combination of the chemical shift and the second order isotropic quadrupolar shift. A further challenge to tackle with methods for sensitivity enhancement is already being developed, including polarization transfer,[24] DNP,[20] optimal control theory[34] and other instrumental improvements.

We also report progress with another long-standing issue associated with both DOR and overtone spectroscopy – the mathematical complexity of its numerical treatment. This paper uses the Fokker–Planck formalism[35,36] (recently implemented in

---

[a] School of Chemistry, University of Southampton, SO17 1BJ, Southampton, UK. E-mail: M.Carravetta@soton.ac.uk

[b] Department of Chemistry, College of Science, University of Mosul, Mosul, Iraq

[c] Centre for Biological Sciences, University of Southampton, SO17 1BJ, Southampton, UK

† Electronic supplementary information (ESI) available. See DOI: 10.1039/c5cp03266k

Spinach[37]). Its most attractive feature is that the DOR evolution operator is time-independent and the rotor coordinates, once discretized, are in a direct product relationship with the spin degrees of freedom.

Materials and methods

Solid state NMR

All the NMR measurements were performed on a Bruker AVANCE III 850 MHz spectrometer. All spectra were referenced indirectly to 0 ppm (liquid ammonia) using the ^{14}N signal of ammonium chloride at 39.3 ppm.[38] The overtone reference frequency was taken to be twice the ^{14}N reference frequency.

The DOR measurements used a wide-bore double resonance DOR probe, with diameters of 9.3 mm for the outer rotor (at magic angle) and 3.4 mm for the inner rotor (at 30.56°), respectively. Both rotors rotate in a clockwise direction. The power level was calibrated to give an overtone nutation frequency of $\omega_{\text{nut}}^{\text{OT}}/2\pi$ = 21 kHz for the ^{14}N overtone using the ^{17}O signal from the H_2O sample at 115.262 MHz and no ^{1}H decoupling was used under DOR.

MAS measurements were performed using a 3.2-mm-wide-bore triple resonance probe and a 3.2 mm zirconium oxide rotor, which rotates in the anticlockwise direction. For MAS, SPINAL64 decoupling at $\omega_{\text{nut}}^{\text{H}}/2\pi$ = 89 kHz was used throughout, while the overtone nutation frequency was set to $\omega_{\text{nut}}^{\text{OT}}/2\pi$ = 70 kHz and calibrated on water as above.

NMR samples

DOR experiments were performed on 27 mg of glycine-*N*,*N*,*O*-d_3 (Aldrich) and 24 mg of *N*-(acetyl-d_3)valine-d_{10} (NAV, prepared in house). The synthesis and characterization of fully deuterated NAV are described below. Deuterated samples were chosen for the DOR experiments due to the very limited ^{1}H decoupling performance of this probe. For the MAS measurements, 35 mg of naturally abundant glycine and 31 mg of naturally abundant NAV (both obtained from Sigma-Aldrich and used without further purification) were used. During MAS acquisition, SPINAL-64 decoupling was used with a nutation frequency of 89 kHz. All recycle delays were set to 0.5 s.

Synthesis of *N*-(acetyl-d_3)valine-d_{10}

Solvents and reagents were used as received from standard chemical suppliers unless otherwise stated. Fourier-transform infrared (FT-IR) spectra are reported in wavenumbers (cm^{-1}) and were collected on a Nicolet 380 spectrometer fitted with a diamond platform. ^{2}H and ^{13}C NMR spectra were recorded in CH_3OH/CD_3OD solutions (76.8 MHz and 100 MHz, respectively). Chemical shifts are reported in δ units using ppm and coupling constants (*J*) are reported in Hz and are rounded to the nearest 0.1 Hz. Melting points are uncorrected. Electrospray mass spectra were obtained using a Micromass platform mass analyser with an electrospray ion source (Scheme 1).

A clear solution was prepared by sonication of L-valine-d_8 (250 mg, 2 mmol) in D_2O (5 mL). Acetic anhydride-d_6 (433 mg, 4 mmol, 380 μL) was added at 0 min, 2 min and 4 min (127 μL at each interval). The reaction was sonicated for a further 5 min and then the solvent was removed *in vacuo*. The white residue was dissolved in methanol (20 mL) and the solution was filtered to remove traces of unreacted starting material. The filtrate was evaporated *in vacuo* and the residue was recrystallised twice from D_2O (2 × 1 mL) to give *N*-(acetyl-d_3)valine-d_{10} as a white solid (280 mg, 1.63 mmol, 82%). Further details of the characterization of this material are provided in the ESI.†

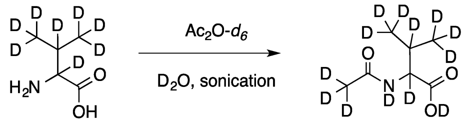

Scheme 1 Ref. 39.

Theory

The recently proposed Fokker–Planck formalism for solid state NMR calculations[36,38] allows the simulation of double rotation overtone NMR experiments to be performed without undue formulaic complexity and in reasonable time. The primary observation is very similar to the one made in the stochastic Liouville equation theory[40,41] – spatial dynamics may be introduced into the equation of motion simply by adding the corresponding derivatives to the evolution generator. In the case of DOR NMR, we have

$$\frac{\partial}{\partial t}\hat{\rho}(\varphi_{\text{O}},\varphi_{\text{I}},t)=\left[-i\hat{\hat{H}}(\varphi_{\text{O}},\varphi_{\text{I}},t)+\omega_{\text{O}}\frac{\partial}{\partial\varphi_{\text{O}}}+\omega_{\text{I}}\frac{\partial}{\partial\varphi_{\text{I}}}\right]\hat{\rho}(\varphi_{\text{O}},\varphi_{\text{I}},t) \tag{1}$$

where $\varphi_{\text{O,I}}$ are outer and inner rotor angles, $\omega_{\text{O,I}}$ are outer and inner rotor angular frequencies, $\hat{\rho}(\varphi_{\text{O}}, \varphi_{\text{I}}, t)$ is the state vector and $\hat{\hat{H}}(\varphi_{\text{O}},\varphi_{\text{I}},t)$ is the spin Hamiltonian commutation superoperator:

$$\hat{\hat{H}}(\varphi_{\text{O}},\varphi_{\text{I}},t)=\hat{\hat{H}}_0(\varphi_{\text{O}},\varphi_{\text{I}})+\hat{\hat{H}}_1(t) \tag{2}$$

in which the dependence on the two spinner angles is parametric and the time-dependent part (radiofrequency pulses, *etc.*) is orientation-independent.

If the spatial basis is chosen to be complex exponentials of the rotor angles, this formalism would reduce[35] to nested Floquet theory.[42,43] eqn (1) does, however, also permit a more direct numerical approach – exact matrix representations exist for the derivative operators on any periodic grid.[44] At the matrix level, this leads to remarkably simple relations:

$$\begin{aligned}\frac{\partial}{\partial t}\boldsymbol{\rho}(t)&=\mathbf{F}(t)\boldsymbol{\rho}(t),\quad\mathbf{F}(t)=\mathbf{H}_0+\mathbf{H}_1(t)+\mathbf{D}_{\text{I}}+\mathbf{D}_{\text{O}}\\ \mathbf{H}_1(t)&=\hat{\hat{E}}_{N_{\text{O}}}\otimes\hat{\hat{E}}_{N_{\text{I}}}\otimes\hat{\hat{H}}_1(t),\quad\mathbf{D}_{\text{I}}=\hat{\hat{E}}_{N_{\text{O}}}\otimes\hat{\hat{D}}_{N_{\text{I}}}\otimes\hat{\hat{E}}_{N_{\text{S}}},\\ \mathbf{D}_{\text{O}}&=\hat{\hat{D}}_{N_{\text{O}}}\otimes\hat{\hat{E}}_{N_{\text{I}}}\otimes\hat{\hat{E}}_{N_{\text{S}}}\end{aligned} \tag{3}$$

where N_{O} is the number of grid points for the outer rotor, N_{I} is the number of grid points for the inner rotor, N_{S} is the dimension of the spin state space, $\hat{\hat{E}}$ are identity superoperators of indicated dimensions, $\hat{\hat{D}}$ are Fourier spectral differentiation matrices[44] of indicated dimensions, the vector $\boldsymbol{\rho}(t)$ is obtained by stacking the state vector $\hat{\rho}((\varphi_O^{(n)}), \varphi_I^{(k)}, t)$ vertically in the order of increasing index of the inner rotor grid points, followed by the increasing index of the outer rotor grid points, and the block-diagonal matrix $\mathbf{H}_0$ is obtained by concatenating individual grid point Hamiltonians $\hat{\hat{H}}_0\left(\phi_O^{(n)}, \phi_I^{(k)}\right)$ in the same order as the state vectors.

From the practical programming perspective, the entire procedure is implemented and extensively annotated in the double rotation module of *Spinach.*[37] At the cost of increasing the matrix dimensions, the presence of the double rotation no longer troubles the end user – DOR dynamics operators are now just another static term in the background Hamiltonian $\mathbf{F}_0$:

$$\mathbf{F}(t) = \mathbf{F}_0 + \mathbf{F}_1(t), \quad \mathbf{F}_0 = \mathbf{H}_0 + \mathbf{D}_I + \mathbf{D}_O, \quad \mathbf{F}_1(t) = \mathbf{H}_1(t) \tag{4}$$

Another advantage of eqn (3) is that averages with respect to the phases of both rotors may be computed simply by taking the average of every block in $\boldsymbol{\rho}(t)$. This means that a powder simulation would only need a two-angle spherical averaging grid. In principle, even that is not strictly necessary,[37] but the mathematics in the grid-free case is less straightforward.

From this point onwards, the problem is identical to the simulation of a pulse-acquire experiment with a soft pulse, with the additional complication that the frequency of the pulse is *twice* the Larmor frequency of the spin – we are pulsing and detecting the overtone transition. The methods used to perform such simulations in reasonable time are described in our previous paper[24] and implemented in *Spinach.*[37] Because the number of spinning sidebands in overtone spectra is small and the resulting signals are narrow, five to seven grid points for the discretization of the phase of each rotor and a rank 5 Lebedev spherical averaging grid (parallel evaluation) were in practice found to be sufficient. When the calculation is parallelized with respect to the spherical averaging grid, the simulation shown in Fig. 1 takes a few minutes on a contemporary quad-core desktop workstation. All simulations for DOR and MAS experiments were performed using a single ^{14}N spin and neglecting the effects of protons and deuterons, using parameters summarised in Table 1. Hence the simulated DOR lineshapes are unaffected by the residual dipolar interactions with other neighbouring nuclei.

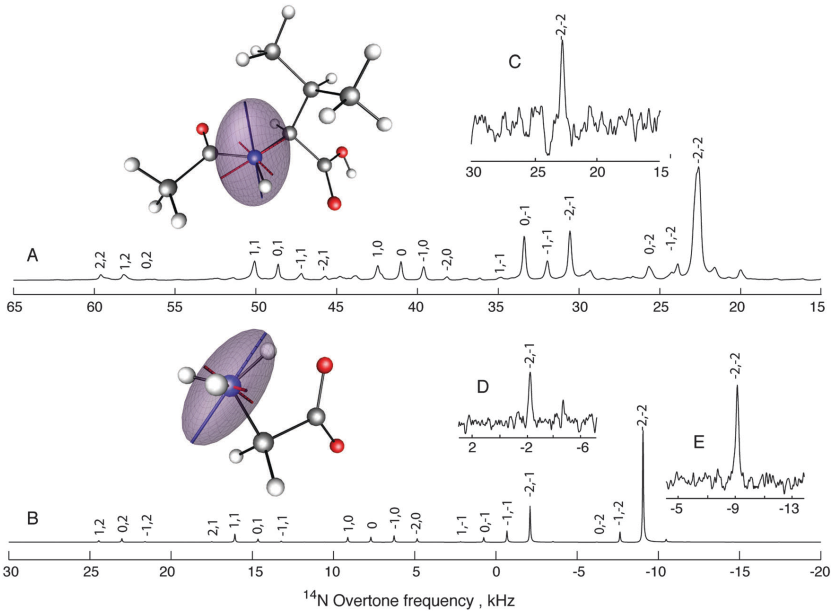

Fig. 1 DOR simulation and experiments for the ^{14}N overtone transition of glycine and NAV. Simulations were obtained using one ^{14}N spin, parameters from Table 1 and ideal pulses. Experiments were recorded at $\omega_{\text{nut}}^{\text{OT}}/2\pi$ = 21 kHz without decoupling. The numbers above the peaks are indices for spinning sidebands of the outer and inner rotors, respectively. (A) Simulation for NAV using the outer rotor frequency of 1.45 kHz and the inner rotor frequency of 7.6 kHz; (B) simulation for glycine using the outer rotor frequency of 1.425 kHz and the inner rotor frequency of 6.95 kHz; (C) the experimental spectra of the (−2, −2) spinning sideband of deuterated NAV acquired with 550 000 scans using 300 μs pulse width; and (D and E) experimental spectra of the (−2, −2) and (−2, −1) spinning sidebands of deuterated glycine respectively, acquired with 40 000 scans using 800 μs pulse width. The ellipsoid plots indicate the principal directions and the absolute values of the corresponding eigenvalues for the ^{14}N NQI tensors.

Table 1 Summary of parameters used for the simulations of glycine and NAV, using a single nitrogen spin. CSA interaction tensor orientations are quoted relative to the eigenframe of the ^{14}N quadrupolar interaction tensor. The inner and outer rotor speed values match the experimental data. Floquet theory convergence is achieved at rank 5 in the MAS simulations, and rank 5 was also used for the inner and the outer rotations in the DOR simulations

	C_q MHz	η_q	σ_{iso} ppm	$\Delta\sigma$ ppm	η	Euler angles, CSA	Lebedev Grid Rank	(ν_{out}, ν_{in}) kHz
Gly[45,46]	1.18	0.53	32.4	–	–	–	11	(1.425, 6.95)
NAV[47–50]	3.21	0.32	121.8	105	0.23	[−90, −90, −17]	65	(1.450, 7.60)

Results and discussion

DOR NMR spectra were simulated for *N*-acetylvaline (NAV) and glycine (Fig. 1) using spin Hamiltonian parameters given in Table 1. Under MAS, the spectrum consists of five sidebands, the strongest peak belonging to the +2 sideband for the counter-clockwise (it matters) spinner rotation direction.[17] Under DOR, each sideband is split into a further family of sidebands whose line width is reduced compared to those obtained under MAS.

Experimental spectra (Fig. 1, insets) of deuterated glycine-d_3 and NAV-d_{13} were acquired at 850 MHz on a Bruker Avance III spectrometer equipped with a DOR probe where both spinners rotate in a clockwise direction. Due to the limited excitation bandwidth, it is not possible to record the overall spectrum at once and only individual sidebands can be recorded. The overtone transition is forbidden in the Zeeman basis and overtone excitation is quite ineffective with the low power levels provided by the DOR probe, leading to the long pulse length and narrow bandwidth. Nutation curves for the (−2, −2) spinning sidebands of both compounds are given in Fig. S1 (ESI†). Glycine requires longer pulses than NAV due to a smaller quadrupole coupling constant. As seen in Fig. 1, experimental results and simulation show good agreement for both the resonance position and relative peak intensity. The most intense signal is at the (−2, −2) spinning sideband. Attempts were also made to acquire other DOR spinning sidebands for glycine (8000 scans) but there was no clear evidence of the signal (Fig. S2, ESI†). The extent of the line-narrowing effect of DOR on overtone NMR data may be appreciated from Fig. 2 and 3. Note that simulations are consistently much narrower than the experimental data. The larger experimental line width is attributed to spinning frequency instabilities and dipolar couplings to other nuclei. Spinning speed variations of the DOR rotors were of the order of ±25 Hz, and since we are observing not the center-band but sidebands of the overtone signal, unstable spinning will significantly broaden the resonances. Moreover, the DOR experiments were run at moderate spinning frequencies and without any decoupling, hence dipolar coupling to deuterium and protons is unlikely to be fully averaged out. Such an extended spin system is too complex for accurate numerical simulation. Simulations of DOR in Fig. 2 and 3 are sharp as they do not suffer from these effects, and assumed a single nitrogen atom, but the full quadrupolar Hamiltonian (not just first and second order terms) is considered here. The *Spinach* input file which generated Fig. 1 for glycine is included in the ESI† as an example.

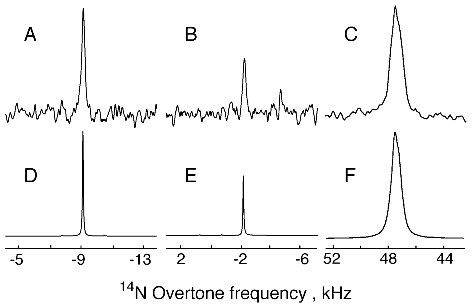

Fig. 2 Line width comparison for DOR and MAS overtone powder spectra of glycine. (A) DOR experiment for the (−2, −2) sideband of deuterated glycine, 40 000 scans, no decoupling; and (B) DOR experiment for the (−2, −1) sideband of deuterated glycine, 40 000 scans, no decoupling; DOR conditions are specified in the Fig. 1 caption. (C) MAS experiment for the +2 spinning sideband of glycine, 1024 scans, SPINAL64 decoupling, using $\omega_{nut}^{OT}/2\pi$ = 70 kHz and a 275 μs excitation pulse with $\omega_r/2\pi$ = 19.84 kHz. (D–F) Simulations of the data in A–C were performed using one ^{14}N spin, the parameters given in Table 1, and using durations and amplitudes matching the experimental data.

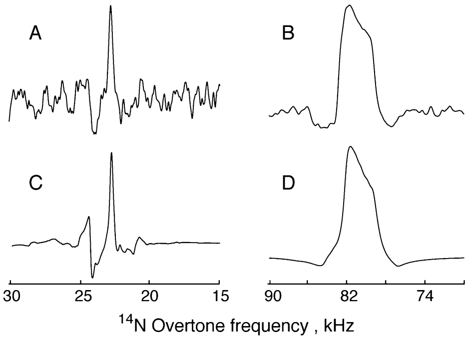

Fig. 3 Line width comparison for DOR and MAS overtone powder spectra of NAV. (A) DOR experiment data for the (−2, −2) spinning sideband of deuterated NAV, 550 000 scans, no decoupling. DOR conditions are specified in the Fig. 1 caption. (B) MAS experiment at the +2 spinning sideband of NAV, 40 000 scans, SPINAL64 decoupling, using $\omega_{nut}^{OT}/2\pi$ = 70 kHz and a 275 μs excitation pulse with $\omega_r/2\pi$ = 19.84 kHz; and (C) and (D) are the corresponding simulations, using one ^{14}N spin, the parameters given in Table 1, and using durations and amplitudes matching the experimental data. Note that the two features on the side of the main peak in (A) and (C) are spinning sidebands of the outer rotor.

For glycine, both the experimental and the simulated DOR NMR lines at (−2, −1) and (−2, −2) sidebands are about three times narrower than the corresponding MAS lines (Fig. 2). The experimental width of the (−2, −2) sideband under DOR is 280 Hz, while the width of the +2 spinning sideband under MAS is about 900 Hz (Fig. 2). It is clear from Fig. 3 that the (−2, −2) DOR sideband is much sharper than the +2 MAS sideband for NAV also: the 3.57 kHz line width under MAS is reduced to only 0.42 kHz under DOR, an improvement by almost an order of magnitude.

The reduction in line width observed under DOR indicates that the residual width apparent in the MAS ^{14}N overtone spectra does indeed arise from the second order quadrupolar terms in the Hamiltonian, removed in the DOR experiment. Importantly, none of that narrowing can be attributed to the narrow bandwidth of the very long overtone pulses under DOR, nor to the deuteration in the sample. This is because identical reduction in the line width is seen in the simulations in which the dipolar interactions with the surrounding atoms are switched off and ideal, very strong pulses are used (Fig. 1). The large number of scans required to record the DOR data arises from the reduced sample volume and reduced excitation efficiency compared to the MAS experiments, where stronger RF pulses are possible.[16]

Conclusions

These DOR results demonstrate the potential of ^{14}N double rotation overtone NMR in terms of resolution, with experimental line widths of a few hundred Hz achievable under DOR conditions. This represents a reduction by a factor of 3 and 9, as compared to MAS, for glycine and NAV, respectively, and a reduction in line width (determined by the third-order quadrupolar terms that survive double rotation averaging) to just tens of Hz predicted from theoretical simulations when artificial broadening is switched off, which sets the theoretical limit of what can be achieved under ideal conditions, without the intrinsic hardware limitation of DOR probes. The ongoing experimental developments go side by side with recent advances in theoretical and computational modelling. It is now possible to simulate elaborate overtone pulse sequences and soft pulses under MAS and double rotation in reasonable time.[37]

The routine application of DOR presents a number of technical challenges both in terms of sensitivity and RF performance. However pulsed methods for the suppression of 2nd order quadrupolar broadening effects in the indirect dimension (MQMAS and STMAS) have existed for half-integer spins for sometime and can be implemented using standard solid-state NMR probes.[26–29] Our findings highlight that for integer spin nuclei, such as the ^{14}N case explored herein, similar averaging of the second order quadrupolar broadening is feasible and the development of pulsed methods will enable the routine realization of the significant resolution enhancements we have observed.

Acknowledgements

MC thanks the University Research Fellowship scheme from the Royal Society for support. LJB thanks the Royal Society for a Dorothy Hodgkin fellowship. Ibraheem Haies thanks The Higher Committee for Education Development in Iraq for financial support. The UK 850 MHz solid-state NMR Facility instruments used in this research were funded by EPSRC and BBSRC, as well as the University of Warwick, including *via* part funding through Birmingham Science City Advanced Materials Projects 1 and 2 supported by Advantage West Midlands (AWM) and the European Regional Development Fund (ERDF). The authors acknowledge the use of the IRIDIS High Performance Computing Facility, and associated support services at the University of Southampton, in the completion of this work. The development of *Spinach* is supported by EPSRC (EP/H003789/1).

References

1 L. A. O'Dell, *Prog. Nucl. Magn. Reson. Spectrosc.*, 2011, **59**, 295–318.
2 T. Giavani, H. Bildsøe, J. Skibsted and H. J. Jakobsen, *J. Magn. Reson.*, 2004, **166**, 262–272.
3 R. W. Schurko, *Acc. Chem. Res.*, 2013, **46**, 1985–1995.
4 S. Cavadini, *Prog. Nucl. Magn. Reson. Spectrosc.*, 2010, **56**, 46–77.
5 L. A. O'Dell and C. I. Ratcliffe, *Chem. Commun.*, 2010, **46**, 6774–6776.
6 S. Cavadini, A. Abraham and G. Bodenhausen, *Chem. Phys. Lett.*, 2007, **445**, 1–5.
7 S. Cavadini, A. Abraham and G. Bodenhausen, *J. Magn. Reson.*, 2008, **190**, 160–164.
8 S. Cavadini, S. Antonijevic, A. Lupulescu and G. Bodenhausen, *J. Magn. Reson.*, 2006, **182**, 168–172.
9 S. Cavadini, S. Antonijevic, A. Lupulescu and G. Bodenhausen, *ChemPhysChem*, 2007, **8**, 1363–1374.
10 S. Cavadini, A. Lupulescu, S. Antonijevic and G. Bodenhausen, *J. Am. Chem. Soc.*, 2006, **128**, 7706–7707.
11 S. Cavadini, V. Vitzthum, S. Ulzega, A. Abraham and G. Bodenhausen, *J. Magn. Reson.*, 2010, **202**, 57–63.
12 Z. Gan, *J. Am. Chem. Soc.*, 2006, **128**, 6040–6041.
13 Z. Gan, J. P. Amoureux and J. Trébosc, *Chem. Phys. Lett.*, 2007, **435**, 163–169.
14 J. A. Jarvis, I. M. Haies, P. T. Williamson and M. Carravetta, *Phys. Chem. Chem. Phys.*, 2013, **15**, 7613–7620.
15 D.-K. Lee and A. Ramamoorthy, *Chem. Phys. Lett.*, 1998, **286**, 398–402.
16 Y. Nishiyama, M. Malon, Z. Gan, Y. Endo and T. Nemoto, *J. Magn. Reson.*, 2013, **230**, 160–164.
17 L. A. O'Dell and A. Brinkmann, *J. Chem. Phys.*, 2013, **138**, 064201.
18 L. A. O'Dell, R. L. He and J. Pandohee, *CrystEngComm*, 2013, **15**, 8657–8667.
19 L. A. O'Dell and C. I. Ratcliffe, *Chem. Phys. Lett.*, 2011, **514**, 168–173.

20 A. J. Rossini, L. Emsley and L. A. O'Dell, *Phys. Chem. Chem. Phys.*, 2014, **16**, 12890–12899.

21 R. Tycko and S. J. Opella, *J. Am. Chem. Soc.*, 1986, **108**, 3531–3532.

22 R. Tycko and S. J. Opella, *J. Chem. Phys.*, 1987, **86**, 1761.

23 R. Tycko, P. L. Stewart and S. J. Opella, *J. Am. Chem. Soc.*, 1986, **108**, 5419–5425.

24 I. Haies, J. Jarvis, H. Bentley, I. Heinmaa, I. Kuprov, P. T. F. Williamson and M. Carravetta, *Phys. Chem. Chem. Phys.*, 2015, **7**, 6577–6587.

25 M. Bloom and M. A. LeGros, *Can. J. Phys.*, 1986, **64**, 1522–1528.

26 L. Frydman and J. S. Harwood, *J. Am. Chem. Soc.*, 1995, **117**, 5367–5368.

27 A. Medek, J. S. Harwood and L. Frydman, *J. Am. Chem. Soc.*, 1995, **117**, 12779–12787.

28 G. Wu, D. Rovnyank, B. Q. Sun and R. G. Griffin, *Chem. Phys. Lett.*, 1996, **249**, 210–217.

29 Z. H. Gan, *J. Am. Chem. Soc.*, 2000, **122**, 3242–3243.

30 A. Samoson, E. Lippmaa and A. Pines, *Mol. Phys.*, 1988, **65**, 1013–1018.

31 B. F. Chmelka, K. T. Mueller, A. Pines, J. Stebbins, Y. Wu and J. W. Zwanziger, *Nature*, 1989, **339**, 42–43.

32 A. Samoson and A. Pines, *Rev. Sci. Instrum.*, 1989, **60**, 3239–3241.

33 K. T. Mueller, B. Q. Sun, G. C. Chingas, J. W. Zwanziger, T. Terao and A. Pines, *J. Magn. Reson.*, 1990, **86**, 470–487.

34 P. de Fouquieres, S. G. Schirmer, S. J. Glaser and I. Kuprov, *J. Magn. Reson.*, 2011, **212**, 412–417.

35 L. J. Edwards, D. V. Savostyanov, A. A. Nevzorov, M. Concistre, G. Pileio and I. Kuprov, *J. Magn. Reson.*, 2013, **235**, 121–129.

36 A. A. Nevzorov, *J. Magn. Reson.*, 2014, 249.

37 H. J. Hogben, M. Krzystyniak, G. T. Charnock, P. J. Hore and I. Kuprov, *J. Magn. Reson.*, 2011, **208**, 179–194.

38 P. Bertani, J. Raya and B. Bechinger, *Solid State Nucl. Magn. Reson.*, 2014, **61–62**, 15–18.

39 M. Erdelyi, V. Langer, A. Karlen and A. Gogoll, *New J. Chem.*, 2002, **26**, 834–843.

40 G. Moro and J. H. Freed, *J. Chem. Phys.*, 1981, **74**, 3757–3773.

41 C. F. Polnaszek, G. V. Bruno and J. H. Freed, *J. Chem. Phys.*, 1973, **58**, 3185–3199.

42 M. Leskes, P. K. Madhu and S. Vega, *Prog. Nucl. Magn. Reson. Spectrosc.*, 2010, **57**, 345–380.

43 I. Scholz, J. D. van Beek and M. Ernst, *Solid State Nucl. Magn. Reson.*, 2010, **37**, 39–59.

44 L. N. Trefethen, *Spectral methods in MATLAB*, Siam, 2000.

45 R. A. Haberkorn, R. E. Stark, H. Vanwilligen and R. G. Griffin, *J. Am. Chem. Soc.*, 1981, **103**, 2534–2539.

46 R. E. Taylor and C. Dybowski, *J. Mol. Struct.*, 2008, **889**, 376–382.

47 R. E. Stark, R. A. Haberkorn and R. G. Griffin, *J. Chem. Phys.*, 1978, **68**, 1996.

48 E. Salnikov, P. Bertani, J. Raap and B. Bechinger, *J. Biomol. NMR*, 2009, **45**, 373–387.

49 M. Bak, R. Schultz, T. Vosegaard and N. C. Nielsen, *J. Magn. Reson.*, 2002, **154**, 28–45.

50 G. Hou, I. J. Byeon, J. Ahn, A. M. Gronenborn and T. Polenova, *J. Chem. Phys.*, 2012, **137**, 134201.

Appendix E : Supporting information for Paper III. Supporting information for "^{14}N overtone transition in double rotation solid-state NMR"

by

Haies, I. M.; Jarvis, J. A.; Brown, L. J.; Kuprov, I.; Williamson, P.; Carravetta, M.

in

Accepted in *Phys. Chem. Chem. Phys.* 2015.

Electronic Supplementary Material (ESI) for Physical Chemistry Chemical Physics.

Supporting information for “^{14}N Overtone transition in double-rotation solid-state NMR”

Ibraheem M. Haies[a,b], James A. Jarvis[c], Lynda J. Brown[a], Ilya Kuprov[a],

Philip T.F. Williamson[c], and Marina Carravetta[a,*]

[a] School of Chemistry, University of Southampton, SO17 1BJ, Southampton, United Kingdom.

[b] Department of Chemistry, College of Science, University of Mosul, Mosul, Iraq.

[c] School of Biological Sciences, University of Southampton, SO17 1BJ, Southampton, United Kingdom.

MATERIALS AND METHODS

Characterisation of *N*-(Acetyl-d$_3$)valine-*d*$_{10}$

Melting point = 159–161 °C; ^{2}H NMR data in Fig. S3 (76.8 MHz, CH_3OH): δ 5.60 (s, 2H), 4.98 (s, 1H), 2.78 (s, 1H), 2.66 (s, 3H), 1.61 (s, 6H); ^{13}C NMR in Fig. S4 (100 MHz, CD_3OD) δ 175.8, 174.3, 59.5 (t, $J_{C\text{-}D}$ = 21 Hz), 31.4 (t, $J_{C\text{-}D}$ = 20 Hz), 22.4 (t, $J_{C\text{-}D}$ = 20 Hz), 19.2 (m), 18.0 (m); IR (powder) ν 3000, 1755, 1518, 1399, 1221, 1092 cm^{-1}; MS (ESI+) m/z $C_7H_3D_{11}NO_3^+$ Calc. 171.16, found 170.92; Calc. for $C_7H_2D_{11}NNaO_3$ 193.15, found 193.07; $C_7H_2D_{12}NO_3^+$ Calc. 172.16, found 172.00; Calc. for $C_7HD_{12}NNaO_3$ 194.15, found 194.11.

FIGURE S1:

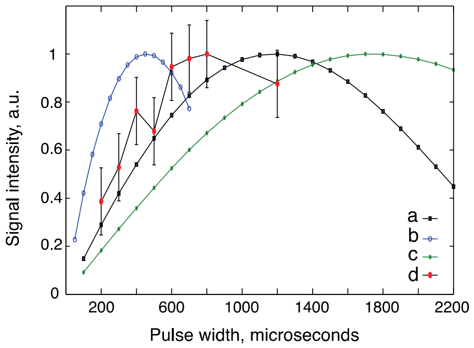

Figure S1. Selected calculated and experimental nutation curves for some of the ^{14}N overtone spinning sidebands of deuterated glycine and deuterated NAV at 20.0 T on the DOR probe, using a nominal RF amplitude of 21 kHz, as calibrated from the ^{17}O signal from water, with the spinning frequency specified in Table S1. (a) simulation of the $^{-}2, ^{-}2$ spinning sideband of glycine, (b) simulation of the $^{-}2, ^{-}2$ spinning sideband of NAV, (c) simulation of the $^{-}1, ^{-}2$ spinning sideband of glycine, (d) experimental data the $^{-}2, ^{-}2$ spinning sideband of glycine acquired with 8000 scans. The simulations were performed using parameters in Table S1.

FIGURE S2:

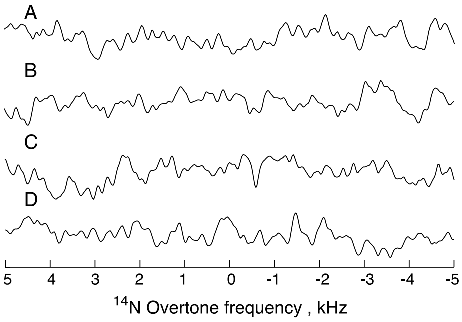

Figure S2. Experimental data for some of the ^{14}N overtone spinning sidebands for deuterated glycine under DOR at 20.0 T and a spinning frequency ν_{out}= 1.425 kHz and ν_{in}= 6.95 kHz, acquired with 8000 scans using a nominal RF amplitude of 21 kHz with 800 μs pulse length. All spectra are recorded near specific overtone spinning sidebands, therefore each spectrum appears at a different position. For the sake of convenience, the spectra are plotted on an arbitrary scale where 0 is set as the center of each spinning sideband. (A) $(-1,-2)$ spinning sideband, (B) $(0,-2)$ spinning sideband, (C) $(-2,0)$ spinning sideband, (D) $(-1,0)$ spinning sideband.

FIGURE S3:

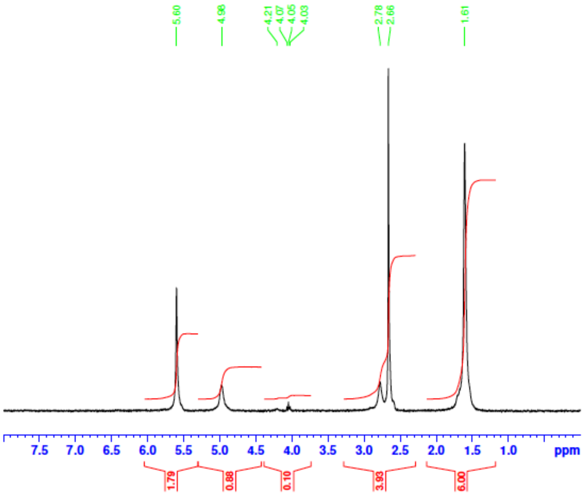

Figure S3: ^{2}H NMR of *N*-(acetyl-d_3)valine-d_{10} (76.8 MHz, CH_3OH)

FIGURE S4:

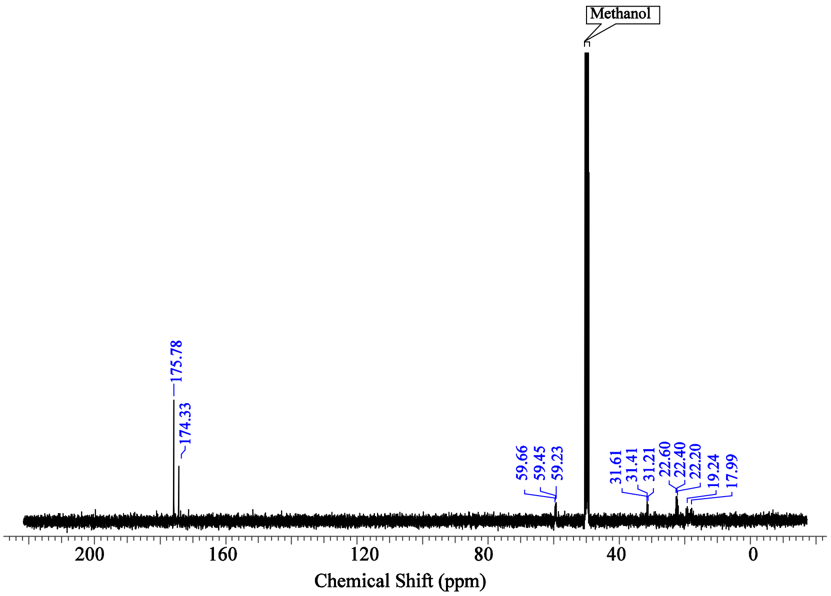

Figure S4: ^{13}C NMR of *N*-(acetyl-d_3)valine-d_{10} (100 MHz, CD_3OD)

SPINACH INPUT FILE FOR THE SIMULATION ON GLYCINE IN FIGURE 1.

```
% Panoramic double rotation overtone 14N spectrum of glycine. A short pulse
% with instrumentally inaccessible power is given to make the excitation
% pattern uniform.
% Note: slower spinning rates require larger spatial ranks.
% i.kuprov@soton.ac.uk
% m.carravetta@soton.ac.uk
% i.haies@soton.ac.uk

function glycine_dor_overtone()
% System specification
sys.magnet=14.1; sys.isotopes={'14N'};
inter.coupling.matrix{1,1}=eeqq2nqi(1.18e6,0.53,1,[0 0 0]);

% Relaxation theory
inter.relaxation='damp';
inter.damp_rate=500;

% Basis set
bas.formalism='sphten-liouv';
bas.approximation='none';
sys.disable={'trajlevel'};

% Spinach housekeeping
spin_system=create(sys,inter);
spin_system=basis(spin_system,bas);

% Experiment setup
theta=atan(sqrt(2));
parameters.rate_outer=-1500;
parameters.rate_inner=-7000;
parameters.rank_outer=4;
parameters.rank_inner=3;
parameters.axis_outer=[sin(theta) 0 cos(theta)];                 % 54.74 degrees
parameters.axis_inner=[sqrt(20-2*sqrt(30)) 0 sqrt(15+2*sqrt(30))]; % 30.56 degrees
parameters.grid='lebedev_ab_rank_5';
center=2*spin_system.inter.basefrqs(1)/(2*pi);
parameters.sweep=[(center-3e4) (center+2e4)];
parameters.npoints=256;
parameters.spins={'14N'};
parameters.axis_units='MHz';
parameters.invert_axis=1;
parameters.rho0=state(spin_system,'Lz','14N');
parameters.coil=cos(theta)*state(spin_system,'Lz','14N')+...
           sin(theta)*(state(spin_system,'L+','14N')+...
```

```
                state(spin_system,'L-','14N'))/2;
parameters.rframes={};

% Experiment parameters
expt.n_power=3.0e6;
expt.n_pulse=1.0e-6;
carrier_frequency=22e3;

% Get the Hamiltonian
[H,Q]=hamiltonian(assume(spin_system,'labframe'));

% Get the relaxation matrix
R=relaxation(spin_system);

% Get the averaging grid
sph_grid=load([spin_system.sys.root_dir '/kernel/grids/' parameters.grid '.mat']);

% Inform the user and shut up
report(spin_system,['powder average being computed over '
num2str(numel(sph_grid.weights)) ' orientations.']);
report(spin_system,'pulse sequence silenced to avoid excessive output.');
spin_system.sys.output='hush';

% Build pulse operator
N_pulse=cos(theta)*operator(spin_system,'Lz','14N')+sin(theta)*(operator(spin_system,'L+','
14N')+operator(spin_system,'L-','14N'))/2;
F_pulse=2*pi*expt.n_power*kron(speye(2*parameters.rank_outer+1),kron(speye(2*parame
ters.rank_inner+1),N_pulse));

% Project the relaxation matrix
R=kron(speye(2*parameters.rank_outer+1),kron(speye(2*parameters.rank_inner+1),R));

% Powder averaged spectrum
spectrum=zeros(1,parameters.npoints);
parfor k=1:numel(sph_grid.weights) %#ok<*PFBNS>

% Get the Fokker-Planck Liouvillian

[L,M,P]=doublerot(spin_system,{},H,Q,parameters,[sph_grid.alphas(k),sph_grid.betas(k),sph_
grid.gammas(k)]);

  % Get the pulse Hamiltonian
 omega=2*spin_system.inter.basefrqs(1)-2*pi*carrier_frequency;
 F_aver=average(spin_system,F_pulse,L+1i*M,F_pulse,omega,'matrix_log');

 % Project the states into Fokker-Planck space
 local_parameters=parameters;
```

```
 local_parameters.rho0=P*parameters.rho0;
local_parameters.rho0=local_parameters.rho0/norm(local_parameters.rho0);
local_parameters.coil=P*parameters.coil;
local_parameters.coil=local_parameters.coil/norm(local_parameters.coil);

% Apply the pulse

local_parameters.rho0=propagator(spin_system,F_aver+1i*R,expt.n_pulse)*local_parameter
s.rho0;

% Run the detection in the frequency domain

spectrum=spectrum+sph_grid.weights(k)*slowpass(spin_system,local_parameters,L+1i*M+1
i*R,0*L,0*L)

end

% Phasing
spectrum=spectrum*exp(1.25i);

% Plotting
spectrum_axis=linspace(-3e4,+2e4,parameters.npoints)/1e3;
subplot(2,1,1); plot(spectrum_axis,real(spectrum)); xlabel('kHz');
subplot(2,1,2); plot(spectrum_axis,imag(spectrum)); xlabel('kHz');
end
```

Appendix F : Paper IV. ^{14}N overtone NMR under MAS: signal enhancement using cross polarization methods

by

Haies, I. M.; Jarvis, J. A.; Kuprov, I.; Williamson, P.; Carravetta, M.

in

Will be submitted soon in *J. Magn. Reson.* 2015.

^{14}N overtone NMR under MAS: signal enhancement using cross polarization methods

Ibraheem M. Haies[a,b], James A. Jarvis[c],
Ilya Kuprov[a], Philip T.F. Williamson[c], Marina Carravetta[a,]*

[a] *School of Chemistry, University of Southampton,*
SO17 1BJ, Southampton, United Kingdom.

[b] *Department of Chemistry, College of Science,*
University of Mosul, Mosul, Iraq.

[c] *School of Biological Sciences, University of Southampton,*
SO17 1BJ, Southampton, United Kingdom.

[*]Corresponding author (m.carravetta@soton.ac.uk)

Abstract

Polarization transfer methods are widely adopted for the purpose of correlating different nuclear species as well as to achieve signal enhancement. The most effective applications of these methods in solid state NMR are towards spin 1/2 nuclei. Here we report that efficient polarization transfer from ^{1}H to the ^{14}N overtone transition ($\Delta m = 2$) can be achieved using cross polarization methods under magic-angle spinning conditions. This approach is demonstrated on two samples (α-glycine and N-acetylvaline). Spin locks of the order of several milliseconds can be easily obtained and efficient transfers, up to 6.7 per unit scan, can be achieved under favorable conditions despite MHz sized quadrupolar interaction.

Introduction

Nitrogen-14 has 99.6% abundance and has gone through a period of new life in the last 10 years, with a range of new methods appearing in the literature for the indirect detection of the nitrogen signal[1-13], for broadband excitation[14-16] and for overtone NMR experiments under static[17-20] and magic-angle spinning (MAS) conditions[19,20]. These methods have to deal with the challenges of exciting effectively the nitrogen signal under a range of conditions, with a potential variation of nuclear quadrupolar interaction (NQI) in a range between 0 to 5 MHz[21] depending on the nature, mobility and symmetry of the local environment. Overtone transitions are normally forbidden, but the presence of a large NQI in ^{14}N leads to a mixing of the Zeeman energy levels and makes the $\Delta m = 2$ transition weakly allowed. Moreover, the overtone transition benefits from the removal to first order of the quadrupolar terms. Under ultra-fast speed, ^{1}H detected overtone experiments are a very powerful route[22,23]. We recently demonstrated that the PRESTO-II sequence, with a simple spin echo on the overtone, leads to polarization transfer from ^{1}H to ^{14}N overtone with significant enhancement per scan in peak height. Due to the limited bandwidth of PRESTO, not the entire overtone line shape is excited with this approach and the resulting spectra are much narrower than the corresponding direct excitation spectra[24].

Cross-polarization (CP) excitation schemes have been employed on overtone transitions, with reported enhancements in sensitivity of up to a factor of 5.9 in single crystals[18] per unit scan. These static schemes did not exploit a Hartmann-Hahn spin lock but rather the formation of ^{1}H spin dipolar order, which was then transferred to overtone spin order. CP to ^{14}N overtone has been reported under MAS in combination with dynamic nuclear polarization (DNP)[25], using ramped CP and short contact time (125 μs) to transfer polarization from hyperpolarized ^{1}H nuclei to ^{14}N overtone. However, the same experiment without ^{1}H hyperpolarization shows no visible signal. The acquisition conditions adopted in those DNP CP measurements are typical for CP to nuclei with large NQI, as the spin lock in this situation cannot typically be fulfilled for more than few hundreds of microseconds[26-28].

In this work we present ^{14}N overtone signal enhancement using cross polarization (CP) methods under MAS. We find that effective spin locks of the overtone transition are readily obtained for contact times of several milliseconds. We find that the enhancement per unit scan is consistently more significant on N-acetylvaline (NAV) while it is negligible for glycine, and that CP with a linear or tangential amplitude sweep are very comparable and consistently much better than constant amplitude CP, with the signal enhancement as high as 6.7 for NAV under optimal conditions.

Materials and methods

Samples for NMR measurements. About 27 mg of α-glycine and 21 mg of NAV were used as purchased from Sigma-Aldrich without any purification and placed in 3.2 mm zirconium oxide pencil rotors.

Solid state NMR. All NMR experiments were performed on an Agilent 600 MHz spectrometer using a 3.2 mm narrow-bore T3 style triple resonance probe under MAS, at $\omega_r/2\pi$ = 19.84 kHz. The ^{14}N overtone RF nutation frequency was calibrated using the ^{17}O signal from a H_2O sample and nominal overtone nutation frequency of $\omega_{nut}^{OT}/2\pi$ =55 kHz was used in all overtone measurements. For all CP measurements, the optimal ^{1}H nutation frequency was carefully optimized and the optimal condition was achieved near $\omega_{nut}^{H}/2\pi$ =34 kHz for both glycine and NAV. SPINAL-64 decoupling[29] at $\omega_{nut}^{H}/2\pi$ =72 kHz was used in all measurements (during overtone acquisition as well as during the overtone pulse for direct excitation measurements). All CP measurements were performed using 2.5 s recycle delay, while for the direct excitation measurements the recycle delays were 0.4 s and 0.5 s for NAV and glycine respectively.

Because of significant probe ringing at the ^{14}N overtone frequency, all the direct excitation data were collected with a small dead time but left shifted to remove the first 70 μs of the FID. The CP data did not present the ringing artifact and a dead time of 10 μs was sufficient. The CP pulse sequences used in this work are shown in the Fig.1. The overtone spectra are referenced indirectly to twice the frequency of the ^{14}N NMR signal in liquid ammonia, using the ^{14}N signal of solid ammonium chloride at 39.3 ppm[30]. Since the most intense signal for the ^{14}N overtone transition is the second (+2) spinning sideband as established from previous studies[24,31,32], all experiments were performed near this condition.

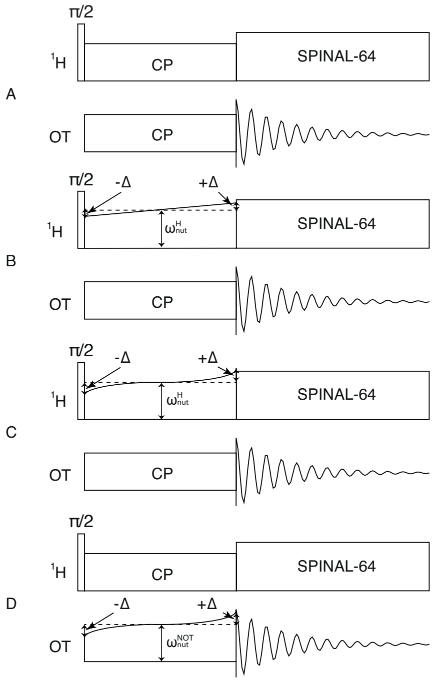

Fig. 1 CP sequences used in this work. (A) CP with constant amplitudes[33,34]. (B) Ramped CP[35] with ^{1}H amplitude sweep. (C) Adiabatic CP with ^{1}H amplitude tangential sweep[36,37].(D) Adiabatic CP with tangential sweep on the ^{14}N overtone channel.

Results and discussion

Encouraged by the success from Rossini et al[25] to achieve CP on overtone transition under MAS, we performed a detailed investigation on various CP pulse sequence to establish if significant levels of polarization enhancements can be achieved, as well as to establish the optimal conditions for this experiments on ^{14}N overtone NMR.

Constant-amplitude cross polarization

Fig.2 shows the variation in signal intensity as the ^{1}H nutation frequency is varied during the contact time, spanning over the Hartmann-Hahn matching conditions.

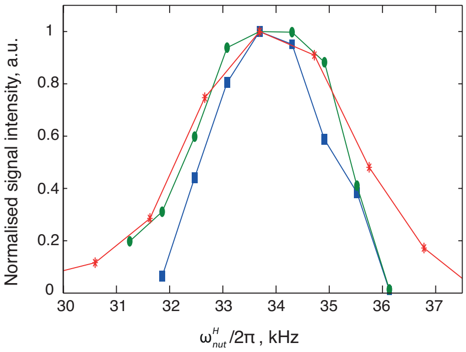

Fig. 2 Experimental Hartmann–Hahn matching profile acquired at $\omega_r/2\pi$ = 19.84 kHz, using $\omega^{OT}_{nut}/2\pi$ = 55 kHz and 5 ms contact time for both samples. NAV data (green cycle) were acquired with 2400 scans using constant amplitude CP. Glycine data (red astetrisk) using linear ramp amplitude CP with Δ/ω^{H}_{nut} = 0.05 and (blue square) constant amplitude CP were acquired with 1024 scans.

For both of the sample, the optimal condition is remarkably close to the predicted value for a spinning sample and follows the condition $(\omega^{OT}_{nut} \cong \omega^{H}_{nut} + \omega_r)$[38]. This is quite important as it makes the optimization of the parameters to set up CP on the overtone signal much simpler by providing a very easy way to predict starting place for parameter optimization. Moreover, the optimal value is fairly sampled independent, as demonstrated on our two test samples, which possess significantly different NQI.

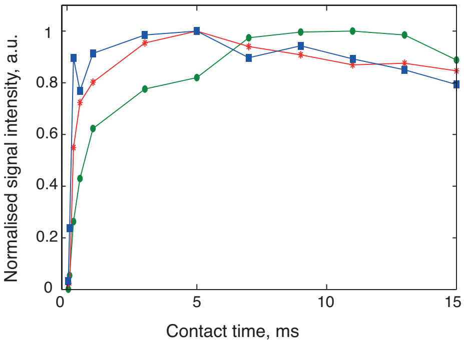

Fig. 3 Experimental CP build-up acquired with $\omega^{H}_{nut}/2\pi$ =34 kHz, $\omega^{OT}_{nut}/2\pi$ =55 kHz and $\omega_r/2\pi$ = 19.84 kHz. NAV data (green cycle) were acquired with 7200 scans using constant amplitude CP. Glycine data (red astetrisk) using linear ramp amplitude CP with Δ/ω^{H}_{nut} = 0.05 and (blue square) using constant amplitude CP were acquired with 1024 scans. Signal intensity is normalized to its own maximum.

Fig. 3 shows the build-up of the CP signal with respect to time. It is apparent that for both samples, the signal gain due to the polarization transfer is quite similar in the short time range. For longer times the NAV signal continues to grow and settles near 10 ms at an enhancement factor of 4.1, while the glycine signal does not grow beyond 5 ms and the overall enhancement is 0.6, hence with an overall reduction of the signal compared to direct excitation.

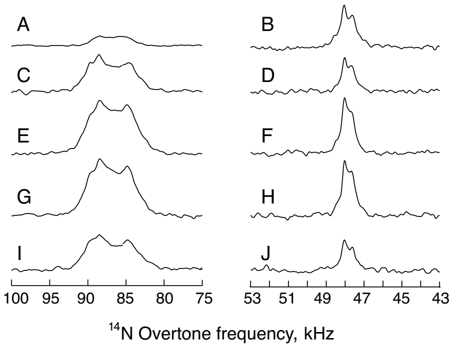

Fig. 4 Comparison between experimental spectra with direct excitation, CP methods from Fig. 1. Enhancement factors are summarized in Table 1. All data refer to the model samples NAV and glycine, using $\omega_r/2\pi$ = 19.84 kHz, $\omega_{nut}^{OT}/2\pi = 55$ kHz and $\omega_{nut}^{H} = 34$ kHz RF power on the ^{1}H for the CP. All NAV CP spectra were acquired with 20000 scans, 10 ms contact time. All glycine CP spectra were acquired with 1024 scans, 5 ms contact time. (A) Direct excitation spectrum of NAV with 16000 scans and 260 μs pulse length. (B) Direct excitation spectrum of glycine with 1024 scans and 260 μs pulse length, (C-D) Constant amplitude CP (Fig.1A) spectra of NAV and glycine respectively, (E) Linear RAMP CP (Fig. 1B) spectrum of NAV using Δ/ω_{nut}^{H} = 0.05, (F) Linear RAMP CP (Fig. 1B) spectrum of glycine using Δ/ω_{nut}^{H} = 0.055, (G) Adiabatic CP (Fig.1C) spectrum of NAV with sweep on the ^{1}H channel using Δ/ω_{nut}^{H} = 0.055, b_{cp}/ω_{nut}^{H}= 0.06. (H) Adiabatic CP (Fig.1C) spectrum of glycine with sweep on the ^{1}H channel using Δ/ω_{nut}^{H} = 0.05, b_{cp}/ω_{nut}^{H}= 0.06. (I) Adiabatic CP (Fig.1D) spectrum of NAV with sweep on the ^{14}N overtone channel using Δ/ω_{nut}^{OT} = 0.055, b_{cp}/ω_{nut}^{OT}= 0.06. (J) Adiabatic CP (Fig.1D) spectrum of glycine with sweep on the ^{14}N overtone channel using Δ/ω_{nut}^{OT} = 0.05, b_{cp}/ω_{nut}^{OT}= 0.06

These finding are remarkable, as one may expect a shorter contact time to be more favorable for samples with larger NQI like NAV, but instead quite the opposite is observed. Hence, the different behavior of the two systems and the overall lower efficiency observed in glycine are likely to relate to the different dynamics around the amide-bond of NAV and the highly mobile amine group of glycine, which disrupts the polarization transfer. The optimal contact times are much longer than what reported in Rossini et al work[25] by at least one order of magnitude, and significantly longer than what typically reported for quadrupolar nuclei, where the large NQI and the difficulty at achieving an effective spin lock typically lead to very short contact times. The optimal experimental spectra are provided in Fig 4 while a summary of experimental efficiencies is provided in Table 1.

Table 1. Summary of optimal CP conditions and enhancement factors with respect to the corresponding direct acquisition sequence, per unit scan. The values in each box refer respectively to the pulse sequences in Figure 1A (constant amplitude CP), 1B (linear RAMP CP), 1C (adiabatic sweep on ^{1}H) and 1D (adiabatic sweep on ^{14}N overtone).

Sample	Contact Time ms	Enhancement
Glycine	5	0.6 1.1 1.1 0.6
NAV	10	4.1 6.7 6.76 4.2

Ramped and adiabatic cross polarization

A significant improvement in signal intensity was observed with variable amplitude CP methods, in particular ramped CP and adiabatic CP. In these measurements, optimal contact times were found to be even longer than in constant amplitude CP. The optimal nutation frequency for the proton remained close to the values optimized under constant amplitude conditions, with the values provided in the body of the paper representing the nutation frequency in the middle of the amplitude sweep.

The symbol b_{cp} (instead of b_f in Ref. 37) defines the profile of the adiabatic sweep and Δ is half of the overall field variation across the linear or tangential sweep, as also defined in Ref. 37. In all cases a variation in ^{1}H amplitude during the contact period was found to be very beneficial for the overall efficiency of the polarization transfer step. The presence of a linear ramp broadens by about 2 kHz the Hartmann-Hahn matching compared to constant-amplitude CP (Fig.2, red and blue lines for glycine). Adiabatic CP shows the same trend as ramped CP (data not shown).

From the optimized constant amplitude CP, improved polarization transfer is obtained on both samples with a linear variation in ^{1}H nutation frequency by about $\mp 5\%$ as shown in Fig. 5. Optimal signal intensity for glycine was obtained after 5 ms with an enhancement of 1.1 and for NAV after 10 ms with an enhancement of 6.7 compared to direct excitation per unit scan (see Figs. 4E and 4F and Table 1).

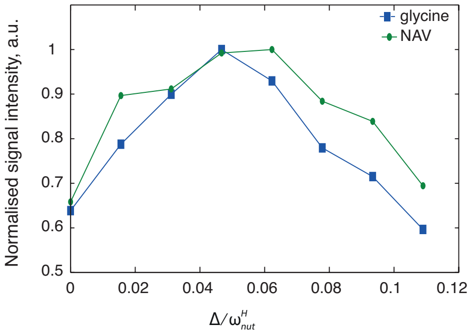

Fig. 5 Optimization of the Δ/ω_{nut}^{H} of the ramped CP pulse sequence (Fig.1B), using $\omega_{nut}^{OT}/2\pi$ =55 kHz, $\omega_{nut}^{H}/2\pi$ =34 kHz and $\omega_r/2\pi$ = 19.84 kHz. NAV data were acquired with 4000 scans and 10 ms contact time. Glycine data were acquired with 1024 scans and 5 ms contact time.

We explored for glycine the behavior of adiabatic CP sequences with amplitude sweeps on either the ^{1}H or the ^{14}N overtone RF fields. This is demonstrated in Fig. 6 through a comparison of the pulse sequences' performance over a range of contact times spanning from 5 ms to 26 ms. For each time point, a grid of experiments with discrete values b_{cp} and Δ were performed. While ^{1}H amplitude sweeps lead to a signal gain with a moderate enhancement of 1.1 (column 1 of Fig. 6), overtone amplitude sweep leads to a signal loss compared to direct acquisition, with enhancement factor of 0.6 (column 2 of Fig. 6). The corresponding spectra are given in Figs. 4G and 4I. For NAV, enhancement factors for the ^{1}H or ^{14}N overtone sweeps are respectively 6.76 and 4.2 using a contact time of 10 ms (Figs. 4H and 4J), hence also in this case the signal builds over longer time and the overall enhancement is much more significant than for glycine.

Ramp and adiabatic CP provide nearly identical performance when the ^{1}H amplitude is modulated, with significant improvement in performance over ^{14}N overtone sweep or constant amplitude CP.

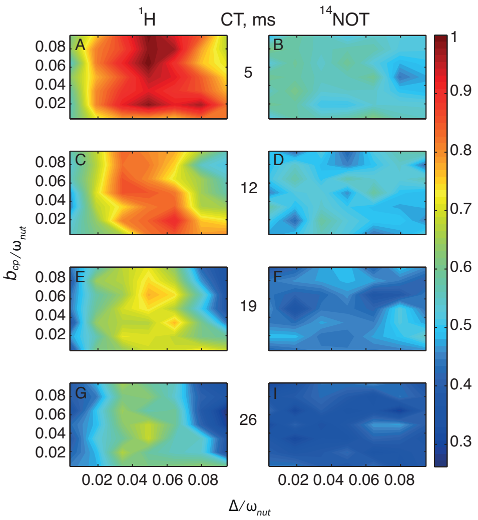

Fig. 6 ^{14}N overtone experimental data for glycine with 1024 scans under MAS at 19.84 kHz with $\omega_{nut}^{OT}/2\pi$ =55 kHz and $\omega_{nut}^{H}/2\pi$ =34 kHz using adiabatic CP with different contact times (5,12,19,26 ms respectively for rows 1 to 4). The tangential sweep was applied on the ^{1}H channel (Fig.1C) for the first column and on the ^{14}N overtone channel (Fig.1D) for the second column. The contour colour reflect the signal intensity, with the maximum set to 1.

Direct excitation and CP signal of the overtone transitions are both very sensitive to the RF pulse offset. Fig.7 shows variation of the signal intensity with respect to the RF offset. Both the adiabatic and linear RAMP CP bandwidths are similar and they are close to the direct excitation bandwidth for a pulse of duration 260 us. Although the CP bandwidth is not very broad, it is broader than the PRESTO-II bandwidth[24].

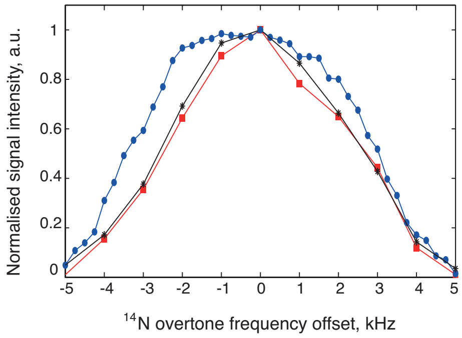

Fig. 7 Glycine experimental data of CP bandwidth compared to the direct excitation. Data acquired with 1024 scans at $\omega_r/2\pi$ = 19.84 kHz using $\omega_{nut}^{OT}/2\pi$ =55 kHz. (red square) Data from adiabatic CP using Δ/ω_{nut}^{H} = 0.05, b_{cp}/ω_{nut}^{H}= 0.06, ω_{nut}^{H} =34 kHz z, 5 ms contact time. (green astetrisk) Data from linear ramp amplitude CP (Fig.1B) using Δ/ω_{nut}^{H} = 0.05, ω_{nut}^{H} =34 kHz z, 5 ms contact time. (blue cycle) Direct excitation with 260 μs pulse length.

Conclusions

Polarization transfer using CP methods has some advantages compared to PRESTO, as it leads to more faithful lineshapes (hence quadrupolar parameters are easier to fit) and improved efficiency for NAV. The overall efficiency for glycine is not as good as for PRESTO, as PRESTO polarization transfer only requires hundreds of microseconds while with CP the very long contact time required to build the polarization on the overtone is more prone to be affected by the dynamics in the system. The excitation bandwidth for CP under the experimental conditions used in this work is also significantly better than PRESTO and quite similar to the bandwidth of conventional direct excitation methods. Therefore the bandwidth is not sufficient for effective excitation of nitrogen signals on samples with multiple sites in general, even though this may be still possible in very favorable cases[25], as the spread in chemical shift as well as in second order isotropic quadrupolar couplings often requires bandwidth of the order of tens of kHz.

Potentially this could be improved by setting up CP one probes with higher RF power, which enable a widening of the bandwidth.

Acknowledgements

This research was supported by the Wellcome Trust (PTFW and MC), EPSRC (EP/H003789/1, IK) and by the Royal Society University Research Fellowship (MC). Ibraheem Haies thanks The Higher Committee for Education Development in Iraq for financial support. With thank Richard Bounds for the XRD measurements on glycine.

References

(1) Amoureux, J. P.; Trebosc, J.; Hu, B.; Halpern-Manners, N.; Antonijevic, S. *J Magn Reson* **2008**, *194*, 317.

(2) Antonijevic, S.; Halpern-Manners, N. *Solid State Nucl Mag* **2008**, *33*, 82.

(3) Cavadini, S.; Abraham, A.; Bodenhausen, G. *J Magn Reson* **2008**, *190*, 160.

(4) Cavadini, S.; Antonijevic, S.; Lupulescu, A.; Bodenhausen, G. *J Magn Reson* **2006**, *182*, 168.

(5) Cavadini, S.; Antonijevic, S.; Lupulescu, A.; Bodenhausen, G. *ChemPhysChem* **2007**, *8*, 1363.

(6) Cavadini, S.; Lupulescu, A.; Antonijevic, S.; Bodenhausen, G. *J. Am. Chem. Soc.* **2006**, *128*, 7706.

(7) Gan, Z. H. *J Magn Reson* **2007**, *184*, 39.

(8) Gan, Z. H.; Amoureux, J. P.; Trebosc, J. *Chem Phys Lett* **2007**, *435*, 163.

(9) Jarvis, J. A.; Haies, I. M.; Williamson, P. T. F.; Carravetta, M. *Phys Chem Chem Phys* **2013**, *15*, 7613.

(10) Nishiyama, Y.; Endo, Y.; Nemoto, T.; Utsumi, H.; Yamauchi, K.; Hioka, K.; Asakura, T. *J Magn Reson* **2011**, *208*, 44.

(11) Vitzthum, V.; Borcard, F.; Jannin, S.; Morin, M.; Mieville, P.; Caporini, M. A.; Sienkiewicz, A.; Gerber-Lemaire, S.; Bodenhausen, G. *ChemPhysChem* **2011**, *12*, 2929.

(12) Gan, Z. H. *J Am Chem Soc* **2006**, *128*, 6040.

(13) Cavadini, S. *Prog. Nucl. Magn. Reson. Spectrosc.* **2010**, *56*, 46.

(14) Schurko, R. W. *Acc. Chem. Res.* **2013**, *46*, 1985.

(15) O'Dell, L. A.; Ratcliffe, C. I. *Chem. Commun.* **2010**, *46*, 6774.

(16) Giavani, T.; Bildsoe, H.; Skibsted, J.; Jakobsen, H. J. *J. Magn. Reson.* **2004**, *166*, 262.

(17) Tycko, R.; Stewart, P. L.; Opella, S. J. *J. Am. Chem. Soc.* **1986**, *108*, 5419.

(18) Tycko, R.; Opella, S. J. *J. Chem. Phys.* **1987**, *86*, 1761.

(19) Tycko, R.; Opella, S. J. *J Am Chem Soc* **1986**, *108*, 3531.

(20) Bloom, M.; LeGros, M. A. *Can. J. Phys.* **1986**, *64*, 1522.

(21) O'Dell, L. A.; Schurko, R. W. *Physical chemistry chemical physics : PCCP* **2009**, *11*, 7069.

(22) Nishiyama, Y.; Malon, M.; Gan, Z.; Endo, Y.; Nemoto, T. *J. Chem. Phys* **2013**, *230*, 160.

(23) O'Dell, L. A.; He, R. L.; Pandohee, J. *CrystEngComm* **2013**, *15*, 8657.

(24) Haies, I. M.; Jarvis, J. A.; Bentley, H.; Heinmaa, I.; Kuprov, I.; Williamson, P. T.; Carravetta, M. *Physical chemistry chemical physics : PCCP* **2015**, *17*, 6577.

(25) Rossini, A. J.; Emsley, L.; O'Dell, L. A. *Phys Chem Chem Phys* **2014**, *16*, 12890.

(26) Vega, A. J. *Solid State Nucl. Magn. Reson.* **1992**, *1*, 17.

(27) Vega, A. J. *J. Magn. Reson.* **1992**, *96*, 50.

(28) Sun, W.; Stephen, J. T.; Potter, L. D.; Wu, Y. *J. Magn. Reson. Ser. A* **1995**, *116*, 181.

(29) Fung, B. M.; Khitrin, A. K.; Ermolaev, K. *J. Magn. Reson.* **2000**, *142*, 97.

(30) Bertani, P.; Raya, J.; Bechinger, B. *Solid State Nucl Mag* **2014**, *61–62*, 15.

(31) O'Dell, L. A.; Ratcliffe, C. I. *Chem Phys Lett* **2011**, *514*, 168.

(32) O'Dell, L. A.; Brinkmann, A. *J Chem Phys* **2013**, *138*.

(33) Pines, A.; Gibby, M. G.; Waugh, J. S. *J. Chem. Phys.* **1973**, *59*, 569.

(34) Hartmann, S. R.; Hahn, E. L. *Phys. Rev.* **1962**, *128*, 2042.

(35) Peersen, O. B.; Wu, X. L.; Kustanovich, I.; Smith, S. O. *J. Magn. Reson., Ser A* **1993**, *104*, 334.

(36) Baldus, M.; Geurts, D. G.; Hediger, S.; Meier, B. H. *J. Magn. Reson., Ser A* **1996**, *118*, 140.

(37) Hediger, S.; Meier, B. H.; Ernst, R. R. *Chem. Phys. Lett.* **1995**, *240*, 449.

(38) Stejskal, E. O.; Schaefer, J.; Waugh, J. S. *J. Magn. Reson.* **1977**, *28*, 105.